

Random Field in Dilute Anisotropic Dipolar Magnets

*Thesis submitted in partial fulfillment of the requirement for the degree of master of science
in the Faculty of Natural Sciences*

Submitted by: **Yoav Pollack**

Advisor: **Dr. Moshe Schechter**

Department of Physics

Faculty of Natural Sciences

Ben-Gurion University of the Negev

Signature of student:

Date:

Signature of advisor:

Date:

Signature of chairperson of the

committee for graduate studies:

Date:

March 19, 2013

Abstract

$\text{LiHo}_x\text{Y}_{1-x}\text{F}_4$ in an applied transverse field was shown to be a realization of the Random Field Ising Model (RFIM), in both its ferromagnetic and spin glass phases. In this work we use exact numerical diagonalization of the full Hamiltonian of 2 Ho ions to calculate explicitly the random field in weak and strong transverse fields. We then suggest a direct measurement of the random field through subkelvin co-tunneling experiments.

Contents

1	Introduction	6
1.1	Introduction	6
1.2	Outline	7
2	Theoretical Foundation	9
2.1	Anisotropic Dipolar Ising Systems	9
2.2	The LiHoF ₄ Crystal	11
2.3	Ho Ion Electronic States	13
2.4	HyperFine Interaction	15
2.5	Applied Magnetic Field	16
2.5.1	Transverse Field	16
2.5.2	Longitudinal Field	18
2.6	Dipolar Interaction	25
3	Random Fields	27
3.1	Perturbation Theory	27
3.2	Beyond Perturbation Theory	29
4	Proposed Direct Random Field Measurement	36
4.1	Adding a Constant Transverse Field - Dynamical	37
4.2	Adiabatic Sweeping	41
4.2.1	Adding a Constant Transverse Field - Equilibrium	45
4.2.2	Sweeping the Transverse Field - Equilibrium	49
4.3	Advantages and Disadvantages of the Three Variations	52

5 Summary	54
Appendices	56
A Extended Discussion of Single Ion States	56
A.1 Ion Positions in the LiHoF ₄ Unit Cell	56
A.2 Ho Free-Ion States	60
A.3 Crystal Field	60
A.4 HyperFine Constant	65
B Perturbation Theory - Extended	67
B.0.1 An Intuitive Picture of Symmetry Breaking	67
B.0.2 2 nd Order - First Approximation	69
B.0.3 2 nd Order - Complete	72
B.0.4 3 rd Order	73
B.0.5 Comparison to Numerics	76
C Iterative Diagonalization	79
D Further Numerical Results for Section 3.2	81
E Further Plots for Chapter 4	88
E.1 A Second Example for Section 4.1	89
E.2 Refined Plots for Section 4.2	89
F Landau-Zener Transition Profile	95
G Numerical Routines	100
G.1 Finding the 17 Crystal Field States	100
G.2 Including HF Structure (Extending to Electro-Nuclear States)	102
G.3 The Full 2 Ions Model	105
G.4 Tracking Diabatic States Through Crossings	109
G.4.1 Review of Method	109
G.4.2 Code	109
G.5 Shifted Peaks Positions	117
G.6 Finding Energy Gaps in Avoided Level Crossings	119

G.7 Finding the Landau-Zener Transition Profile	122
---	-----

Chapter 1

Introduction

1.1 Introduction

The Random Field Ising Model (RFIM) has attracted much attention from the physics community ever since its interesting implications concerning critical dimensionality for phase transitions were first discussed by Imry and MA [1] in 1975. Experimentally, many studies were performed using a diluted Antiferromagnet (AFM) under an applied longitudinal magnetic field as first proposed by Fishman and Aharony [2].

In recent years the study of quantum phase transitions has also attracted growing attention, though no realization of such a transition has yet been confirmed. Understanding of the destruction of phase through random fields can give insight as to which systems are likely to present quantum phase transitions. Evaluating the magnitude and other properties of the random field can help to further this effort by predicting the location of the critical points.

Analysis of the RFIM model has seen much progress since its early days, and many more realizations have been found [3, 4, 5, 6]. However, only recently a realization of the RFIM in FM systems was found in the anisotropic dipolar magnets.

Anisotropic dipolar magnets are ideal systems to study the Ising model in general. Such systems exhibiting ground Ising-like states and under the additional condition of disorder in the dipolar interactions can be used to model the RFIM in both their spin glass (SG) and FM regimes. This is because the Off Diagonal Dipolar (ODD) interaction terms combined with a constant applied transverse magnetic field provide a site dependant mechanism for biasing the Ising states.

As the LiHoF_4 crystal is a prominent and well studied case of an Ising dipolar magnet, it is employed here as an exemplary realization of such models. This realization is preferable to diluted AFM due to the possibility of applying a spatially constant longitudinal magnetic field to it as opposed to the case of staggered magnetization. The disorder is induced by diluting the magnetic Ho ions so that their positions on the lattice are random.

A recent paper by Schechter and Laflorencie [7] showed the dependence of the effective longitudinal field on the positions of the randomly distributed magnetic Ho ions, providing a mechanism to predict the site dependence of the RFIM for small fields. Our current study extends this work to large measurable fields and suggests practical measurement methods. This should provide a first direct microscopical measurement of random fields in a FM system.

1.2 Outline

Chapter 2 presents the theoretical foundation for this work. The general model for anisotropic dipolar systems showing Ising ground states is discussed (section 2.1) and the details of the $\text{LiHo}_x\text{Y}_{1-x}\text{F}_4$ realization are reviewed (section 2.2 and on). Included in this review (section 2.5.2) are results of experiments both validating the fundamental model and paving the way to new measurements capable of assessing the validity of this study.

Chapter 3 is concerned with establishing random field behaviour and evaluating its magnitude. It reviews the derivation of the random field in the perturbative regime on

which this current work is based (3.1), and presents a new extension to this analysis outside perturbation theory using numerical routines (3.2).

In chapter 4 three experiments are proposed, aiming at a direct measurement of the effective random fields in anisotropic dipolar systems. These experiments can also validate the theoretical predictions of this thesis. A summary of analysis results is given in chapter 5.

Appendix A features an extended discussion of the single-ion states presented in sections 2.2 through 2.4. Appendix B presents a more extended and full discussion of the perturbative analysis of section 3.1. In Appendix C the main numerical method used in this work is reviewed. In appendix D, further numerical results can be found complementing the ones in the main text. Appendix E offers an extension to discussions in chapter 4 regarding the proposed experiments. Appendix F presents the analysis of quantum ($T = 0$) Landau-Zener transitions relevant to section 4.1. All Matlab codes used for this study (e.g. for numerical routines) are given in appendix G.

Chapter 2

Theoretical Foundation

2.1 Anisotropic Dipolar Ising Systems

The model considered in this work is of a system with spin-like components, where each spin has a ground state Ising-like doublet, and well removed excited states. The interaction between the components is dipolar. A general Hamiltonian for such Anisotropic Dipolar Magnets can be formulated as:

$$H = -D \sum_i [(J_i^z)^2 - J_0] + \sum_{i \neq j} V_{ij}^{zz} J_i^z J_j^z \quad (2.1.1)$$

where D is a constant dictating the anisotropy measure, $J_i^{x,y,z}$ are magnetic moment components, J_0 is a constant used to calibrate the zero energy and $V_{ij}^{\alpha\beta}$ are the dipolar interaction coefficients ($\alpha, \beta = x, y, z$).

The first part of this Hamiltonian is the anisotropy term with D considered large, and the second is the dipolar interaction with the non-longitudinal terms omitted. While considering only the longitudinal part of the dipolar interaction can seem arbitrary at first, there are indeed realizations in which all the other terms cancel by symmetry (e.g. undiluted LiHoF_4 [8]). In fact even when these terms do not cancel out, they can be neglected due to the large anisotropy dictating $\langle J_{x,y} \rangle \ll \langle J_z \rangle$. However this simplification of the

dipolar interaction has its limitations as discussed in section 2.5.1.

As already implied, only large magnetic moments ($J > \frac{1}{2}$) are considered, as the existence of excited eigenstates for single ions, change the physics significantly. In particular the $J = 8$ case matches the realization presented in this work (see section 2.3).

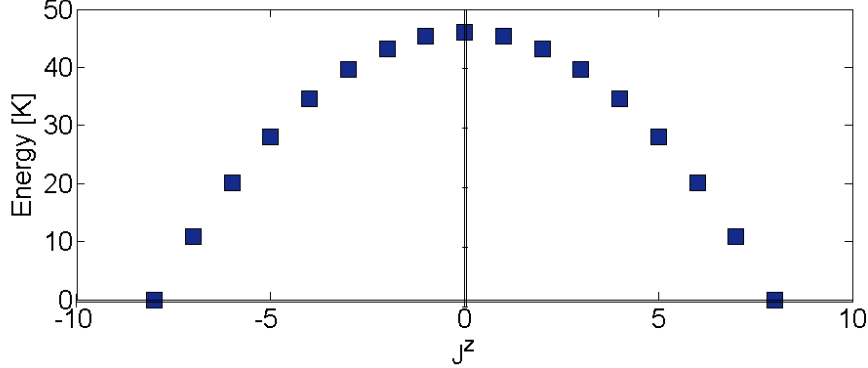


Figure 2.1: The single ion energy levels and $\langle J_z \rangle$ expectancy values for $J = 8$, $D = 0.72$. D is chosen so that the energy difference Ω_0 between the ground states and the lowest excited state, is the same as in the realization presented in section 2.3.

In general, large spin ions do not conform to the usual conception of the (spin half) Ising model. However at low enough temperature compared to the single ion level spacing, only the ground states are populated so that they can be taken as Ising-like states.

Under these constraints, the Hamiltonian above (eq. 2.1.1) can be formulated in effective spin half form:

$$H = \sum_{i \neq j} U_{ij}^{zz} \sigma_i^z \sigma_j^z \quad (2.1.2)$$

with σ^z being a Pauli 2X2 matrix.

2.2 The LiHoF₄ Crystal

For a realization of disordered anisotropic dipolar systems, the LiHoF₄ crystal is considered with the Ho sites diluted randomly by Yttrium ions. This is because the quality of single crystals of LiHoY₄ is usually very high (as they are used for high power lasers) and the relevant parameters of the crystal (see section 2.3 and appendix A.3) obtained through fitting to experimental results, are known with very good accuracy [9].

From this point on, the discussion is carried out in terms of this realization. However, all the analytical derivations can be applied to any realization obeying the constraints discussed in the previous section (2.1).

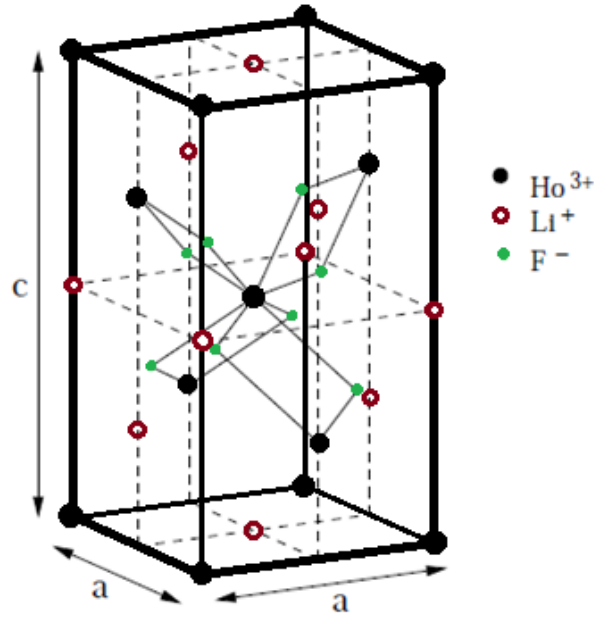


Figure 2.2: The unit cell for LiHoF₄. $a = 5.175\text{\AA}$, $c = 10.75\text{\AA}$.

Positions of the Ho, Li and F ions in the unit cell are found in appendix A.1. The c axis depicted in the figure will function as the easy Ising (z) axis. Illustration taken from Gingras and Henelius [10]

The concentration of the Ho ions in the crystal is given by x and the diluted crystal is denoted as $\text{LiHo}_x\text{Y}_{1-x}\text{F}_4$. As the Ho ions are highly magnetic ($\mu_{\text{Ho}} = 10.6\mu_B$) [11] and the other elements in the crystal negligibly so (e.g. $\mu_Y = 0.14\mu_B$) this effectively leads to magnetic moments randomly distributed throughout the lattice. Since the Yttrium ions have an atomic radius similar to that of Ho, they do not distort the lattice [12].

The invariance of the crystal structure under a transformation $(r, \theta, \phi) \longrightarrow (r, \pi - \theta, \phi + \frac{\pi}{2})$ implies an S_4 symmetry [13], a property which is useful in determining the Crystal Field (see appendix A.3).

The $\text{LiHo}_x\text{Y}_{1-x}\text{F}_4$ crystal shows several distinct phases. At temperatures $T < 1.53\text{K}$, the undiluted LiHoF_4 is an Ising dipolar ferromagnet. As the Ho concentration decreases, frustration due to dipolar interactions builds up, until at $x \simeq 0.25$ a dipolar spin glass phase appears.

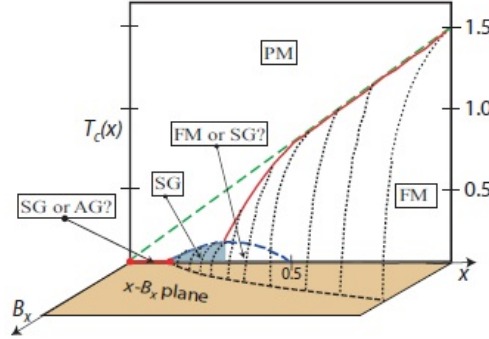


Figure 2.3: The phase diagram for $\text{LiHo}_x\text{Y}_{1-x}\text{F}_4$ as a function of dilution x , temperature T and transverse magnetic Field B^x . Diagram taken from Gingras and Henelius [10]

Figure 2.3 appeared in a 2011 review on the current understanding of the $\text{LiHo}_x\text{Y}_{1-x}\text{F}_4$ crystal. It clearly shows there are regimes in the phase diagram that are not yet resolved.

In the current study, the discussion is restricted to the very dilute regime $x \ll 0.1$. In this dilute regime we can assume that while a small percentage of ions have a close-by neighbor (much closer than the average distance for the chosen dilution), the number of ions

with more than one close-by neighbor is negligible in comparison.

2.3 Ho Ion Electronic States

The "free" trivalent Ho ion has the configuration 5I_8 ($J = 8$) (see appendix A.2). The Crystal Field generated by the electrostatic potential of all the ions in the LiHoF_4 compound partially breaks the 17-fold degeneracy ($J^z = -8, -7, \dots, 7, 8$) of the free-ion states and translates to a large uniaxial magnetic anisotropy along the z axis. This Crystal Field term can be formulated following Chakraborty et al. [14] as:

$$H_{CF} = B_2^0 O_2^0 + B_4^0 O_4^0 + B_6^0 O_6^0 + B_4^4(C) O_4^4(C) + B_6^4(C) O_6^4(C) + B_6^4(S) O_6^4(S) \quad (2.3.1)$$

where the O_n^l are Stevens' operator equivalents and the B_n^m are crystal specific coefficients, called Crystal Field Parameters, obtained through fitting to experiments (see appendix A.3 for discussion, coefficients values and operators definitions).

The operator equivalents O_2^0 , O_4^0 and O_6^0 do not break the symmetry (to rotations around the z axis) dictating states characterized by their J_z value. However the $O_4^4(C)$, $O_6^4(C)$ and $O_6^4(S)$ contain terms with J_\pm^4 so that the eigenstates of the Crystal Field are combinations of free-ion states with $\Delta J^z = \pm 4$. This gives Crystal Field eigenstates belonging to the four one-dimensional irreducible representations $[\Gamma_{1,2,3,4}]$ of the S_4 group:

$$V_{\Gamma_3} = \alpha^i |Jz = -7\rangle + \beta^i |Jz = -3\rangle + \gamma^i |Jz = 1\rangle + \delta^i |Jz = 5\rangle \quad (2.3.2a)$$

$$V_{\Gamma_4} = \alpha^i |Jz = 7\rangle + \beta^i |Jz = 3\rangle + \gamma^i |Jz = -1\rangle + \delta^i |Jz = -5\rangle \quad (2.3.2b)$$

$$V_{\Gamma_2} = \alpha^i |Jz = -6\rangle + \beta^i |Jz = -2\rangle + \gamma^i |Jz = 2\rangle + \delta^i |Jz = 6\rangle \quad (2.3.2c)$$

$$V_{\Gamma_1} = \alpha^i |Jz = -8\rangle + \beta^i |Jz = -4\rangle + \gamma^i |Jz = 0\rangle + \delta^i |Jz = 4\rangle + \epsilon^i |Jz = 8\rangle \quad (2.3.2d)$$

with different coefficients α^i through ϵ^i for each state ($i = 1..17$).

These states and their corresponding energies were also found numerically through a standard Matlab diagonalization routine (see results in appendix A.3 and code in appendix G.1)

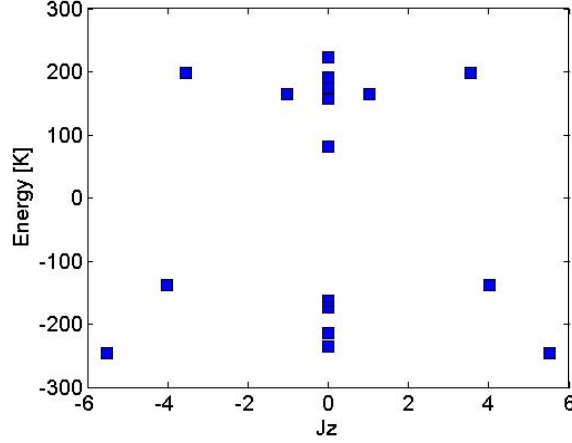


Figure 2.4: *Energies and $\langle J_z \rangle$ expectancy values for the different Ho ion electronic states. Figure based on similar plot in Giraud et al. [15]*

The ground states are well separated ($\Omega_0 = 10.8K$) from the excited states so that at temperatures far lower than Ω_0 , only the ground state doublet will be significantly populated. These ground states, belonging to the groups Γ_3 and Γ_4 are related by time reversal symmetry and can be viewed as Ising states. These states are hence forth labelled as $|\uparrow\rangle$ and $|\downarrow\rangle$ according to their $\langle J_z \rangle = \pm 5.5$. This is a manifestation of the anisotropy mentioned before ($\langle J_{x,y} \rangle \simeq 0$). In the presence of an applied transverse field, the first excited state has a significant role in breaking the degeneracy of the ground doublet (see section 3.1) and in introducing coupling between the Ising states. It is labelled Γ_2 after the irreducible representation it belongs to (this should not cause confusion as there as is no direct reference to other excited states throughout the remainder of this thesis, except in appendix B where this is clearly noted).

2.4 HyperFine Interaction

At low enough temperatures, even weak HyperFine (HF) interactions can play an important part (see e.g. [16]) since in some systems they can impede coupling between the ground states. This is even more pronounced in Ho ions where the HF interaction is relatively strong.

The HF interaction can be conveniently separated into two parts:

$$\begin{aligned}
 H_{HF} &= A_J \sum_i \vec{I}_i \cdot \vec{J}_i \\
 &= A_J \sum_i I_i^z \cdot J_i^z + \frac{A_J}{2} \sum_i (I_i^+ \cdot J_i^- + I_i^- \cdot J_i^+) \\
 &= H_{HF}^{\parallel} + H_{HF}^{\perp}
 \end{aligned} \tag{2.4.1}$$

with $I = \frac{7}{2}$ and $A_J = 0.039K$ as determined through fitting to resonance measurements (see appendix A.4).

The "longitudinal" part of the interaction H_{HF}^{\parallel} splits each of the electronic ground doublet into 8 equidistant levels $\Delta E \simeq 201mK$ according to the projection I^z of the nuclear spin on the z axis.

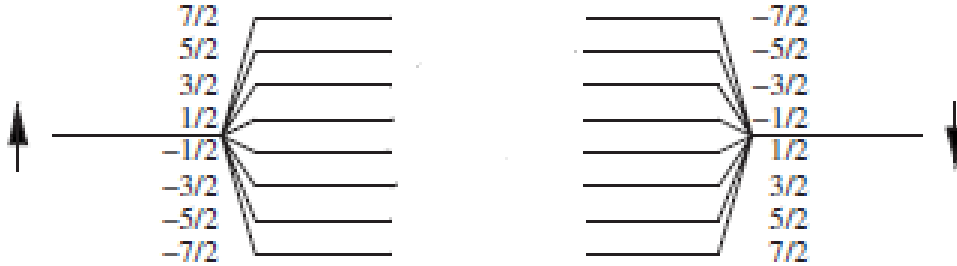


Figure 2.5: *Splitting of the electronic Ising states into electro-nuclear states due to the "longitudinal" part of the HF interaction (H_{HF}^{\parallel}). Illustration taken from Schechter and Stamp [17]*

From this diagram the importance of the inclusion of the HF structure can be understood, since at low enough temperatures $T \ll 0.2K$ the two lowest electro-nuclear levels act

as the Ising states, and these cannot be coupled by a transverse magnetic field alone as it cannot couple states of different nuclear spin.

In contrast the "transverse" HF term can couple \uparrow and \downarrow states of different nuclear spin as long as $\Delta m = I_{\downarrow}^z - I_{\uparrow}^z = 2$ (in second order of perturbation) or $\Delta m = 6$ (sixth order). However on its own, this term still doesn't produce coupling between the electro-nuclear ground states.

2.5 Applied Magnetic Field

Applying a magnetic field to the crystal is taken into account through the Zeeman effect:

$$H_z = -g_L \mu_B \vec{B} \cdot \vec{J}$$

where for the $J = 8$ configuration, the Wigner-Eckert theorem yields a Landé g factor $g_L = \frac{5}{4}$.

In the next subsections the effects of magnetic field components, along the crystallographic easy z axis (longitudinal field) or perpendicular to it (transverse field), are discussed separately.

2.5.1 Transverse Field

If the HF interaction is neglected, as proposed in several articles (e.g. [18, 19]), an applied transverse field should induce quantum fluctuations between the electronic Ising ground states and split the degeneracy to produce symmetric and anti-symmetric single ion states ($|\uparrow\rangle + |\downarrow\rangle$) and ($|\uparrow\rangle - |\downarrow\rangle$). Combined with an inter-ionic interaction for which all except the Ising like interaction terms are discarded (see section 2.1 and also reference [16]), this produces an effective transverse field Ising model:

$$H = \sum_{i \neq j} U_{ij}^{zz} \sigma_i^z \sigma_j^z - \Gamma(B^x) \sum_i \sigma_i^x \quad (2.5.1)$$

where Γ is the splitting between symmetric and anti-symmetric single ion states.

However at temperatures lower than the HF splitting ($T \ll 0.21K$), the HF structure has to be taken into account. As mentioned in section 2.4, transverse fields cannot couple between states of different nuclear spin by themselves, so that the coupling between the ground Ising states involves the transverse HF term and is greatly reduced ($\Gamma_{HF} \ll \Gamma_{no-HF}$)[17]. In fact the coupling between the ground Ising states becomes appreciable only when $B_x \simeq \frac{\Omega_0}{\mu_B J} \simeq 1.5T$ where the first excited electronic state Γ_2 becomes well hybridized with the ground electronic states [8, 16].

Furthermore as shown by Schechter and Laflorencie [7], for the dilute $\text{LiHo}_x\text{Y}_{1-x}\text{F}_4$ the Off Diagonal Dipolar interaction terms reduce the symmetry of the system, so that the Transverse Field Ising Model cannot adequately describe it (see section 3.1).

2.5.2 Longitudinal Field

A magnetic field applied in the longitudinal direction, splits the degeneracy between the electro-nuclear doublets and specifically between the Ising states linearly.

$$\Delta E = g_L \mu_B B^z \langle J_{\uparrow}^z \rangle - g_L \mu_B B^z \langle J_{\downarrow}^z \rangle = 2g_L \mu_B B^z \langle J_{\uparrow}^z \rangle \quad (2.5.2)$$

In other words, each of the levels of figure 2.5 develops into two branches linear in longitudinal field as shown in figure A.3.

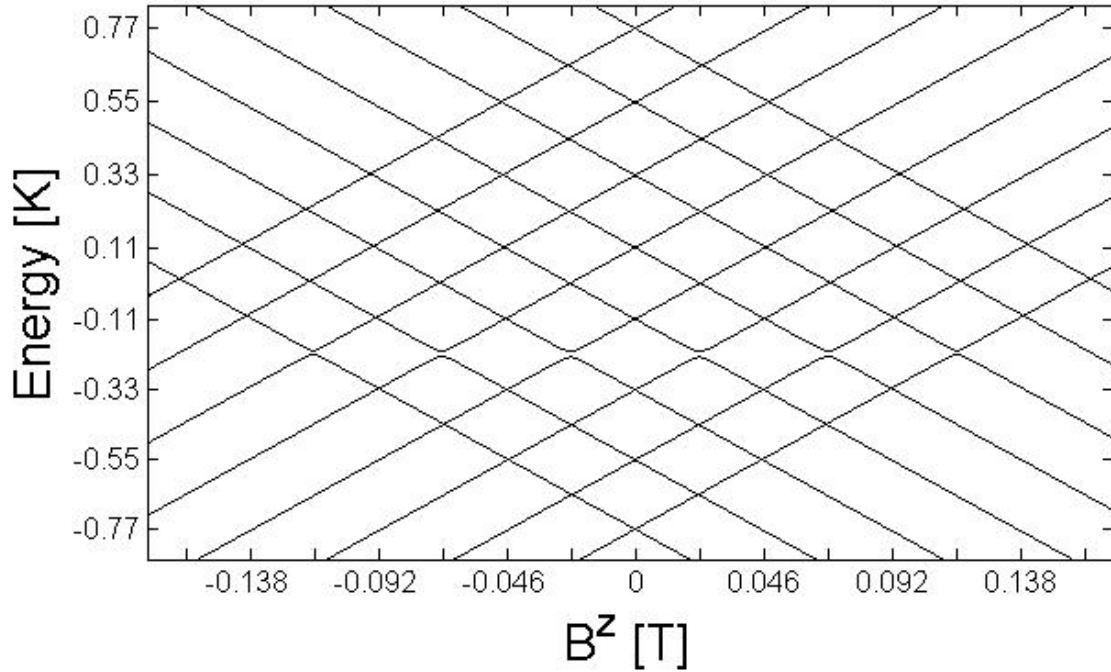


Figure 2.6: *Energy levels of the 8 X 2 lowest electro-nuclear levels as a function of an applied longitudinal magnetic field B^z (single ion picture).*

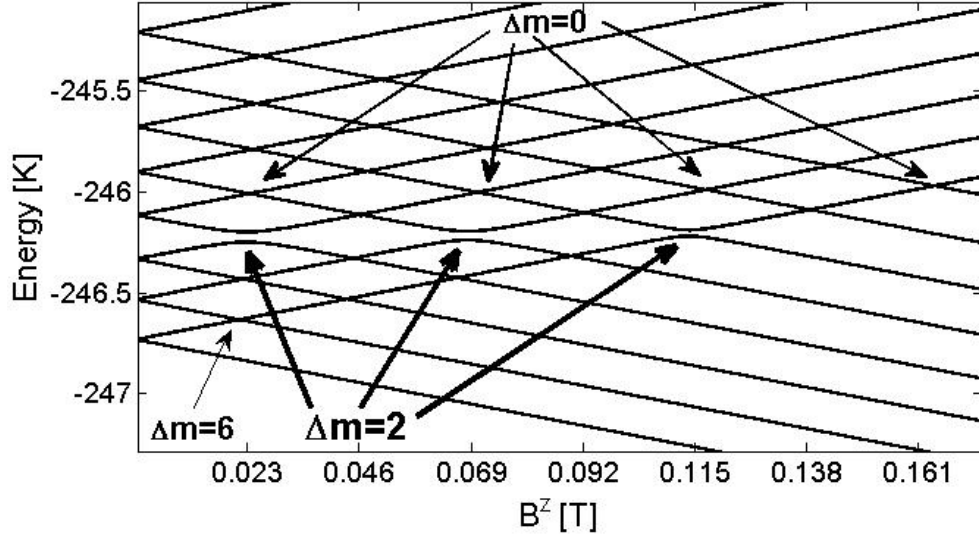


Figure 2.7: Zoom in of figure A.3 with avoided level crossing gaps intentionally exaggerated. Crossings specifically mentioned in the text are pointed out

The level crossings in figure A.3 are practically equally separated ($\Delta B^z = 23[mT]$) in the field axis due to the linearity of the Zeeman effect with field and the regularity of the HF splitting. Some of the energy level crossings are avoided level crossings. This can be seen quite easily for the case $\Delta m = I_{\downarrow}^z - I_{\uparrow}^z = 2$, where the coupling between levels through the transverse HF interaction is in second order. Avoided level crossings allow tunnelling between the corresponding states. In practice, there are more effects not taken into account in this model which couple the different states, thereby allowing more tunnelling possibilities.

Giraud et al. [15] conducted experiments in which a magnetic field was applied to a $\text{LiHo}_x\text{Y}_{1-x}\text{F}_4$ crystal parallel to the crystal's easy axis. The Ho concentration was very dilute ($x = 0.002$) in order to allow treatment of the ions singly, neglecting inter-ionic interactions. These experiments were conducted at temperatures equal to or lower than the energy splitting of the HF structure. The magnetic field was swept between $\pm 0.3T$ at various rates. A relatively low sweep rate of $\nu = 0.55[mT/sec]$ resulted in a hysteresis curve for the

magnetization of the sample as a function of the longitudinal field as shown in figure 2.8.

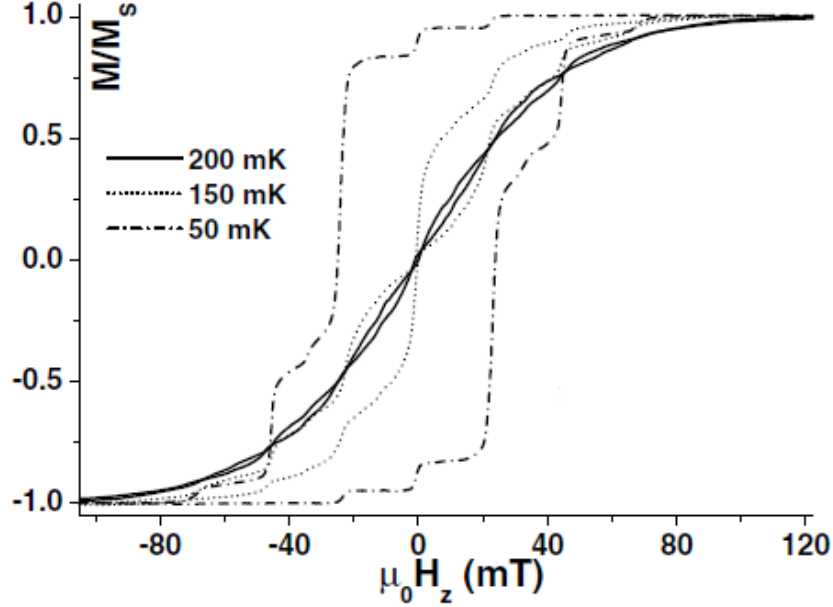


Figure 2.8: Magnetization with applied longitudinal field for $\nu = 0.55[mT/sec]$, showing hysteresis and magnetization steps. Magnetization is normalized to the maximum magnetization of the sample. Plot taken from Giraud et al. [15]

The explanation offered to this result was that at a large positive (or negative) magnetic field almost all of the magnetic ions were in the $|\uparrow - \frac{7}{2}\rangle$ (or $|\downarrow \frac{7}{2}\rangle$) state and tunneled away whenever the longitudinal field swept past an avoided level crossing. As only states of opposite magnetic moment cross, sweeping through resonances "flips" the ions thereby giving rise to magnetization steps. These magnetization steps are indeed found exactly where crossings are predicted.

At the higher temperatures it can be seen that thermal relaxation induces flips at all times, whereas at $T = 50mK$ it is evident through the neat steps that flipping mainly takes place at the resonances.

Better understanding of the tunnelling process can be gained from looking at the low

temperature susceptibility of the sample:

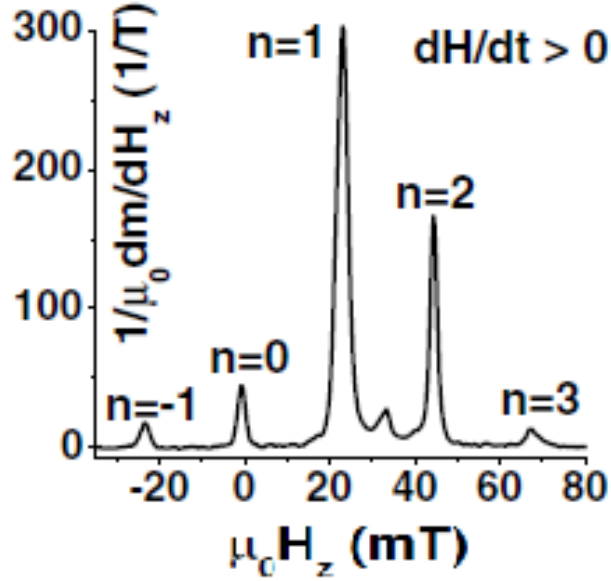


Figure 2.9: Susceptibility derived from the magnetization in the above plot for $T = 50[mK]$. Notice the magnetic field sweep direction from low to high field. Plot taken from Giraud et al. [15]

The sweep direction shown in the above plot corresponds to almost all of the ions initially occupying the $|\downarrow \frac{7}{2}\rangle$ state and gradually flipping to $|\uparrow\rangle$ states with different nuclear spins. The $n = -1$ crossing corresponds to a small but not negligible initial population of the $|\downarrow \frac{5}{2}\rangle$ state predicted by the Boltzmann ratio to be around $\frac{1}{60}$ of the overall magnetic ions. Here it is evident that even crossings which according to our model so far should not allow tunnelling (such as the $n = 0$ crossing), do so nonetheless.

A constant rate sweeping of the magnetic field as executed here naturally suggests an attempt at evaluating the tunnelling rate at each crossing according to the Landau-Zener approximation (see section F). However such an estimation produces tunnelling rates orders of magnitude lower than those witnessed in these experiments. Giraud et al. explained that the large tunnelling rates in the experiment are due to thermal activation. Through

thermal activation, ions are continuously excited to higher $|\downarrow\rangle$ states some of which are strongly coupled to $|\uparrow\rangle$ states (see section 2.4). The coupling for some of these states is so strong that at resonance, ions flip freely (see distinctly visible avoided crossings in figure 2.7). This means the flipping rate at these resonances is determined solely by the thermal activation rate. The relaxation time is given by $\tau = \tau_0 \exp(2\Delta E/k_B T)$ with a long τ_0 because spin-lattice relaxation time T_1 can be hours at very low temperatures and/or as a result of internal fields fluctuations.

A higher sweep rate of $\nu = 0.3[T/sec]$ at low temperature $T = 50[mK]$ resulted in the magnetization hysteresis curve of figure 2.10:

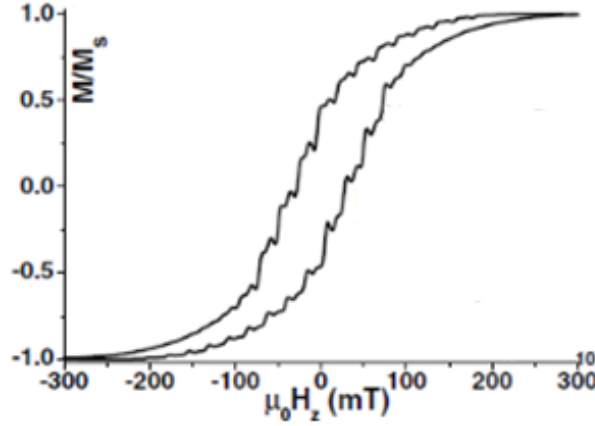


Figure 2.10: *Magnetization with longitudinal field for a high sweep rate $\nu = 0.3[T/sec]$ at $T = 50[mK]$. Plot taken from Giraud et al. [15]*

As expected, the higher sweep rate shows magnetization steps at the same field values as in the lower sweep rate, only of smaller size. This is because here the system sweeps faster past each resonance, limiting the amount of ions thermally excited during that time to the relevant levels. More importantly, figure 2.10 shows new and even smaller magnetization steps exactly midway between the resonances already mentioned.

We note for future reference that the presence of the many susceptibility peaks well

before the field sweeps past zero, implies that the system did not have enough time to equilibrate between sweeps (there is no significant pause between sweeps). In other words, at the start of each sweep, some of the ions are at Ising-states other than the ground one.

The susceptibility derived for this high sweep rate shows even more clearly the tunnelling at half integer n values. It also shows peaks at n values above 7 (see inset).

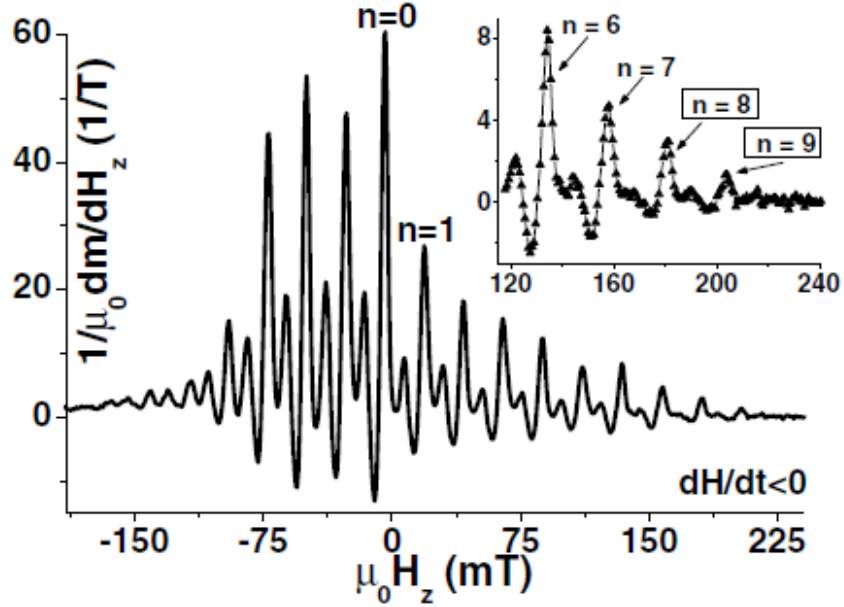


Figure 2.11: Susceptibility derived from the magnetization plot above (fig. 2.10) for a high sweep rate $\nu = 0.3[T/sec]$. Notice the Sweep direction is opposite to the one in the previous susceptibility plot (fig. 2.9). Plot taken from Giraud et al. [15]

These two results of tunnelling at half integer n and at $n > 7$ suggest the co-tunnelling of two ions.

In order to see more clearly why this is so, the Hilbert space of two ions is considered. In this two ions picture, each ion contributes its own Zeeman term, so that the slope with field can be either double that of the single ion picture (for two aligned ions $|\downarrow\downarrow\rangle$ or $|\uparrow\uparrow\rangle$) or practically zero (for anti-aligned ions $\alpha|\uparrow\downarrow\rangle + \beta|\downarrow\uparrow\rangle$).

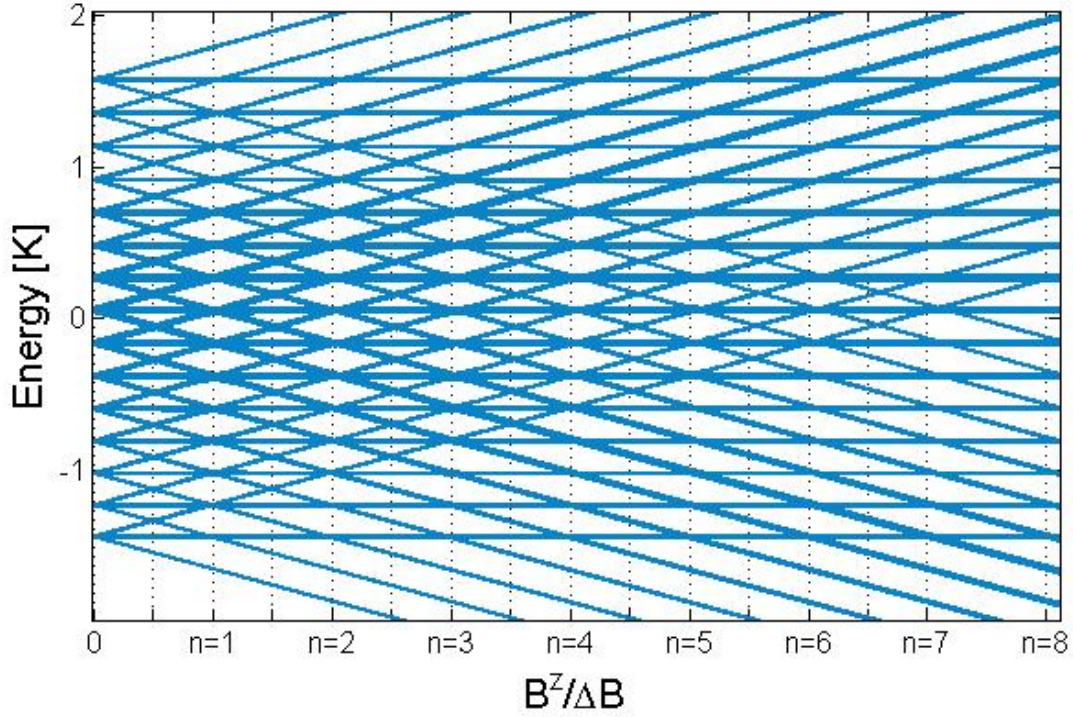


Figure 2.12: *Energy levels of the 256 lowest electro-nuclear levels (i.e. all the levels corresponding to both ions being either $|\uparrow\rangle$ or $|\downarrow\rangle$) as a function of an applied longitudinal magnetic field (two ion picture). No dipolar interaction. The field is given in units of the distance between single-flip resonances $\Delta B = 0.023[T]$*

Crossings between two sloped levels correspond to co-tunnelling of two ions (e.g. $|\downarrow_{\frac{7}{2}}\downarrow_{\frac{7}{2}}\rangle \rightarrow |\uparrow_{\frac{5}{2}}\uparrow_{\frac{7}{2}}\rangle$), while crossings of a sloped level with a horizontal one correspond to single ion flips as before. It is evident from this plot, that co-tunnelling produces additional crossings exactly between single ion crossings (half integer n).

It is worthwhile to note that crossings between $|\downarrow\downarrow\rangle$, $|\uparrow\uparrow\rangle$ and $|\downarrow\uparrow\rangle$ states can overlap, i.e. some of the peaks in susceptibility are generated both by ions tunnelling singly and by co-tunnelling (e.g. most of the $n = 1$ crossings).

Figure 2.12 also explains the susceptibility peaks at integer $n > 7$ through the addi-

tional crossings witnessed for the appropriate field values.

Notice that this is only a simplified picture as inter-ionic interactions were not included in the model yet and co-tunnelling cannot take place without such interactions. The introduction of such interactions will change the structure of the energy levels (depending on the relative positions of the ions) as discussed in the next sections.

In principle this analysis can be further expanded to include ion triplets and so on. However due to the strong dilution of the magnetic ions, most of them are significantly influenced only by one other such ion which is closer than all the others.

2.6 Dipolar Interaction

The Ho ions in the LiHoF4 crystal experience both superexchange and dipolar interactions. However even for nearest lattice neighbors (n.n.), the AFM exchange interaction has only half the magnitude of the dipolar interaction [14]. This is because the unfilled shell is an f shell which is spatially more contracted than other filled shells of the ion (in this case the $4d$ and $5p$ shells)[10]. Since exchange interactions decay exponentially and dipolar interactions decay cubically with distance, the ratio between the interactions grows fast, so that for all practical reasons the exchange interaction can be neglected and only the dipolar one should be taken into account (for next nearest neighbors, the exchange energy is 5% that of the dipolar interaction) [20, 14, 10, 21].

$$\begin{aligned}
H_{dipolar} &= \sum_{\substack{i \neq j \\ \alpha, \beta = x, y, z}} V_{ij}^{\alpha\beta} J_i^\alpha J_j^\beta \\
&= \sum_{\alpha, \beta = x, y, z} \sum_{j \neq i} \sum_i \frac{1}{2} g_L^2 \mu_B^2 \frac{\mu_0}{4\pi} \frac{|r_{ij}|^2 \delta_{\alpha, \beta} - 3 r_{ij}^\alpha r_{ij}^\beta}{|r_{ij}|^5} J_i^\alpha J_j^\beta
\end{aligned} \tag{2.6.1}$$

Depending on the positions of the two ions interacting, the dipolar term can prefer aligned magnetic moments (FM interaction), or anti-aligned (AFM interaction). The angle

of the position vector connecting the two ions relative to the z axis determines the interaction to be AFM for $54.7^\circ < \theta < 125.3^\circ$ and FM otherwise.

Chapter 3

Random Fields

3.1 Perturbation Theory

As discussed in section 2.5.1, the inability of the transverse field to couple two (single ion) time-reversed Ising states to first order, means that effects of the transverse field become noticeable only at second order of perturbation theory. This seems to suggest, in a naive approach, that the effects of the transverse field are proportional to $(B^x)^2$ [14].

Schechter and Lafflorencie showed [7] using second order degenerate perturbation theory that the combination of Off Diagonal Dipolar (ODD) terms and a transverse magnetic field brings about an effective longitudinal field whose magnitude and direction depend on the relative positions of the magnetic ions. Since the magnetic ions are distributed randomly throughout the possible lattice sites, the effective field is in fact a random longitudinal magnetic field (which turns out to be linear in B^x for small B^x). An intuitive perspective of why the combination of a transverse field and the dipolar interaction breaks the symmetry to flips of spins along the z axis is given in appendix B.

A perturbative expansion similar to that of Schechter and Lafflorencie was carried out with the specifics of the $\text{LiHo}_x\text{Y}_{1-x}\text{F}_4$ crystal in mind (see detailed derivation in appendix

B). The lowest energy unperturbed eigenstates of the crystal are '*Global-Ising states*' for which all the ions are in one of the (single ion) electro-nuclear Ising states (e.g. $|\uparrow - \frac{5}{2}\rangle$). We expand these states to find energy splittings as a function of transverse field along the x axis. Specifically the splittings form between any two such states, which are degenerate and related by $J_k^z \rightarrow -J_k^z$ and $I_k^z \rightarrow -I_k^z$ symmetry. The ground states, for which each of the Ho ions is in one of the Ising states $|\uparrow - \frac{7}{2}\rangle$ or $|\downarrow \frac{7}{2}\rangle$, in such a way as to minimize the longitudinal dipolar term, can be taken as a representing example of such states. The energy splitting is given in eq. 3.1.1 to leading order.

$$\delta E = 2g_L\mu_B \sum_k \left(\frac{4\eta}{\Omega_0} \sum_{i \neq k} V_{ki}^{zx} B^x \right) \langle J_k^z \rangle \quad (3.1.1)$$

where the quantity $\eta = |\langle \Gamma_2 | J^x | \uparrow \rangle|^2 = 5.62$ is found numerically using the code in appendix G.1.

This energy splitting has the form of a sum of, single ion, longitudinal Zeeman splittings (see eq. 2.5.2)

$$\delta E = 2g_L\mu_B \sum_k B_{k,eff}^z \langle J_k^z \rangle \quad (3.1.2)$$

and we thus deduce effective longitudinal fields

$$B_{k,eff}^z = \frac{4\eta}{\Omega_0} \sum_{i \neq k} V_{ki}^{zx} B^x \quad (3.1.3)$$

Each of these effective longitudinal fields has a magnitude particular to the (dipolar interaction experienced by the) relevant Ho ion and can thus be considered as a random longitudinal field due to the spatial disorder of the magnetic ions. As is evident, the magnitude of all these random fields increases linearly with B^x .

A rough estimate is that this analysis is valid as long as corrections of first order to the unperturbed states are small $g_L\mu_B\sqrt{\eta}B^x \ll \Omega_0$ (or roughly $B^x \ll 2.5[T]$). However there are more constraints such as that this analysis is of course not valid near level crossings.

As the effective field for each ion is dependant on the lattice positions of its neighboring ions, these random fields are, strictly speaking, correlated. However for large enough domain sizes Imry-Ma behaviour is nevertheless obtained as was shown explicitly for $\text{LiHo}_x\text{Y}_{1-x}\text{F}_4$ with $(1-x) \ll 1$ where the correlations are most significant [8].

While not directly relevant to this work, it is interesting to note that the original analysis of this result goes on to conclude that any finite transverse field destroys the Spin Glass phase in $\text{LiHo}_x\text{Y}_{1-x}\text{F}_4$ so that there is no quantum phase transition for this system [7].

In order to compare the perturbative result to the numerical result in the next section, we give the splitting up to third order perturbation expansion for nearest lattice neighbors $\vec{r}_{n.n.} = (\frac{a}{2}, 0, \frac{c}{4})$ expanding the states $|\uparrow -\frac{7}{2} \uparrow -\frac{7}{2} \rangle$ and $|\downarrow \frac{7}{2} \downarrow \frac{7}{2} \rangle$:

$$\delta E^{(2)} + \delta E^{(3)} = 0.8169B^x - 0.0034B^x = 0.8135B^x[K] \quad (3.1.4)$$

where the second order here includes corrections due to the dipolar and HF interactions and also electronic levels higher than Γ_2 (see appendix B for details)

3.2 Beyond Perturbation Theory

After reviewing the analytical derivation of the random field in the previous section, we now aim at finding the random field beyond perturbation theory. This is done through exact numerical diagonalization of a *full* two ions Hamiltonian for various ion pairs:

$$H_{2Ho} = H_{CF} + H_{HF} + H_{dipolar} + H_{zeeman}$$

with an applied transverse magnetic field along one of the crystallographic "hard" axes chosen as the x axis. Applied longitudinal field is disregarded throughout this section.

Such a matrix is 18496 X 18496 big (17 electronic states times 8 nuclear states for each ion, squared for the two ions). A standard Matlab diagonalization process was not feasible as it requires 5GB of memory simply to store a single such matrix. Instead an iterative

process was used. This was possible due to the sparsity of the Hamiltonian matrix. That is the matrix is composed mostly of zeros which were not stored. Iterative methods allow treatment of only the non-zero matrix components in the diagonalization process. Another advantage of iterative diagonalization is that it can be much faster than the standard process (under certain limitations). See appendix C for more details.

The energy levels for transverse fields between 0 and $2T$ are shown for nearest lattice neighbor pairs as an example.

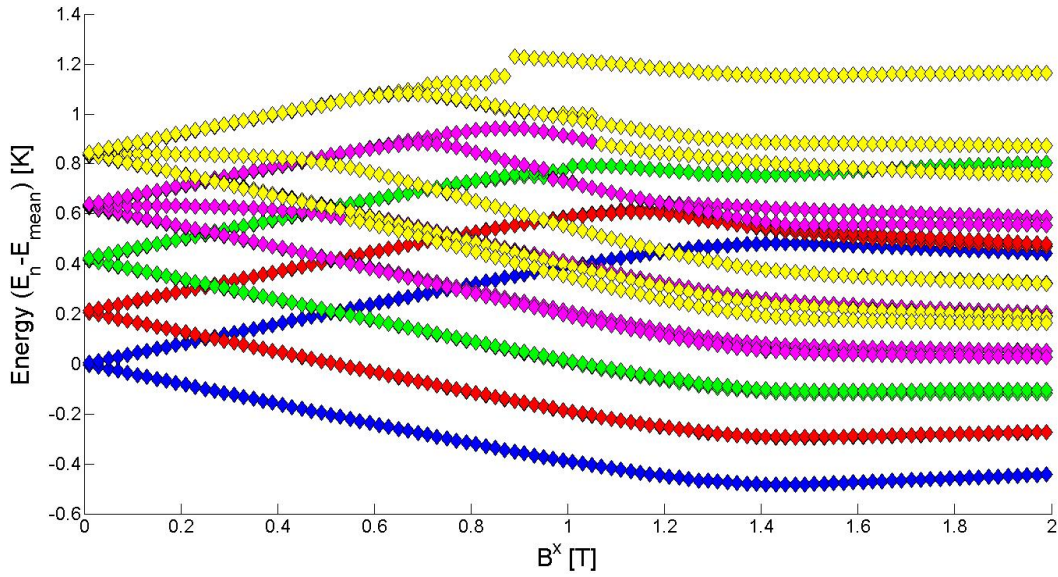


Figure 3.1: Energy levels Vs. B^x for *n.n.* pairs at relative positions $\vec{r} = (\pm\frac{1}{2}a, 0, \frac{1}{4}c)$

Explanatory notes:

- Only the first 32 levels are shown for clarity.
- The color scheme is determined according to the degeneracies at zero field. Each diabatic state should retain its color as B^x changes.
- All energies are relative to the mean between the states starting (at zero field) as $|\uparrow -\frac{7}{2} \uparrow -\frac{7}{2} \rangle$ and $|\downarrow \frac{7}{2} \downarrow \frac{7}{2} \rangle$ (i.e. relative to the mean between blue lines).

- Similar relevant plots for other pairs can be found in appendix D.

In the following, for reasons of convenience, the states are referred to according to their characterization at zero transverse field even though their composition changes with field. For example the ground state in the above figures is referred to as the $|\uparrow -\frac{7}{2} \uparrow -\frac{7}{2}\rangle$ state even though at non-zero transverse fields the eigenstate actually mixes components of other states in this basis as well.

Notice that even though the relevant eigenstates acquire non-zero $\langle J^x \rangle$ and $\langle J^y \rangle$ expectancy values for non-zero transverse fields (see below), they are still magnetic Ising states since they can be characterized by their $\langle J^z = \pm const \rangle$ value (for each B^x value).

The effective longitudinal field for such a pair is extracted from the energy difference between the $|\uparrow -\frac{7}{2} \uparrow -\frac{7}{2}\rangle$ and $|\downarrow \frac{7}{2} \downarrow \frac{7}{2}\rangle$ (blue) levels as discussed in the previous section (eq. B.0.10) and elaborated below.

We note that the energy spectrum for AFM pairs has states of anti-aligned ions (i.e. containing terms: $|\uparrow\downarrow\rangle$) as ground states (for small enough fields, see e.g. fig. D.2 in appendix D). While such states do not significantly change their energy as a function of B^x relative to their zero field energy, this does not contradict the validity of the effective longitudinal field model since their position in the energy spectrum relative to other states does change.

A plot (Fig. 3.2) of the energy difference between the $|\uparrow -\frac{7}{2} \uparrow -\frac{7}{2}\rangle$ and $|\downarrow \frac{7}{2} \downarrow \frac{7}{2}\rangle$ states shows an interesting feature. The practically linear curve of the energy difference extending to transverse field values of above $1T$, i.e. well beyond second order perturbation theory, is a new and unpredicted result. The linearity is due to the cancellation by symmetry of the square term $(B^x)^2$ (and indeed all even power terms), and due to smallness of the cubic term $(B^x)^3$ which only survives at the 4th order of expansion. This curve $\delta E_{numerical} = 0.80B^x + 0.02(B^x)^3[K]$ is comparable to the 3rd order perturbative result from the previous section (eq. 3.1.4) $\delta E_{perturbative} = 0.81B^x[K]$.

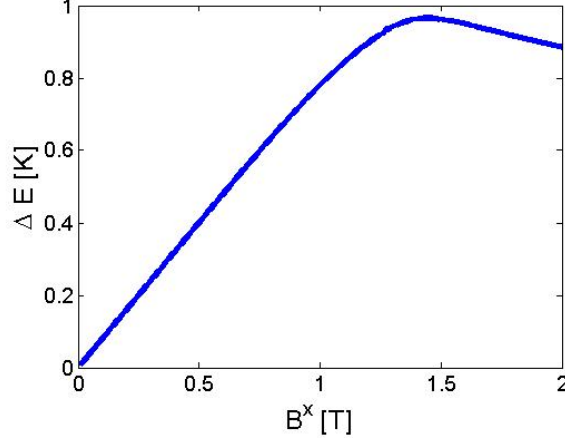


Figure 3.2: Energy difference between the $|\uparrow -\frac{7}{2} \uparrow -\frac{7}{2}\rangle$ and $|\downarrow \frac{7}{2} \downarrow \frac{7}{2}\rangle$ for n.n. pairs (with relative positions $\vec{r} = (\pm\frac{1}{2}a, 0, \frac{1}{4}c)$)

It is important to note at this time that at high enough transverse fields (e.g. $B^x = 1.4T$ for n.n. pairs and $B^x = 1.3T$ for 3rd pairs), it becomes increasingly hard to keep track of the diabatic states through level crossings (see appendix G.4 for details about tracking diabatic states). Therefore the color scheme of the energy levels should only be relied upon for moderate field values (i.e. the diabatic states are identified correctly only at the field range where the energy difference shows a linear curve).

The effective longitudinal field can be derived from the energy difference as in eq. 2.5.2 (expanded for two ions labelled 1 and 2):

$$\Delta E = g_L \mu_B B_{eff}^z (< J_1^z >_{\uparrow} + < J_2^z >_{\uparrow} - < J_1^z >_{\downarrow} - < J_2^z >_{\downarrow}) \quad (3.2.1)$$

where we considered that (unlike in the perturbative derivation) the $< J_{1,2}^z >$ expectancy values, can be different for states of two ions up or two ions down (see fig. 3.3).

Isolating the effective field gives:

$$B_{eff}^z = \frac{\Delta E}{g_L \mu_B (< J_1^z + J_2^z >_{\uparrow} - < J_1^z + J_2^z >_{\downarrow})} \quad (3.2.2)$$

Notice that the expectancy values for $< J^z >$ change with transverse field (Fig. 3.3).

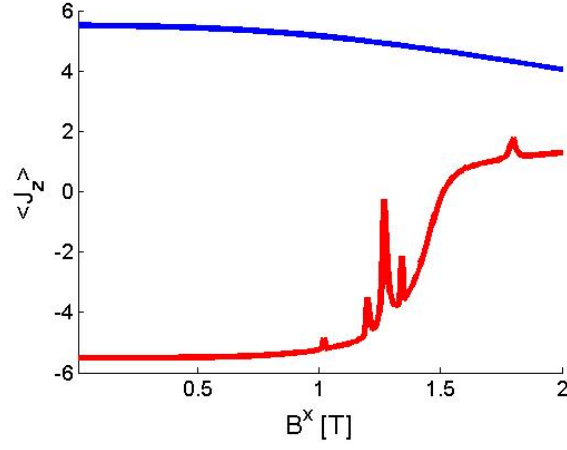


Figure 3.3: $\langle J_1^z \rangle$ and $\langle J_2^z \rangle$ (identical) Vs. B^x for $n.n$ pairs. Blue line is for $|\uparrow -\frac{7}{2} \uparrow -\frac{7}{2}\rangle$ and red for $|\downarrow \frac{7}{2} \downarrow \frac{7}{2}\rangle$

The sudden jumps in $\langle J^z \rangle$ testify to level crossings where the relevant eigenstates are a mix of two diabatic states with different $\langle J^z \rangle$ (the $|\uparrow -\frac{7}{2} \uparrow -\frac{7}{2}\rangle$ state does not cross any other state at positive fields leading to the smooth curve in the above figure).

The effective longitudinal field calculated as discussed above is:

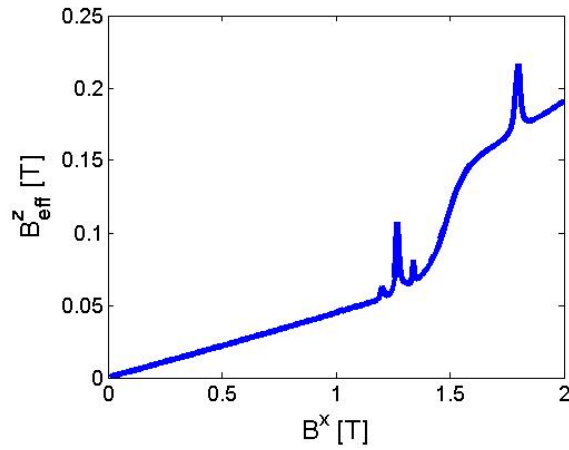


Figure 3.4: Effective longitudinal field Vs. B^x for $n.n.$ pairs (with relative positions $\vec{r} = (\pm\frac{1}{2}a, 0, \frac{1}{4}c)$).

A fit for the linear segment produces $B_{eff}^z = 0.044B^x$.

The sharp peaks are due to the anomalies in the $\langle J^z \rangle$ values for eigenstates near level crossings as explained above (fig. 3.3). They should not be taken as anomalies in the effective field, as the effective field should be determined by the properties of the diabatic states and not the eigenstates. That is, the above plot shows the correct effective field only away from level crossings where the diabatic states and the eigenstates are equivalent. The effective field is not calculated using the diabatic states for technical reasons; however it can be extrapolated for these anomalous regions from the linear fit.

Again it is advised not to rely on the calculated effective field beyond the region where the energy difference is linear, due to difficulties in tracking diabatic states as mentioned above.

A unified plot of the random fields for different pairs is convenient for comparison (Fig. 3.5).

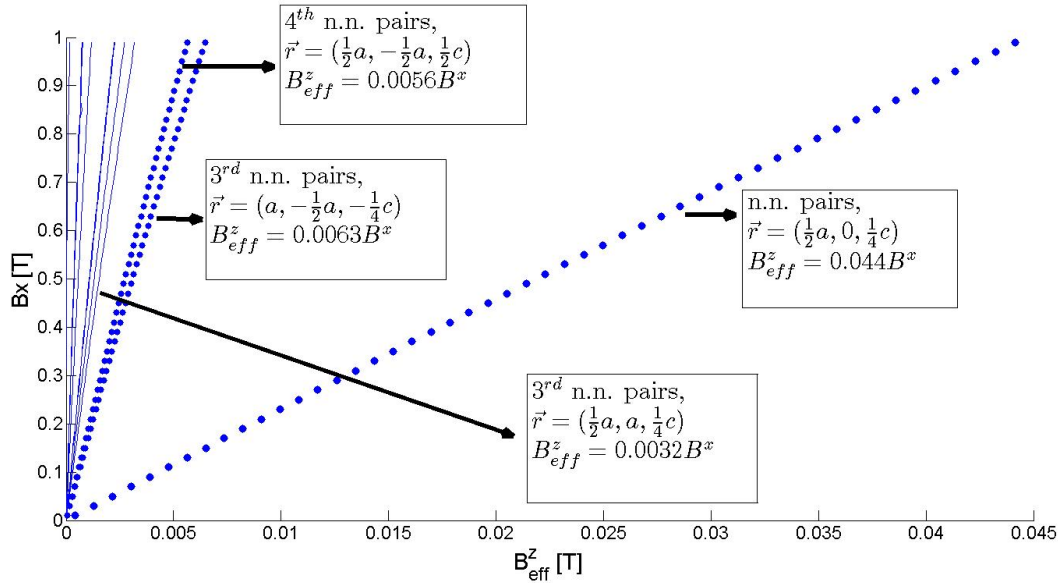


Figure 3.5: Comparison of the effective longitudinal fields for lattice neighbors of the 8 shortest distances. Notice the change in the axes compared to the previous plot

The axes are switched in Fig. 3.5 as compared with fig. 3.4 for compatibility to plots in the next chapter, having a horizontal B^z axis. The effective longitudinal fields for the 3 strongest fields which are the ones we propose to measure in experiment, are accentuated (bold dots instead of thin lines).

Chapter 4

Proposed Direct Random Field Measurement

As a central application of our exact calculations of the effective longitudinal field experienced by pairs at various relative lattice positions, we propose methods for measuring the Random Field through variations on the experiments performed by Giraud et al. [15] (see section 2.5.2). Such experiments would be of particular significance as they would constitute the first direct measurement of a Random Field in a FerroMagnetic Ising-like system.

We suggest three different variations to the experimental process discussed in section 2.5.2, each with its own advantages. We first discuss an almost identical process to the original experiment with the addition of a constant applied transverse field. This should produce the desired results in a graphical representation similar to the original (i.e. magnetization hysteresis and the susceptibility derived thereof). The next variation is to sweep the longitudinal field adiabatically slow (with a constant transverse field as before), so that the system evolves through equilibrium states instead of the dynamical process in the original experiment. Finally we suggest adiabatically sweeping the *transverse* field in a constant applied longitudinal field.

We note that all the plots in this chapter are approximated using the linear fits to the energy differences and effective fields found for the different pairs.

4.1 Adding a Constant Transverse Field - Dynamical

Repeating Giraud's experiments, with the addition of a constant applied transverse field, is expected to shift the resonances by the effective fields found in the previous section and split the peaks in the susceptibility plot. More specifically, the susceptibility plot should show the original peaks of previous experiments, plus small peaks thus shifted from each of the original peaks (both "single-flip" and co-tunnelling peaks) and in both directions (due to the symmetry of the crystal).

As mentioned before, different ion pairs (of different relative positions between the two ions) experience different effective longitudinal fields. At transverse fields of up to $1.2T$ (for which the characterization of the states as Ising-like is clear) most pairs experience negligible effective fields which means the shifted resonances would not be discernible from the original ones witnessed by Giraud (due to broadening). However the pairs of near enough lattice positions, can experience large enough effective fields, to produce distinct shifted peaks even within this $1.2T$ range. Specifically we consider for these purposes, the n.n. pairs and the 3rd and 4th n.n. pairs. The 2nd and 5th n.n. pairs do not experience an effective field as explained in appendix D.

These shifted peaks of susceptibility are expected to be small compared to the original peaks. This is because in such a strong Ho dilution, only a small number of Ho ions would produce such crowded pairs. For this reason it is important to choose applied transverse field values with care so that the shifted peaks are in fact well shifted and discernible from the original peaks. Optimal visibility of the shifted peaks should be achieved when such peaks are at the valley of susceptibility between original peaks (between a main co-tunnelling peak and a "single-flip" peak).

In their 2003 article [22] Giraud et al. presented the results of another experiment showing better resonance resolution through ac susceptibility measurements (Fig. 4.1).

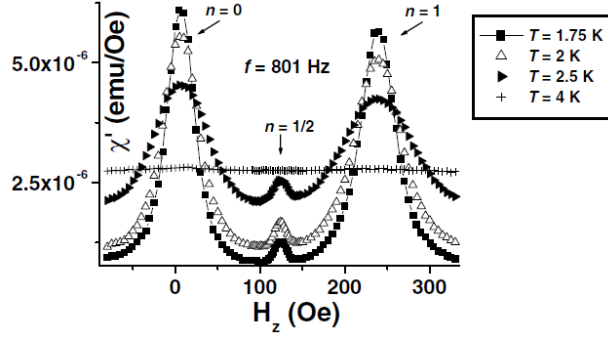


Figure 4.1: *The ac susceptibility measured for a $\text{LiHo}_x\text{Y}_{1-x}\text{F}_4$ crystal with $x = 0.001$ at different temperatures. Measurements were performed with a quantum design MPMS SQUID magnetometer, using a 4 Oe-amplitude excitation field at $f = 800\text{Hz}$ frequency. Figure taken from Giraud et al. [22]*

From these results we deduce that the minimum of such a valley is around 1/4 of the way from a co-tunnelling peak to the adjacent "single-flip" peak. Thus the optimal effective field values should be:

$$B_{eff,optimal}^z = \left(\frac{1}{4} + \frac{1}{2}k\right) \cdot \frac{\Delta B^z}{2} \quad (4.1.1)$$

with integer k and the inter-peak distance being $\frac{\Delta B^z}{2} = 0.0115$. We keep in mind the restriction of the previous chapter on the transverse field range at which this analysis is valid ($B^x < 1.3[T]$)

Of course we cannot place all the shifted peaks at minima of such valleys at the same time, as each pair is shifted by a different amount. Thus we might have to repeat the experiment at different transverse field values to observe shifted peaks related to different pairs.

Note that the peaks' shape and width are also temperature dependent (at least for

"single-flip" peaks), as seen clearly in the above figure (4.1) and as established in section 2.5.2 (see also [22]).

A convenient method, to find optimal transverse field values to be applied, is by using the code supplied in appendix G.5. This code employs a process similar to the 'manipulate' function in Mathematica (a plot with varying parameters controlled manually). This "interactive" plot shows (for a given B^x) the predicted positions of the shifted peaks (for the 1st, 3rd and 4th n.n. pairs) relative to the original peaks. A slider control determines B^x (see example in fig. 4.2).

At this point it should be emphasized that our calculations assume the transverse field is applied along one of the ("hard") crystallographic axes. A generalization to any other direction can be easily obtained. Another consideration is that we calculated the effective field based on the energy difference between the $|\downarrow \frac{7}{2} \downarrow \frac{7}{2}\rangle$ and $|\uparrow -\frac{7}{2} \uparrow -\frac{7}{2}\rangle$ while a more careful calculation should consider the energy difference between $|\downarrow \frac{7}{2} \downarrow \frac{7}{2}\rangle$ and a $|\uparrow\uparrow\rangle$ level of different nuclear spins for each level crossing in B^z (i.e. for different $n = \frac{1}{2}, 1, \frac{3}{2}, \dots$ according to the levels participating in the crossing). This is the same sort of correction suggested for the perturbative analysis in eq. B.0.12 (due to the HF interaction) and can lead to a small correction to the B^z position for resonances of large n (e.g. $n=7$).

As a simple example we consider an applied transverse field of $B^x = 0.072[T]$. This field value should produce optimal visibility of the shifted peaks related to n.n. pairs. To be precise, the n.n. pairs separated by $\vec{r} = (0, \pm\frac{1}{2}a, -\frac{1}{4}c)$ (defined as 'second' orientation in appendix A.1) experience no effective field and their resonances do not shift. The pairs separated by $\vec{r} = (\frac{1}{2}a, 0, \frac{1}{4}c)$ experience a positive effective field ($B_{eff}^z = 0.0032[T]$) and their resonances shift in the negative direction of B^z . Similarly the resonances of the pairs separated by $\vec{r} = (-\frac{1}{2}a, 0, \frac{1}{4}c)$ shift equally far in the positive direction. We note that this means each such shifted resonance corresponds to just one kind of n.n. pairs flipping (out of 4). The resonance shifts for all other pairs is indiscernible for this low transverse field value.

Figure 4.2 was made using the code in appendix G.5. The blue lines representing the

original peaks are illustrations drawn for perspective only and should *not* be taken as a prediction for the size and functional form of the real peaks.

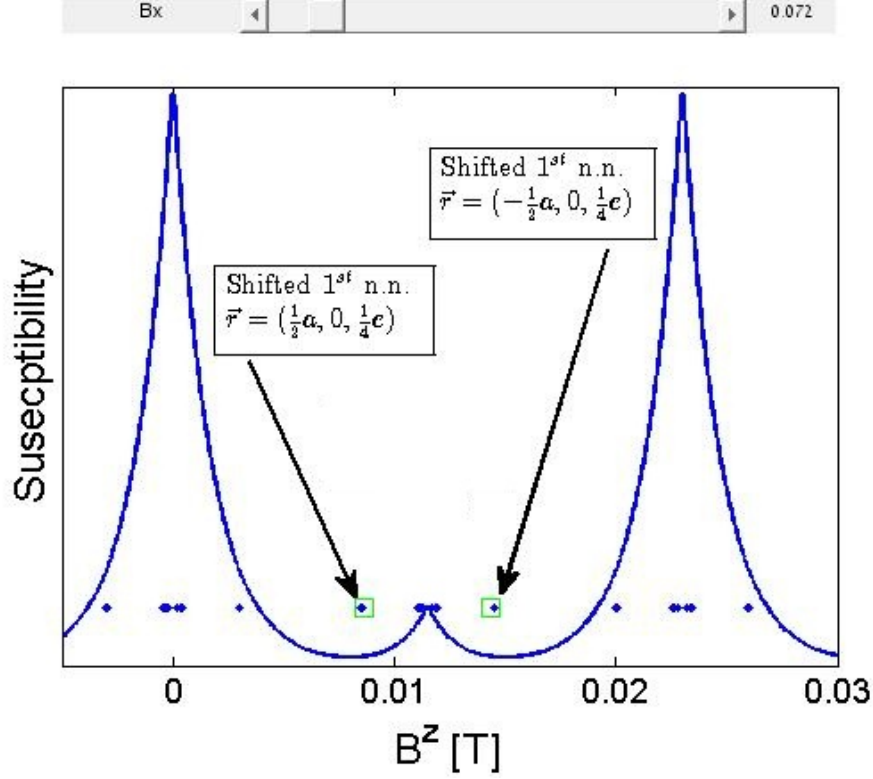


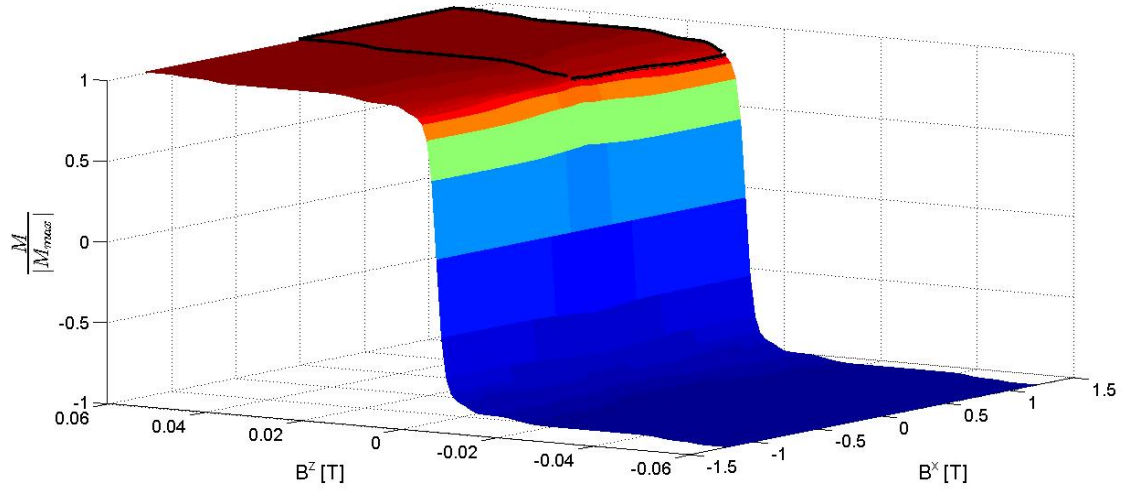
Figure 4.2: Predicted positions of shifted susceptibility (χ^{zz}) peaks for $B^x = 0.072[T]$. Blue lines illustrate the original peaks for perspective. Green squares mark valley minima. Blue dots represent shifted peaks positions. The shifted peaks which are expected to be clearly visible in experiment are noted. All other shifted peaks (dots) in this plot are expected to simply widen the unshifted peaks.

The shifted peaks shown should appear to either side of *any* of the original *co-tunnelling* peaks. They are expected to be much smaller than the original co-tunnelling peaks since each such peak corresponds to just the n.n. pairs flipping (and in fact only 1 out of every 4 n.n. pairs as mentioned before).

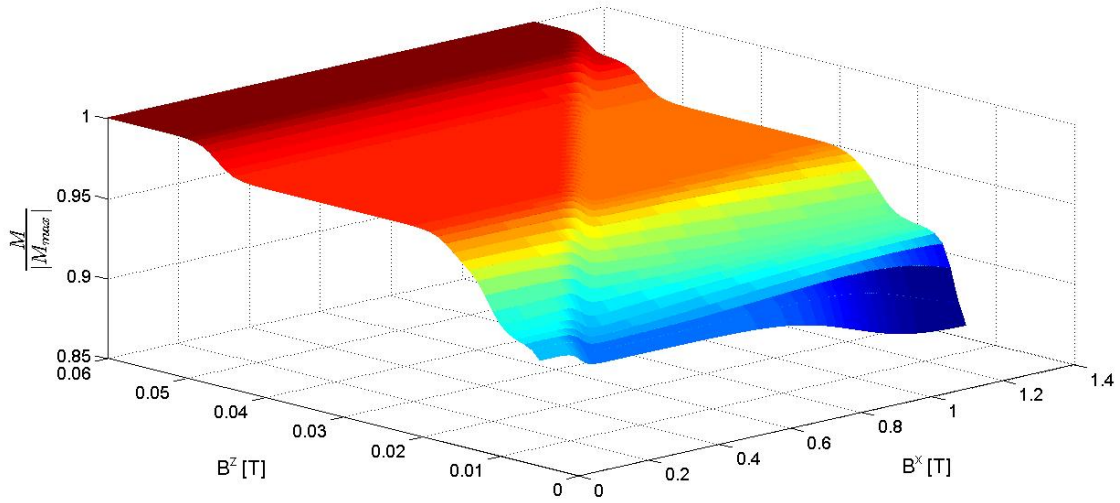
Another such case of optimal visibility for shifted peaks can be found in appendix E for $B^x = 0.46[T]$. This example also features the shifted peaks of 3rd and 4th n.n. pairs. In fact resonances of these farther pairs only start to separate from an unshifted co-tunnelling peak for $B^x \geq 0.4[T]$. The ability to precisely predict the position of these peaks is a direct consequence of our exact calculation of the effective longitudinal field beyond perturbation theory. Appendix F discusses the functional profile of the quantum ($T = 0$) transitions (magnetization steps and susceptibility peaks) at shifted resonances in this kind of experiment.

4.2 Adiabatic Sweeping

The above method has the disadvantage of producing results for which the distinctness of the shifted resonances against the 'noise' of the unshifted resonances is highly sensitive to experimental parameters (such as transverse field, sweep rate, and measurement resolution). A more stable version of this experiment is to sweep an applied field adiabatically slow so that the system stays at (a momentary) equilibrium throughout the sweep. In other words, in adiabatic sweeping most of the pairs occupy their momentary (two ions picture) ground state (see for example the ground states in Fig. 4.6). Excited states are only occupied according to the Boltzmann ratio so that away from crossings involving the (momentary) ground state (where the gap to the first excited level is small), their population is exponentially small compared to the ground state. Figures 4.3 through 4.5 show the magnetization and susceptibility predicted at equilibrium as a function of both B^z and B^x .



(a)



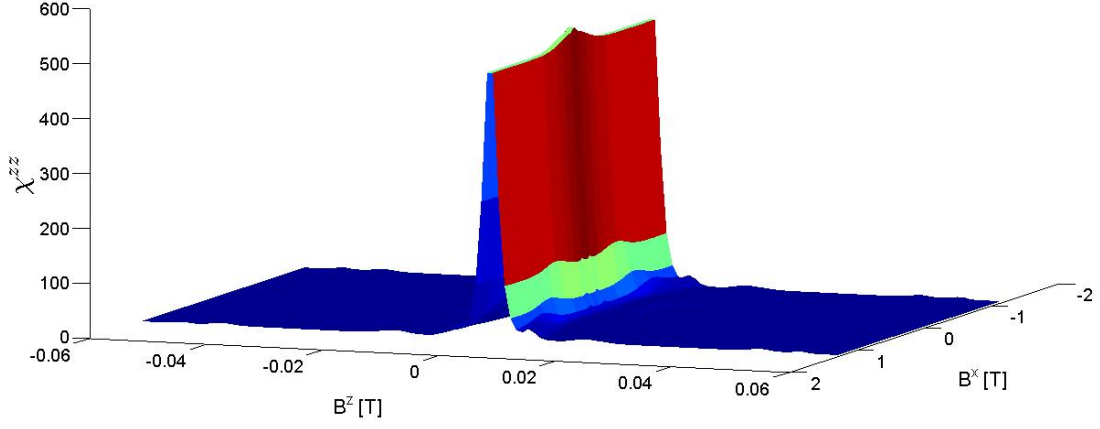
(b)

Figure 4.3: *Predicted Magnetization for applied fields:*

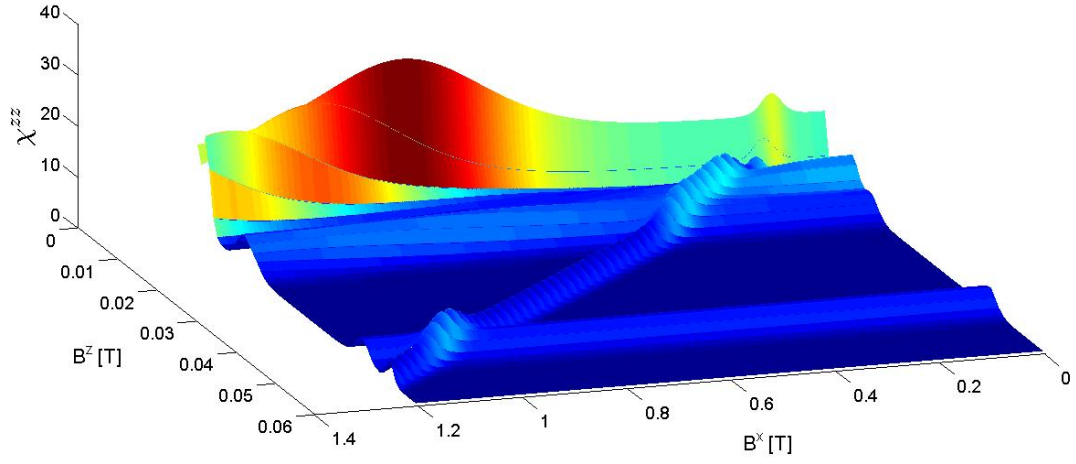
a) $-0.06 < B^z < 0.06T$; $-1.2 < B^x < 1.2T$.

b) $0.005 < B^z < 0.06T$; $0 < B^x < 1.2T$. (*zoom in*)

$T = 10[mK]$, $x = 0.005$ (*broadening is not taken into account here*).



(a)



(b)

Figure 4.4: Predicted Susceptibility to B^z ($\frac{\partial M^z(B^x, B^z)}{\partial B^z}$) for applied fields:

a) $-0.06 < B^z < 0.06T$; $-1.2 < B^x < 1.2T$.

b) $0.004 < B^z < 0.06T$; $0 < B^x < 1.2T$. (zoom in)

$T = 10[mK]$, $x = 0.005$ (broadening is not taken into account here).

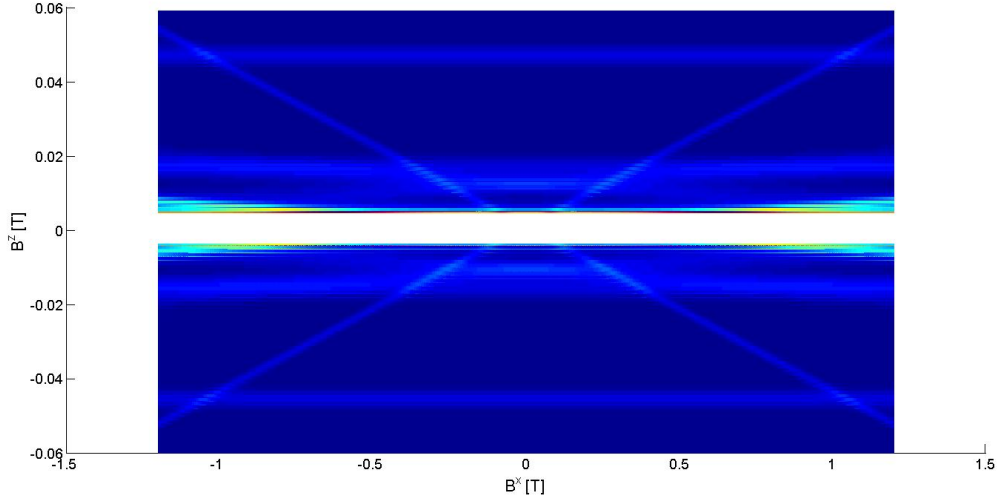


Figure 4.5: *Projection of the susceptibility (χ^{zz}) on the $B^x B^z$ plane for applied fields $-0.06 < B^z < 0.06T$; $-1.2 < B^x < 1.2T$. The area of the big susceptibility peak at zero longitudinal field ($-0.004 < B^z < 0.004T$) was cut off for better visibility of areas outside this big peak. $T = 10[mK]$, $x = 0.005$ (broadening is not taken into account here).*

Note that here we used a constant value $J^z = 5.5$ even though we explicitly showed that J^z changes with B^x in section 3.2 (fig. 3.3). This was done to produce clearer plots where magnetization steps are more easily visible, since we use these plots mainly as a guide to finding the desired parameters for experiment. Refined plots, taking into account a varying $J^z(B^x)$, can be found in appendix E.

The diagonal magnetization step (susceptibility peak) clearly visible in figures 4.3b, 4.4b and especially 4.5 corresponds to the shifted resonances of n.n. pairs and is linear in B^x as expected.

Guided by these plots, we suggest two more ways for observing shifted resonances. The plot for the projection of the susceptibility (χ^{zz}) on the $B^x B^z$ plane (fig. 4.5) will be presented again for each of the following predictions with the appropriate field values clearly marked in order to give perspective as to their respective differences.

4.2.1 Adding a Constant Transverse Field - Equilibrium

We now discuss an experiment similar to the original one by Giraud's only with an adiabatic sweep of the longitudinal field and an added constant transverse field. For comparison we shall first discuss the predicted results in the absence of a transverse field. Such a slow sweep would produce one very big magnetization step at zero field and several small ones on either side (see figure 4.7). The Big step at and around zero field includes the flipping of almost all the spins (both FM and AFM pairs). All of the FM ion pairs contribute to the big step, because they all have only a single ground state resonance which is exactly at zero field as illustrated in figure 4.6a (though broadening and finite measurement resolution should be taken into account). The AFM pairs on the other hand have two ground state resonances away from zero field (figure 4.6b), though most of them are swallowed up in the wide zero field step except a few which have a dipolar interaction larger than the width of the zero field step (e.g. 2nd n.n. pairs). The small steps are related to the resonances of these exceptional AFM pairs. This means by the way that at these resonances only one ion in the pair flips.

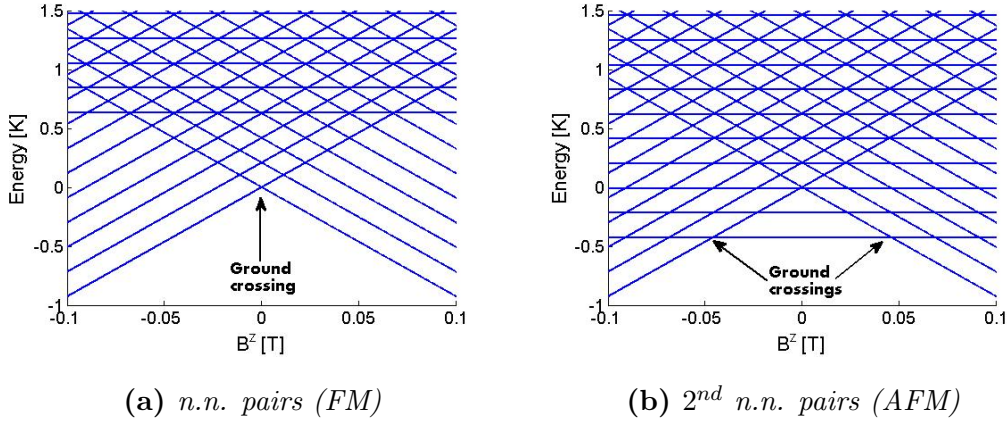


Figure 4.6: Examples of energy levels as a function of B^z ($B^x = 0$) for FM and AFM pairs. Crossings involving ground levels are noted

We therefore treat specifically only six such resonances which are separated by more

than $10mT$ from zero field. These six resonances belong to the AFM 2nd, 3rd and 5th n.n. pairs and appear at field values $\pm 46.2mT$, $\pm 11.5mT$ and $\pm 16.3mT$ respectively. Excluding only these six resonances from the zero field magnetization step, means that the zero field step corresponds to 92% of all the Ho ions in the crystal flipping (assuming Ho dilution $x = 0.005$).

The predictions of figures 4.7 through 4.15 take into account a temperature of $T = 10[mK]$, Ho dilution $x = 0.005$ and a broadening of $1mT$ due to both spin-spin interactions with farther Ho ions and HF interactions with Fluorine ions. $J^z(B^z)$ dependency was not taken into account since it is not significant for the relatively small transverse fields used in this section (see appendix E).

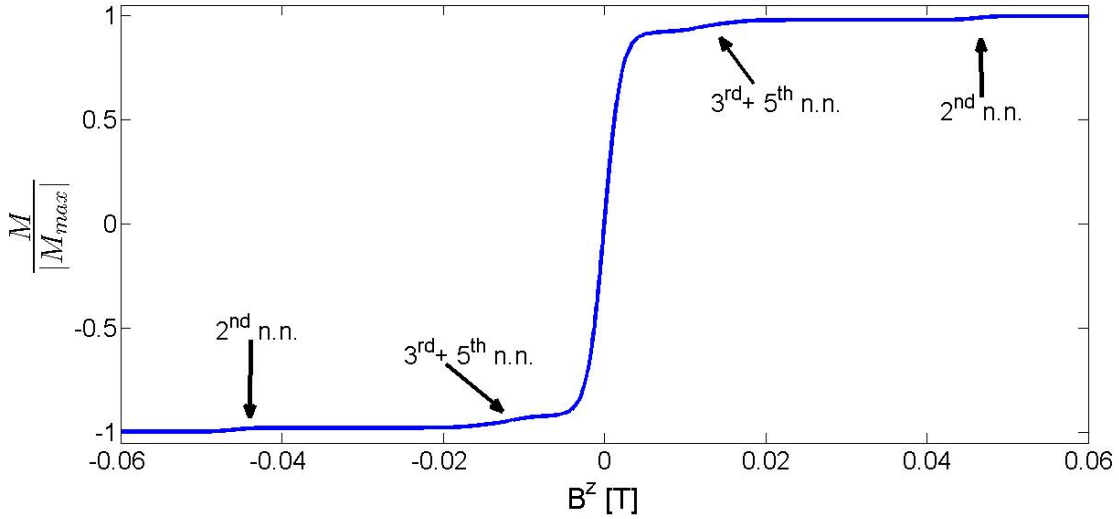


Figure 4.7: Predicted Magnetization for an adiabatic sweep of B^z with $B^x = 0$, $T = 10[mK]$, $x = 0.005$ and a quantum broadening of $1mT$.

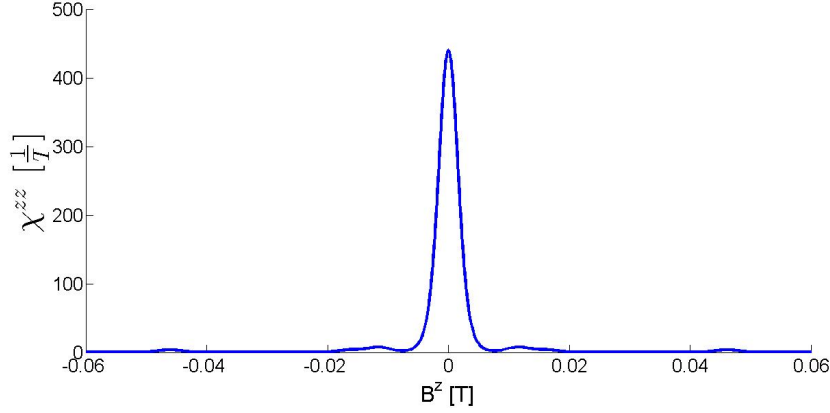


Figure 4.8: *Predicted Susceptibility for an adiabatic sweep of B^z with $B^x = 0$, $T = 10[mK]$, $x = 0.005$ and a quantum broadening of $1mT$.*

Obviously there is no hysteresis since we stay at equilibrium.

A zoom in on the susceptibility plot shows the small peaks more clearly.

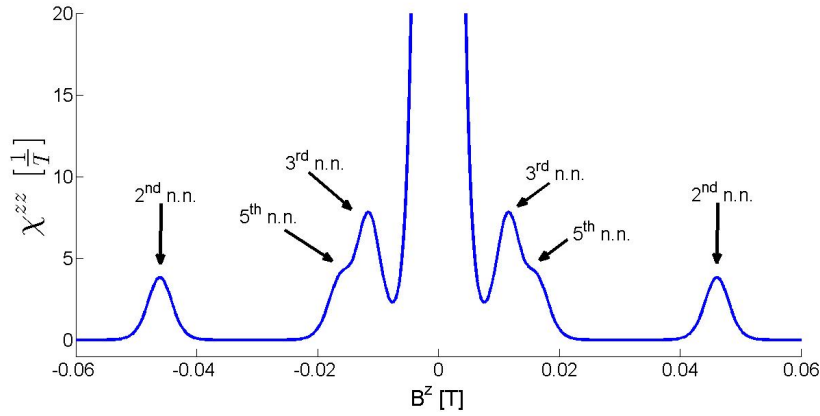


Figure 4.9: *Predicted Susceptibility (zoom in) for an adiabatic sweep of B^z with $B^x = 0$, $T = 10[mK]$, $x = 0.005$ and a quantum broadening of $1mT$.*

The addition of a constant transverse field to the process shifts these resonances as in the previous method (e.g. $B_{eff}^z = 0.044B^x$ for n.n. pairs. see fig. 3.5). We stress again that these predictions assume the application of the transverse field along one of the ("hard")

crystallographic axes.

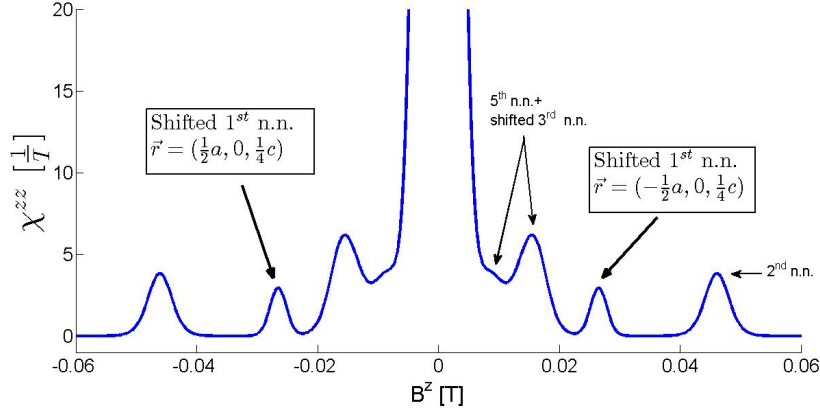


Figure 4.10: *Predicted Susceptibility (zoom in) for an adiabatic sweep of B^z with $B^x = 0.6[T]$, $T = 10[mK]$, $x = 0.005$ and a quantum broadening of $1mT$*

Figure 4.11 shows the difference in paths along the $B^x B^z$ plane between the zero transverse field and the non-zero transverse field predictions for perspective.

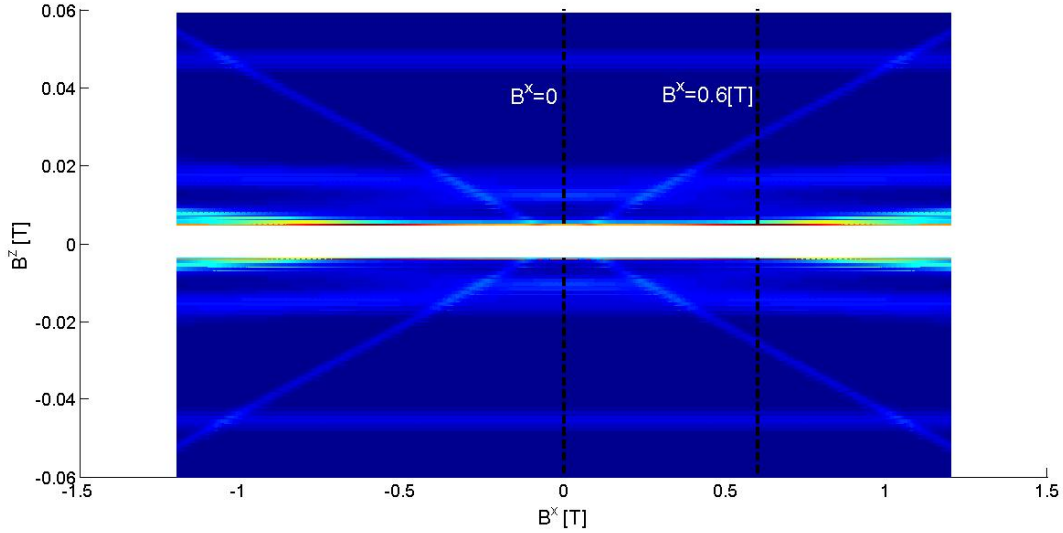


Figure 4.11: *Projection of the susceptibility (χ^{zz}) on the $B^x B^z$ plane (as in fig. 4.5). The two different cross sections presented in figures 4.9 and 4.10 are marked by black dashed lines*

4.2.2 Sweeping the Transverse Field - Equilibrium

Instead of sweeping the longitudinal field, we could keep this field constant, and vary the magnitude of the transverse field. This should shift the resonances for close together pairs with very little effect on the resonances of farther apart pairs (i.e. only ions belonging to close together pairs flip). Thus we can study with ease the transitions corresponding to the crossing of a resonance by specific pairs.

As an example we consider a constant longitudinal field of $B^z = -30[mT]$ and a transverse field swept in the range $-1.2 < B^x < 1.2 [T]$. For perspective we first show the path along the $B^x B^z$ plane for this prediction.

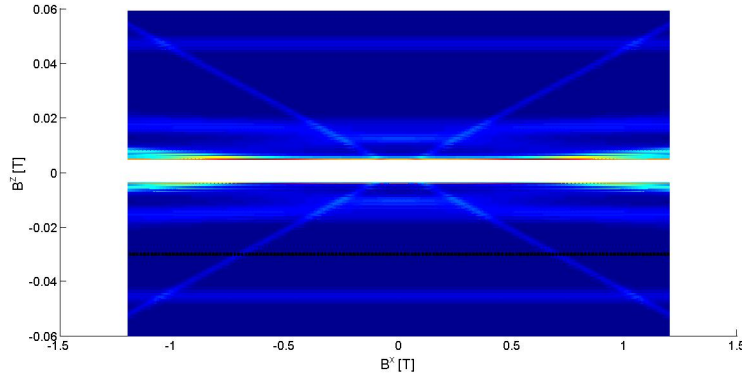


Figure 4.12: *Projection of the susceptibility (χ^{zz}) on the $B^x B^z$ plane (as in fig. 4.5). The cross section presented in figure 4.13 is marked by a black dashed line*

Sweeping the transverse field, should shift the resonances of the n.n. pairs (originating at zero field) until at some point they cross the value of applied field $B^z = -30[mT]$. We stress yet again that our predictions assume the transverse field is applied along one of the ("hard") crystallographic axes and that in any other case modifications can be made easily.

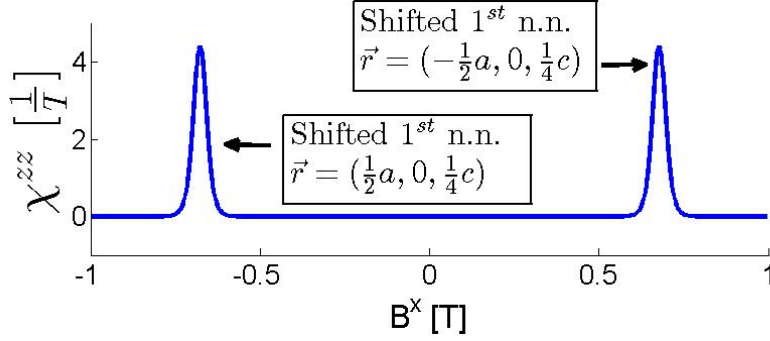


Figure 4.13: Predicted Susceptibility ($\chi^{zz} = \frac{\partial M^z(B^x, B^z)}{\partial B^z}$) for an adiabatic sweep of B^x with $B^z = -30[mT]$, $T = 10[mK]$, $x = 0.005$ and a quantum broadening of $1mT$

Repeating this experiment for various longitudinal field values can be used to verify the linear dependence of the effective longitudinal field on the transverse field.

Another interesting longitudinal field value for this experiment is $B^z = -4[mT]$. Here we suggest measuring both the $\chi^{zz} = \frac{\partial M^z(B^x, B^z)}{\partial B^z}$ and $\chi^{zx} = \frac{\partial M^z(B^x, B^z)}{\partial B^x}$ susceptibilities. Again to give perspective we first show the path along the $B^x B^z$ plane for this prediction.

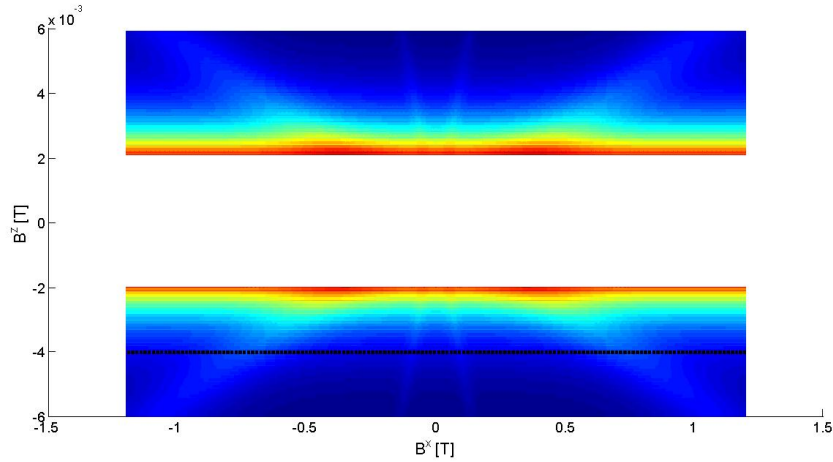


Figure 4.14: Projection of the susceptibility (χ^{zz}) on the $B^x B^z$ plane (a zoom in on fig. 4.5). The cross section presented in figure 4.15 is marked by a black dashed line

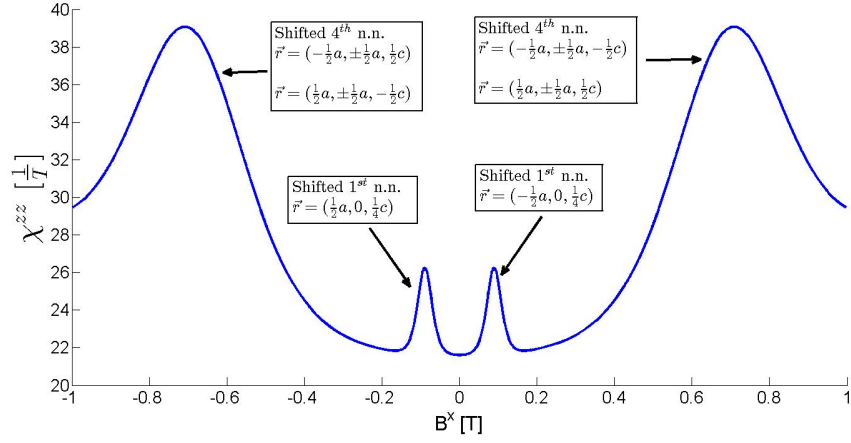


Figure 4.15: Predicted Susceptibility ($\chi^{zz} = \frac{\partial M^z(B^x, B^z)}{\partial B^z}$) for an adiabatic sweep of B^x with $B^z = -4[mT]$, $T = 10[mK]$, $x = 0.005$ and a quantum broadening of $1mT$

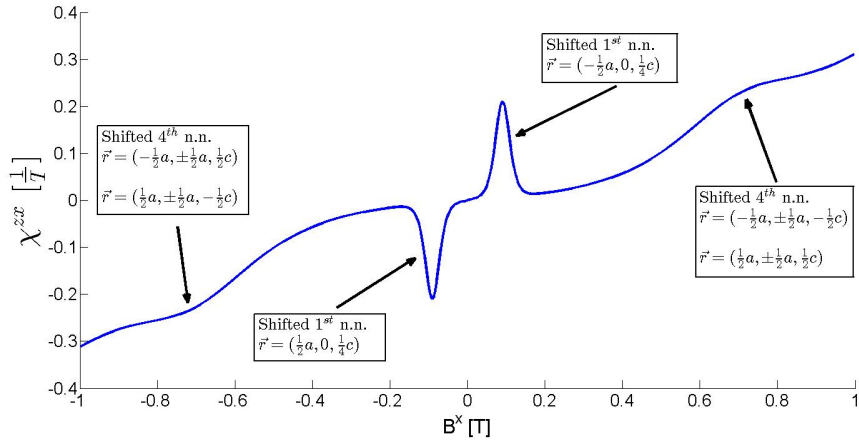


Figure 4.16: Predicted Susceptibility ($\chi^{zx} = \frac{\partial M^z(B^x, B^z)}{\partial B^x}$) for an adiabatic sweep of B^x with $B^z = -4[mT]$, $T = 10[mK]$, $x = 0.005$ and a quantum broadening of $1mT$.

$J^z(B^x)$ (of a single spin) was taken into account (see appendix E.2 for details)

where for χ^{zx} we considered the dependency $J^z(B^x)$ (see appendix E.2) for a more accurate prediction.

Figures 4.15 and 4.16 show both the shifted resonances of the n.n. and 4th n.n. pairs

(both are FM and originating from zero field). Since the effective longitudinal field of the 4th n.n. pairs changes more slowly with B^x than that of the n.n. pairs, they appear at greater B^x values and are more stretched.

The χ^{zz} susceptibility seems to produce clearer results for the peaks of 4th n.n. pairs. However since the longitudinal field value ($B^z = -4[mT]$) puts us within the big magnetization step (see fig. 4.3a), where each fluctuation in B^z produces a significant change in magnetization, the measurement of χ^{zz} should be quite noisy. It might therefore be easier to witness the contribution to susceptibility of the 4th n.n. pairs by the shoulders in the χ^{zx} susceptibility.

We note that this variation of the experiment can also be performed dynamically, i.e. with a sweep rate fast enough so that the system does not equilibrate during the process, much like in the first variation (section 4.1).

4.3 Advantages and Disadvantages of the Three Variations

The dynamical experiment variation under a constant transverse field can prove the ansatz employed by Giraud [15] which explains the small peaks at half integer n as co-tunnelling peaks. Furthermore it enables analysis of the relative contribution of each pair to the co-tunnelling peak (e.g. how big is the contribution of the 1st n.n. pairs which is expected to be much more significant than other pairs). Another advantage of the dynamical variation is the ability to use the effective (random) field as a tool for the study of the dynamics of co-tunnelling.

The main advantage of the two equilibrium variations compared to the dynamic variation, is that they are not as sensitive to experimental parameters. For example the exact sweep rate is not crucial as long as it is sufficiently slow. More importantly, the measurement

resolution can be comparable to that used in the original experiments by Giraud (in the constant transverse field variation) or even lower (in the constant longitudinal field variation). In the equilibrium variation with *constant transverse* field for example this is because there are less peaks in susceptibility (corresponding to unshifted peaks) that can hide the shifted peaks. Of course in the equilibrium variation with *constant longitudinal* field, there are no unshifted peaks at all, so that the shifted peaks should stand out.

We note that the *constant transverse* field version has the advantage of showing the shifted peaks in perspective to unshifted peaks as opposed to the *constant longitudinal* field version.

Another advantage of the equilibrium versions is that we are not restricted to a small temperature to sweep rate ($\frac{T}{\nu}$) ratio. This was required in the dynamic method to keep from having temperature assisted relaxation even away from resonance (i.e. in the previous method we could not allow the system enough time to equilibrate).

This last statement also leads to another advantage of the equilibrium versions. Here the change in magnetization of crossing a shifted resonance (peak area) can be easily calculated from equilibrium considerations, whereas in the dynamic method we could only try to predict it by considering the dynamical process due to both quantum ($T = 0$) transitions (see appendix F) and thermally assisted transitions (as noted in section 2.5.2).

Chapter 5

Summary

In this work we have numerically validated and extended the analysis of an effective random longitudinal magnetic field in disordered anisotropic dipolar magnets under an applied transverse field, beyond second order perturbation regime. By diagonalizing a full 2 Ho ions Hamiltonian for various pairs in the $\text{LiHo}_x\text{Y}_{1-x}\text{F}_4$ compound (section 3.2), we have found the random field for transverse fields of up to around $1.2T$ and shown the increase in random field to be linear for this range (Fig. 3.5). We have also suggested three experimental variations for a possible direct measurement of the random field using co-tunnelling experiments on a $\text{LiHo}_x\text{Y}_{1-x}\text{F}_4$ compound and made predictions for the results (chapter 4). The first method is by applying a constant transverse field to the sample and dynamically sweeping a longitudinal field. This method should produce susceptibility peaks similar to the experiments by Giraud et al. [15, 22] plus some added shifted peaks of nearby (n.n.) pairs due to the random field (Figs. 4.2 and E.1). The second method is to replace the dynamical sweep of the longitudinal field by an adiabatic one (still applying a constant transverse field) so that the system is always at a momentary equilibrium. This should produce fewer peaks, showing the effect of the random field (shifted peaks) more clearly (Fig. 4.10). The third method is to apply a constant longitudinal field and sweep the transverse field adiabatically. This

should produce only the shifted peaks so that even the weaker random fields experienced by 3rd and 4th n.n. pairs would not be obscured (Figs. 4.13, 4.15 and 4.16).

Suggestions for further analysis of this model and realization include for example understanding the characterization of the states beyond transverse fields of $1.4T$. This could lead to understanding of the mechanism responsible for the phase transition to a Paramagnet in dilute anisotropic dipolar magnets. Another possible extension is to try to apply a similar analysis to single molecule magnets such as Fe_8 which posses properties to those of dilute anisotropic dipolar magnets.

Appendix A

Extended Discussion of Single Ion States

A.1 Ion Positions in the LiHoF₄ Unit Cell

Positions of Ho ions in the unit cell:

$$(0, 0, 0) \quad \left(\frac{1}{2}a, 0, \frac{1}{4}c\right) \quad \left(\frac{1}{2}a, \frac{1}{2}a, \frac{1}{2}c\right) \quad \left(0, \frac{1}{2}a, \frac{3}{4}c\right) \quad (\text{A.1.1})$$

Positions of Li ions in the unit cell:

$$\left(\frac{1}{2}a, \frac{1}{2}a, 0\right) \quad \left(0, \frac{1}{2}a, \frac{1}{4}c\right) \quad \left(0, 0, \frac{1}{2}c\right) \quad \left(\frac{1}{2}a, 0, \frac{3}{4}c\right) \quad (\text{A.1.2})$$

Positions of F ions relative to the nearest Ho ion (relative distance $0.2244nm$)[23]:

$$(x_0, y_0, z_0) \quad (-x_0, -y_0, z_0) \quad (x_0, -y_0, -z_0) \quad (-x_0, y_0, -z_0) \quad (\text{A.1.3})$$

where $x_0 = (t - 1/2)a$; $y_0 = (1/2 - p)a$; $z_0 = -qc$

and $p = 0.2817$; $t = 0.1645$; $q = 0.0813$.

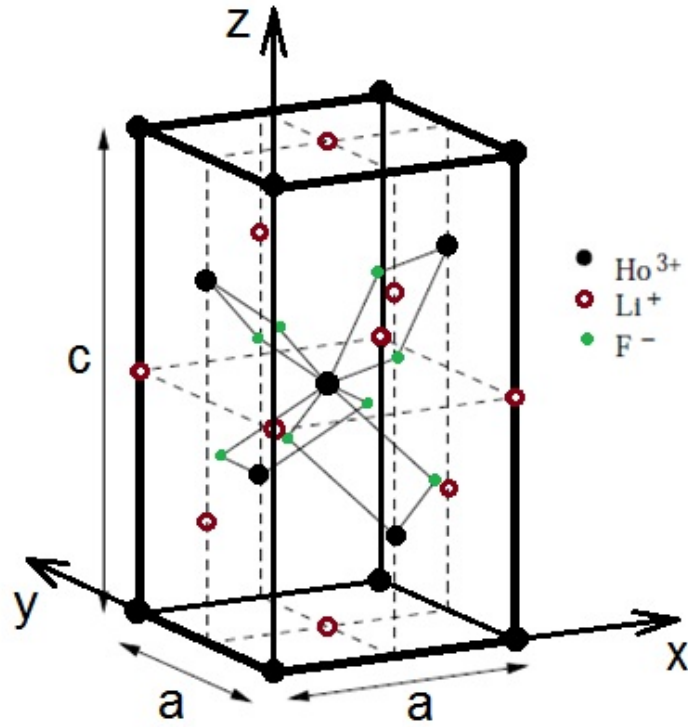


Figure A.1: The unit cell for LiHoF_4 . $a = 5.175\text{\AA}$, $c = 10.75\text{\AA}$. Illustration taken from Gingras and Henelius [10]

Positions of the 5 nearest lattice neighbors to any Ho ion and some properties:

#	n.n.	Dist	X	Y	Z	FM/AFM	Prob	$\Delta E_{FM \rightarrow AFM}$	$B_{FM \rightarrow AFM}^z$	V^{xz}	V^{xx}
1	1 st	3.7E-10	$-\frac{1}{2}$	0	$\frac{1}{4}$	FM	0.5	-0.63		0.01405	-0.00415
2	1 st	3.7E-10	0	$-\frac{1}{2}$	$-\frac{1}{4}$	FM	0.5	-0.63		0	0.00937
3	1 st	3.7E-10	$\frac{1}{2}$	0	$\frac{1}{4}$	FM	0.5	-0.63		-0.01405	-0.00415
4	1 st	3.7E-10	0	$\frac{1}{2}$	$-\frac{1}{4}$	FM	0.5	-0.63		0	0.00937
5	2 nd	5.2E-10	-1	0	0	Anti	0.49	0.43	0.046	0	-0.00702
6	2 nd	5.2E-10	0	-1	0	Anti	0.49	0.43	0.046	0	0.00351
7	2 nd	5.2E-10	0	1	0	Anti	0.49	0.43	0.046	0	0.00351
8	2 nd	5.2E-10	1	0	0	Anti	0.49	0.43	0.046	0	-0.00702
9	3 rd	6.4E-10	$-\frac{1}{2}$	-1	$\frac{1}{4}$	Anti	0.48	0.11	0.012	0.00096	0.00095
10	3 rd	6.4E-10	-1	$-\frac{1}{2}$	$-\frac{1}{4}$	Anti	0.48	0.11	0.012	-0.00192	-0.00183
11	3 rd	6.4E-10	-1	$\frac{1}{2}$	$-\frac{1}{4}$	Anti	0.48	0.11	0.012	-0.00192	-0.00183
12	3 rd	6.4E-10	$-\frac{1}{2}$	1	$\frac{1}{4}$	Anti	0.48	0.11	0.012	0.00096	0.00095
13	3 rd	6.4E-10	$\frac{1}{2}$	-1	$\frac{1}{4}$	Anti	0.48	0.11	0.012	-0.00096	0.00095
14	3 rd	6.4E-10	$\frac{1}{2}$	1	$\frac{1}{4}$	Anti	0.48	0.11	0.012	-0.00096	0.00095
15	3 rd	6.4E-10	1	$-\frac{1}{2}$	$-\frac{1}{4}$	Anti	0.48	0.11	0.012	0.00192	-0.00183
16	3 rd	6.4E-10	1	$\frac{1}{2}$	$-\frac{1}{4}$	Anti	0.48	0.11	0.012	0.00192	-0.00183
17	4 th	6.5E-10	$-\frac{1}{2}$	$-\frac{1}{2}$	$-\frac{1}{2}$	FM	0.46	-0.23		-0.00175	0.00093
18	4 th	6.5E-10	$-\frac{1}{2}$	$-\frac{1}{2}$	$\frac{1}{2}$	FM	0.46	-0.23		0.00175	0.00093
19	4 th	6.5E-10	$-\frac{1}{2}$	$\frac{1}{2}$	$-\frac{1}{2}$	FM	0.46	-0.23		-0.00175	0.00093
20	4 th	6.5E-10	$-\frac{1}{2}$	$\frac{1}{2}$	$\frac{1}{2}$	FM	0.46	-0.23		0.00175	0.00093
21	4 th	6.5E-10	$\frac{1}{2}$	$-\frac{1}{2}$	$-\frac{1}{2}$	FM	0.46	-0.23		0.00175	0.00093
22	4 th	6.5E-10	$\frac{1}{2}$	$-\frac{1}{2}$	$\frac{1}{2}$	FM	0.46	-0.23		-0.00175	0.00093
23	4 th	6.5E-10	$\frac{1}{2}$	$\frac{1}{2}$	$-\frac{1}{2}$	FM	0.46	-0.23		0.00175	0.00093
24	4 th	6.5E-10	$\frac{1}{2}$	$\frac{1}{2}$	$\frac{1}{2}$	FM	0.46	-0.23		-0.00175	0.00093
25	5 th	7.3E-10	-1	-1	0	Anti	0.44	0.15	0.016	0	-0.00062
26	5 th	7.3E-10	-1	1	0	Anti	0.44	0.15	0.016	0	-0.00062
27	5 th	7.3E-10	1	-1	0	Anti	0.44	0.15	0.016	0	-0.00062
28	5 th	7.3E-10	1	1	0	Anti	0.44	0.15	0.016	0	-0.00062

- This table assumes a Ho ion at the origin and lists some properties of its neighboring lattice positions.
- '#’ is a serial number (for keeping track).
- 'n.n.' tells which lattice neighbor this is to the ion at the origin.
- 'Dist' stands for the distance between positions in nanometer.
- X, Y and Z are the separation in each axis. X and Y are in units of $a = 5.175\text{\AA}$ and Z is in units of $c = 10.75\text{\AA}$.
- FM/AFM tells whether an ion placed in this position would interact FerroMagnetically or AntiFerroMagnetically with the ion at the origin.
- 'Prob' stands for the probability that this lattice position will be populated without any closer positions being populated. In other words, what is the probability that the closest other ion to the origin would be in this lattice position.
- $\Delta E_{FM \rightarrow AFM}$ is the energy difference between the lowest 'aligned-ions' state and the lowest 'anti-aligned-ions' state in Kelvin (two ion picture).
- $B_{FM \rightarrow AFM}^z$ is the longitudinal field at which the lowest 'aligned-ions' state and the lowest 'anti-aligned-ions' state cross in Tesla (at zero transverse field; two ion picture; only listed for AFM neighbors).
- V^{xz} is the coefficient of the appropriate Off Diagonal Dipolar interaction (if you multiply this by the J^z of one ion and J^x of the second ion you can get the strength of the corresponding dipolar interaction).
- V^{xx} is the same coefficient only for the appropriate diagonal interaction.

Many lattice distance groups (i.e. 1st n.n. , 2nd n.n. and so on) have two different orientations. One orientation in which the lattice positions have an X component greater in magnitude than the Y component and another orientation for which this is reversed (Y greater than X). We label these 'first' and 'second' orientations respectively. For our purposes, the main difference in these orientation is the magnitude of V^{xz} which determines the magnitude of the effective fields derived in section 3.2 and appendix D. In these terms, the 'first' orientation always leads to greater effective fields than the 'second'. In table A.1 positions #1 and #3 correspond to the 'first' orientations of the 1st n.n. pairs while #2 and #4 correspond to the 'second' orientation. For the 3rd n.n. pairs, positions #10, #11, #15 and #16 correspond to the 'first' orientation while #9, #12, #13 and #14 correspond to the 'second' orientation.

A.2 Ho Free-Ion States

In this section, the reasons for assuming total angular momentum $J = 8$ for free Ho ions, are discussed.

Neutral Ho atoms have the configuration $[Xe]4f^{11}6s^2$ as their ground level. In the $LiHo_xY_{1-x}F_4$ crystal where the Ho ions are trivalent (Ho^{+3}), each Ho ion has 10 electrons in the unfilled $4f$ shell ($[Xe]4f^{10}$). The smallness of the intra-ionic exchange interaction between the free electrons of a single Ho ion, compared to their "direct" interaction, leads to Russell-Saunders (LS) coupling, i.e. characterization of the eigenstates of the Free Ion in terms of orbital angular momentum L and spin S . Rare earth ions and specifically Ho also show strong spin orbit coupling which leads to a preference of further characterization of the states according to total angular momentum J (instead of the spin and orbit projections M_S, M_L). The ground state for this configuration can be found using Hund's rules [24, 25, 26]:

1. The value of the spin S must be maximum (maximum number of parallel spins). For trivalent Ho with 10 free electrons this means 7 electrons "up" and 3 "down" resulting in $S = 7 \cdot \frac{1}{2} - 3 \cdot \frac{1}{2} = 2$.
2. The value of the orbital angular momentum L must be also maximum, taking into account the restrictions imposed by the first rule. $L = 3 + 2 + 1 + 0 + (-1) + (-2) + (-3) + 3 + 2 + 1 = 6$
3. The value of the total angular momentum J is maximum $J = L + S$ as the partially filled $4f$ shell is more than half full. $J = 6 + 2 = 8$.

These properties of the Free Ion ground state can be expressed concisely using the term symbol 5I_8 .

A.3 Crystal Field

In this section, the assumptions leading to the Crystal Field used in this work are discussed, and the details relevant to the chosen realization are specifically noted. At the end of this section, the numerically calculated eigenstates and eigenvalues of this Crystal Field are listed.

For most compounds containing rare earth ions, and specifically for $LiHoF_4$, the Crystal Field Hamiltonian term, which is due to the electrostatic potential (or more accurately due to the superposition model of crystal fields [27]), can be taken as a perturbation compared to the spin-orbit couplings [26]. This is in contrast to the iron group ions which are smaller and therefore have larger Crystal Fields (A common misconception is that the Crystal Field contribution in rare-earths is weaker due to shielding of outer filled shells [28]). This Crystal Field partially breaks the 17-fold degeneracy ($J^z = -8, -7, \dots, 7, 8$) of the Free Ion

states and translates to a large uniaxial magnetic anisotropy along the z axis.

The point charge approximation is used here to find the electrostatic potential. This approximation does not take into account small effects due to the spatial distribution of electrons belonging to adjacent ions, but rather places all charges at the position of the nuclei of these adjacent ions. It also neglects effects such as screening of the magnetic electrons by the outer electron shells of the magnetic ion and spatial overlap of the wave functions of adjacent ions [29, 14].

Under this approximation the potential function is given by the electrostatic potential $V(x, y, z)$ generated by the surrounding point charges at a position (x, y, z) near the magnetic ion in question.

$$V(x, y, z) = \sum_j \frac{q_j}{|\vec{R}_j - \vec{r}|} \quad (\text{A.3.1})$$

where q_j is the charge of the j^{th} ion a distance R_j from the origin. As in most cases, the only significant contribution to the potential is generated by electrons in unfilled shells, as electrons in filled shells only contribute at high order perturbation (ions in an S subshell also contribute only in high order perturbation and can be neglected here) [29].

The straight forward method of performing a Taylor expansion in V in cartesian coordinates is too lengthy in the case of LiHoF_4 . A more convenient method is by defining the potential in terms of tesseral harmonics (which are related to spherical harmonics) [13, 29].

$$V = \sum_{n=0}^{\infty} r^n \sum_{l=0}^n (A_n^l C_n^l + B_n^l S_n^l) \quad (\text{A.3.2})$$

where C_n^l and S_n^l are the tesseral harmonics and A_n^l and B_n^l are constants for a given crystal.

The relevant tesseral harmonics can be deduced from symmetry arguments, and then reformulated in terms of cartesian coordinates. As mentioned in section 2.2, the LiHoF_4 crystal possess an S_4 point symmetry and the potential function V must be invariant under the operations of this point group. Prather [13] gives a thorough account of the tesseral harmonics relevant to various symmetries and specifically for the S_4 symmetry. Not all of the tesseral harmonics given by Prather are used as some of them only couple to or between excited free-ion states which is not relevant even at room temperature (This is why the tesseral harmonics C_{nl} and S_{nl} of index n odd or greater than 6, are not taken into account). Also the coefficient to a single (though not any) tesseral harmonic can be chosen to be zero through the right choice of axes (rotation about the z axis).

Following is a list of the tesseral harmonics relevant to our study and their formulation in cartesian

coordinates:

$$C_2^0 = \frac{\sqrt{10}}{4\sqrt{2\pi}} \frac{2z^2 - x^2 - y^2}{r^2} \quad (\text{A.3.3a})$$

$$C_4^0 = \frac{3\sqrt{2}}{16\sqrt{2\pi}} \frac{8z^4 + 3x^4 + 3y^4 - 24x^2z^2 - 24y^2z^2 + 6x^2y^2}{r^4} \quad (\text{A.3.3b})$$

$$C_4^4 = \frac{3\sqrt{35}}{16\sqrt{\pi}} \frac{x^4 - 6x^2y^2 + y^4}{r^4} \quad (\text{A.3.3c})$$

$$C_6^0 = \frac{\sqrt{26}}{32\sqrt{2\pi}} \frac{16z^6 - 120(x^2 + y^2)z^4 + 90(x^2 + y^2)^2z^2 - 5(x^2 + y^2)^3}{r^4} \quad (\text{A.3.3d})$$

$$C_6^4 = \frac{3\sqrt{91}}{32\sqrt{\pi}} \frac{(10z^2 - x^2 - y^2)(x^4 - 6x^2y^2 + y^4)}{r^6} \quad (\text{A.3.3e})$$

$$S_6^4 = \frac{3\sqrt{91}}{32\sqrt{\pi}} \frac{(10z^2 - x^2 - y^2)(4x^3y - 4xy^3)}{r^6} \quad (\text{A.3.3f})$$

The Crystal Field Hamiltonian term itself is given by :

$$H_{CF} = -|e| \sum_i V(x_i, y_i, z_i) \quad (\text{A.3.4})$$

The method of Steven' "Operator Equivalents" [26] is employed to evaluate the Crystal Field matrix in the free-ion states basis. This amounts to replacing x, y, z by J_x, J_Y, J_z respectively allowing for the non-commutation of J_x, J_Y, J_z . To do this, for every product of J_x, J_Y, J_z , all the different commutations are added and then divided by the number of commutations. This gives an operator which has the same transformation properties under rotations as the potential. Thus according to group theory arguments, the resulting operator is proportional to the original operator up to a numerical factor.

The operator equivalents corresponding to the tesseral harmonics listed previously are:

$$O_2^0 = 3J_z^2 - J(J+1) \quad (\text{A.3.5a})$$

$$O_4^0 = 35J_z^4 - 30J(J+1)J_z^2 + 25J_z^2 - 6J(J+1) + 3J^2(J+1)^2 \quad (\text{A.3.5b})$$

$$O_4^4(C) = J_+^4 + J_-^4 \quad (\text{A.3.5c})$$

$$\begin{aligned} O_6^0 = & 231J_z^6 - 315J(J+1)J_z^4 + 735J_z^4 + 105J^2(J+1)^2J_z^2 - \\ & - 525J(J+1)J_z^2 + 294Jz^2 - 5J^3(J+1)^3 + \\ & + 40J^2(J+1)^2 - 60J(J+1) \end{aligned} \quad (\text{A.3.5d})$$

$$\begin{aligned} O_6^4(C) = & (j_+^4 + j_-^4)(11Jz^2 - J(J+1) - 38) + \\ & + (11Jz^2 - J(J+1) - 38)(j_+^4 + j_-^4) \end{aligned} \quad (\text{A.3.5e})$$

$$O_6^4(S) = (j_+^4 - j_-^4)(11Jz^2 - J(J+1) - 38) - (11Jz^2 - J(J+1) - 38)(j_+^4 + j_-^4) \quad (\text{A.3.5f})$$

Stevens [26] suggests a method for calculating the coefficients relating his operators to the original ones, but this calculation is arduous and problematic and in practice the coefficient of each Stevens' operator equivalent is determined by fitting H_{CF} to experimental data. These phenomenological constants are called the Crystal Field Parameters (CFP).

Finally the Crystal Field used in this work formulated in the operator equivalents is:

$$H_{CF} = B_2^0 O_2^0 + B_4^0 O_4^0 + B_6^0 O_6^0 + B_4^4(C) O_4^4(C) + B_6^4(C) O_6^4(C) + B_6^4(S) O_6^4(S) \quad (\text{A.3.6})$$

where the B_n^l are the Crystal Field Parameters with values proposed by Rønnow et al. and listed clearly by Chakraborty [14].

$$B_2^0 = -0.696K \quad (\text{A.3.7a})$$

$$B_4^0 = 4.06 \cdot 10^{-3}K \quad (\text{A.3.7b})$$

$$B_6^0 = 4.64 \cdot 10^{-6}K \quad (\text{A.3.7c})$$

$$B_4^4(C) = 0.0418K \quad (\text{A.3.7d})$$

$$B_6^4(C) = 8.12 \cdot 10^{-4}K \quad (\text{A.3.7e})$$

$$B_6^4(S) = 1.137 \cdot 10^{-4}K \quad (\text{A.3.7f})$$

These values were obtained through fitting the results of RPA [Random Phase Approximation] of spin-wave dynamics calculations to observed neutron scattering data, as well as to the two lowest energy levels of the crystal-field spectrum, as observed in spectroscopic measurements. However, there are no estimates of the accuracies to which these parameters are known [14].

Group theory arguments dictate that in S_4 symmetry, the states of a configuration with an even number of electrons transform according to four one-dimensional representations $[\Gamma_{1,2,3,4}]$, two of which are related by time-reversal symmetry. The ground state of the crystal-field Hamiltonian is thus a doublet, belonging to the two related representations mentioned above, giving rise to a non-Kramers degenerate ground state [14].

In fact even simple observation of the Crystal Field Hamiltonian suggests that the only terms breaking the symmetry of rotations about the z axis are the ones containing O_4^4 and O_6^4 which couple free-ion states

with $\Delta l = \pm 4$ making the eigenvectors:

$$V_{\Gamma_3} = \alpha^i |Jz = -7\rangle + \beta^i |Jz = -3\rangle + \gamma^i |Jz = 1\rangle + \delta^i |Jz = 5\rangle \quad (\text{A.3.8a})$$

$$V_{\Gamma_4} = \alpha^i |Jz = 7\rangle + \beta^i |Jz = 3\rangle + \gamma^i |Jz = -1\rangle + \delta^i |Jz = -5\rangle \quad (\text{A.3.8b})$$

$$V_{\Gamma_2} = \alpha^i |Jz = -6\rangle + \beta^i |Jz = -2\rangle + \gamma^i |Jz = 2\rangle + \delta^i |Jz = 6\rangle \quad (\text{A.3.8c})$$

$$V_{\Gamma_1} = \alpha^i |Jz = -8\rangle + \beta^i |Jz = -4\rangle + \gamma^i |Jz = 0\rangle + \delta^i |Jz = 4\rangle + \epsilon^i |Jz = 8\rangle \quad (\text{A.3.8d})$$

with different coefficients α^i through ϵ^i for each state ($i = 1..17$).

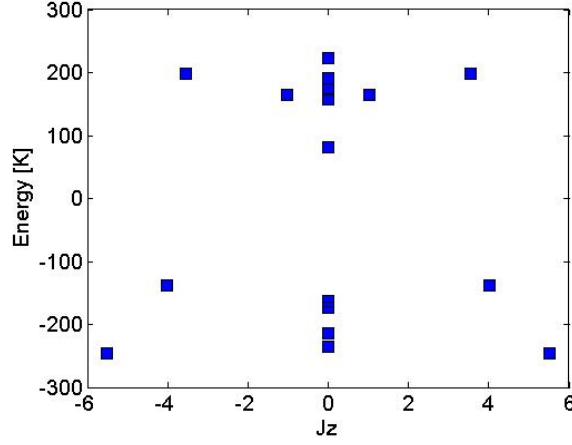


Figure A.2: The energies for the different states as a function of their $\langle J_z \rangle$ expectancy value.

Figure based on similar plot in Giraud et al. [15]

These states and their corresponding energies were also found numerically through a standard Matlab diagonalization routine (see code in appendix G.1).

The eigenstates are:

$$10^{-2} \cdot \begin{pmatrix} -21-77i & 0 & 0 & 0 & 0 & 0 & 0 & 0 & -1-5i & 0 & 0 & 0 & -6-24i & 0 & 0 & -14-54i & 0 & 0 \\ 22+56i & 0 & 0 & 0 & 0 & 0 & 0 & 0 & i & 0 & 0 & 0 & -11-27i & 0 & 0 & -27-69i & 0 & 0 \\ 4 & 0 & 0 & 0 & 0 & 0 & 0 & 0 & -49-3i & 0 & 0 & 0 & -80-4i & 0 & 0 & 34+2i & 0 & 0 \\ -3 & 0 & 0 & 0 & 0 & 0 & 0 & 0 & 87 & 0 & 0 & 0 & -46 & 0 & 0 & 17 & 0 & 0 \\ 0 & -1-3i & 0 & 0 & 0 & 0 & -23-84i & 0 & 0 & 0 & 0 & -12-44i & 0 & 0 & 0 & 0 & 4+16i & 0 \\ 0 & 1+4i & 0 & 0 & 0 & 0 & 15+46i & 0 & 0 & 0 & 0 & -25-76i & 0 & 0 & 0 & 0 & 11+32i & 0 \\ 0 & 60+7i & 0 & 0 & 0 & 0 & -1 & 0 & 0 & 0 & 0 & -29-3i & 0 & 0 & 0 & 0 & -74-8i & 0 \\ 0 & -79 & 0 & 0 & 0 & 0 & 5 & 0 & 0 & 0 & 0 & -24 & 0 & 0 & 0 & 0 & -55 & 0 \\ 0 & 0 & 0 & 0 & 0 & -45-i & -48-2i & 0 & 0 & -38-i & -52-2i & 0 & 0 & 0 & 39+i & 0 & 0 & 0 \\ 0 & 0 & 0 & 0 & 52-5i & 52-5i & 0 & 0 & 0 & -16+i & -48+4i & 0 & 0 & 0 & 44-4i & 0 & 0 & 0 \\ 0 & 0 & 0 & 0 & -20 & 0 & 0 & 0 & 0 & 81+i & 0 & 0 & 0 & 0 & 54+i & 0 & 0 & 0 \\ 0 & 0 & 0 & 0 & 52+6i & -52-6i & 0 & 0 & -16-2i & 47+6i & 0 & 0 & 0 & 0 & 44+5i & 0 & 0 & 0 \\ 0 & 0 & 0 & 0 & -45 & 48 & 0 & 0 & -38 & 52 & 0 & 0 & 0 & 0 & 39 & 0 & 0 & 0 \\ 0 & 0 & 42+39i & 44+42i & 0 & 0 & 0 & 0 & 0 & 0 & 0 & 0 & 30+28i & 0 & 0 & 0 & 0 & -27-25i \\ 0 & 0 & -32-25i & -29-23i & 0 & 0 & 0 & 0 & 0 & 0 & 0 & 0 & 45+35i & 0 & 0 & 0 & 0 & -48-37i \\ 0 & 0 & -41-4i & 36+3i & 0 & 0 & 0 & 0 & 0 & 0 & 0 & 0 & 57+5i & 0 & 0 & 0 & 0 & 60+6i \\ 0 & 0 & 58 & -60 & 0 & 0 & 0 & 0 & 0 & 0 & 0 & 0 & 41 & 0 & 0 & 0 & 0 & 37 \end{pmatrix}$$

and the corresponding energies in Kelvin are:

$$\begin{pmatrix} -246 & -246 & -235 & -214 & -174 & -162 & -137 & -137 & 82 & 158 & 164 & 164 & 174 & 192 & 197 & 197 & 223 \end{pmatrix}$$

A.4 HyperFine Constant

The HyperFine constant A_J can be found through fitting to the results of the experiments discussed on section 2.5.2. This is done by comparing the positions of the crossings, in the field axis, predicted by theory for single ions:

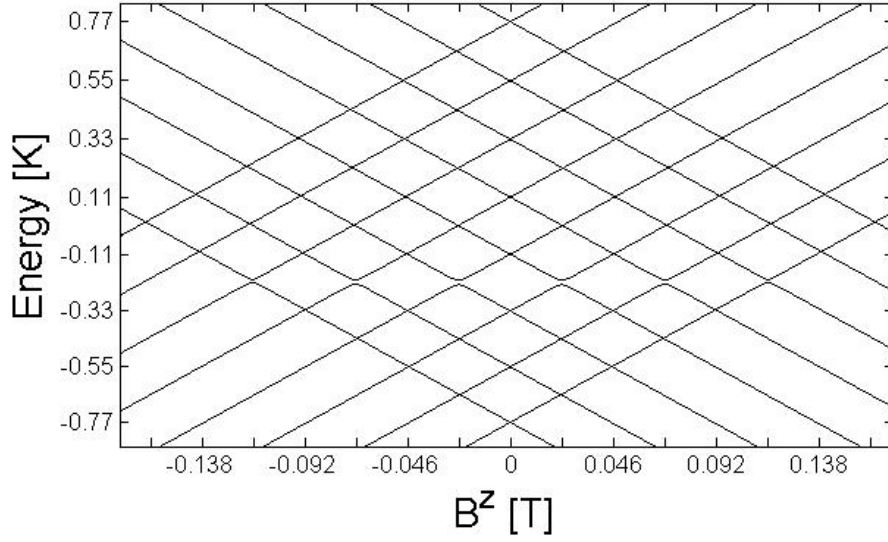


Figure A.3: *Predicted crossings in the single ion picture.*

$$\begin{aligned}
 A_J J^z \cdot n - g_L \mu_B J_{\uparrow}^z B_n^z &= 0 - g_L \mu_B J_{\downarrow}^z B_n^z \\
 \Downarrow \\
 B_n^z &= \frac{A_J J^z \cdot n}{g_L \mu_B (J_{\uparrow}^z - J_{\downarrow}^z)}
 \end{aligned}
 \tag{A.4.1}$$

to the experimental resonance fields (for integer n crossings):

$$B_n^z = n \cdot 23mT \tag{A.4.2}$$

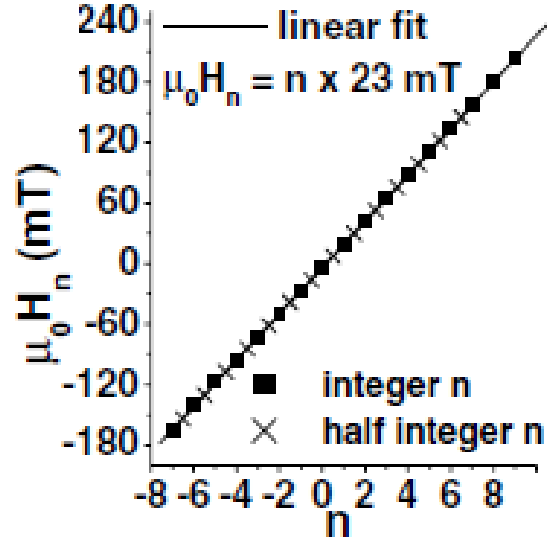


Figure A.4: *Applied field values at resonances. Plot taken from Giraud et al. [15]*

resulting in $A_J = 0.039K$.

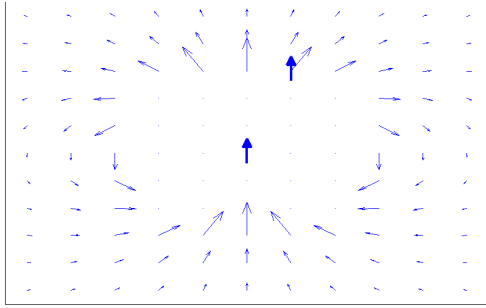
Appendix B

Perturbation Theory - Extended

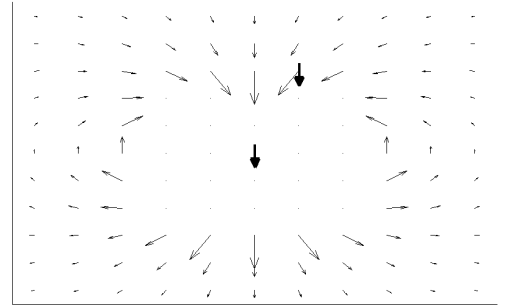
In this appendix, after first portraying an intuitive picture explaining the breaking of symmetry, we present in detail the perturbation expansion discussed in section 3.1. We start by reviewing in full detail the expansion to leading term (2nd order), followed by an extension of greater precision within the same order of expansion. Next an expansion of 3rd order in perturbation theory is derived. Finally the perturbative results are compared with numerical ones.

B.0.1 An Intuitive Picture of Symmetry Breaking

An intuitive perspective of why the combination of a transverse field and the dipolar interaction breaks the symmetry to flips of spins along the z axis can be obtained by considering the following classical picture (see figs. B.1 through B.3 below): We consider two dipoles (bold arrows) both pointing in the same direction along the z axis (blue for both up or black for both down) and lying on the xz plane. For convenience we position one of them at the origin and look at the dipolar magnetic field (thin arrows) experienced by the other.



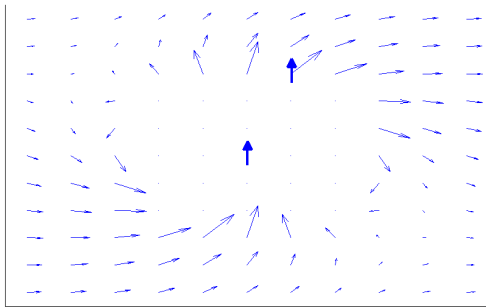
(a) *Two dipoles up*



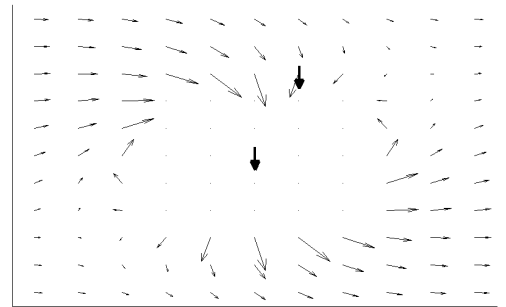
(b) *Two dipoles up*

Figure B.1: *Two dipoles and the field generated by the one at the origin*

We now add an applied transverse magnetic field to the right:



(a) *Two dipoles up*



(b) *Two dipoles down*

Figure B.2: *The same as above (fig. B.1) plus an applied transverse field to the right*

Finally we compare the two cases:

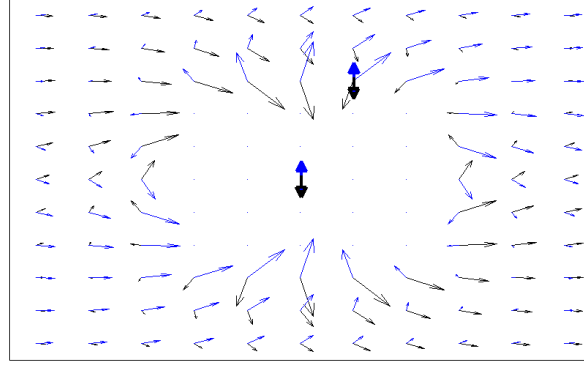


Figure B.3: Comparison between the two dipoles up case (blue) and two dipoles down case (black)

When both magnetic moments are up the transverse part of the dipolar field adds to the applied field, while when both are down they subtract. Thus the total transverse field (experienced by the second dipole away from the origin) is greater when both dipoles are up, allowing (in the quantum case) greater fluctuations and thus a lower energy for that state.

B.0.2 2nd Order - First Approximation

We now give a rigorous review of the expansion of the energy levels in second order degenerate perturbation theory which was originally derived in [7] up to the leading term. However here the derivation is carried with the specifics of the $\text{LiHo}_x\text{Y}_{1-x}\text{F}_4$ crystal in mind. The unperturbed Hamiltonian is:

$$H_0 = H_{CF} + A_J \sum_i I_i^z \cdot J_i^z + \sum_{i \neq j} V_{ij}^{zz} J_i^z J_j^z \quad (\text{B.0.1})$$

As mentioned in section 3.1, the states for which we would like to find the splitting are 'Global-Ising states' for which all the ions are in one of the (single ion) electro-nuclear Ising states (e.g. $|\uparrow - \frac{5}{2}\rangle$). Specifically the splitting will occur between any two such states, which are degenerate and related by $J_k^z \rightarrow -J_k^z$ and $I_k^z \rightarrow -I_k^z$ symmetry. Considering the scaling ("droplet") picture [30, 31], the ground states correspond to each of the Ho ions being in one of the Ising states $|\uparrow - \frac{7}{2}\rangle$ or $|\downarrow \frac{7}{2}\rangle$ in such a way as to minimize the longitudinal dipolar term and are only twofold degenerate with the two states related by the above symmetry. Thus this analysis can be applied to the ground states as a representing example (as was performed in the original derivation [7]).

Following Schiff [32], second order expansion of the eigenstates and eigenvalues in the Schrödinger equation gives the following equations in determinant form:

$$\begin{vmatrix} \sum_{n \notin M} \frac{|\langle m|H'|n\rangle|^2}{E_m - E_n} - W_2 & \sum_{n \notin M} \frac{\langle m|H'|n\rangle \langle n|H'|l\rangle}{E_m - E_n} \\ \sum_{n \notin M} \frac{\langle l|H'|n\rangle \langle n|H'|m\rangle}{E_m - E_n} & \sum_{n \notin M} \frac{|\langle l|H'|n\rangle|^2}{E_m - E_n} - W_2 \end{vmatrix} = 0 \quad (\text{B.0.2})$$

where W_2 is the corrected energy level and H' is the perturbation:

$$H' = \sum_{\alpha, \beta \neq zz} \sum_{j \neq i} V_{ij}^{\alpha\beta} J_i^\alpha J_j^\beta - g_L \mu_B B^x \sum_i J_i^x + \frac{A_J}{2} \sum_i (I_i^+ \cdot J_i^- + I_i^- \cdot J_i^+) \quad (\text{B.0.3})$$

assuming an applied transverse field along the x axis.

The notation conventions used in eq. B.0.2 and throughout this appendix are as follows:

- m and l are the unperturbed states to be expanded and constitute the subspace M . They are any two degenerate ($E_m = E_l$) 'Global-Ising states' for which all the ions are in one of the (single ion) electro-nuclear Ising states (e.g. $|\uparrow - \frac{5}{2}\rangle$) and related by $J_k^z \rightarrow -J_k^z$ and $I_k^z \rightarrow -I_k^z$ symmetry. The subspace \tilde{M} contains all of the 'Global-Ising states' (as opposed to just 2 of them in M)
- n (or n') is any of the other states in the entire Hilbert space Λ .
- the p, q, r, s states (see below) are states identical to either m or l with the exception of one or two spins in the higher (single ion) electronic levels (e.g. Γ_2). These states constitute the subspace P .

Solving gives:

$$\begin{aligned} W_2 &= \frac{1}{2} \sum_{n \notin M} \frac{|\langle m|H'|n\rangle|^2 + |\langle l|H'|n\rangle|^2}{E_m - E_n} \pm \\ &\pm \frac{1}{2} \left[\left(\sum_{n \notin M} \frac{|\langle m|H'|n\rangle|^2}{E_m - E_n} - \sum_{n' \notin M} \frac{|\langle l|H'|n'\rangle|^2}{E_m - E_{n'}} \right)^2 + \right. \\ &\quad \left. + 4 \sum_{n \notin M} \sum_{n' \notin M} \frac{\langle m|H'|n\rangle \langle n|H'|l\rangle \langle l|H'|n'\rangle \langle n'|H'|m\rangle}{(E_m - E_n)(E_m - E_{n'})} \right]^{\frac{1}{2}} \\ &= \text{II} \pm \frac{1}{2} \sqrt{(\text{III})^2 + \text{IIII}} \end{aligned} \quad (\text{B.0.4})$$

Terms II give the same correction to both m and l states and do not remove the degeneracy. Terms III give the corrections due to coupling between a state in M and a state outside M , and are the main focus here. Terms IIIV require coupling between the m and l states which does not exist at second order (among other reasons due to the HF structure) and thus zero out (in the original derivation this was due to the ground states being $|J^z = \pm J\rangle$ with $J > \frac{1}{2}$).

Furthermore at this order of expansion, the only terms that do not fall off, employ the n states which the perturbation directly couples to the unperturbed M states. This means n states identical to the M states but for one or two Ho ions excited to a higher electronic (single ion) state (e.g. Γ_2). We label these states p and q , and name the subspace they constitute P .

As a first approximation we consider only the minimally excited P states with a single Ho ion excited to the Γ_2 level, which are significantly closer in energy to the M states (Ω_0) than the other options ($2\Omega_0$ and above). In fact the states P of two excited ions coupled to the M states through dipolar terms such as V^{xx} , fall off due to symmetry (see below) so that the next relevant excited P state is roughly $3\Omega_0$ away from the M states. As a first approximation we consider only the contribution of the Crystal Field term in the Hamiltonian to the energy separation between the relevant levels since the longitudinal dipolar and longitudinal HF interactions give very small contributions in comparison. Later we will include these corrections as well.

Thus considering only the contribution of the 'minimally excited' excited P states, the energy difference between the m and l levels is now:

$$\delta E^{(2)} = \sum_p \frac{\langle m | H' | p \rangle \langle p | H' | m \rangle}{\Omega_0} - \sum_q \frac{\langle l | H' | q \rangle \langle q | H' | l \rangle}{\Omega_0} \quad (\text{B.0.5})$$

The only terms in this expression that do not zero out trivially, are those that have only an even number of J_i^x operators (for any i), and an even (including zero) number of nuclear ladder operator I_i^\pm . Also, terms without an odd number of J_k^z operators cancel each other out (identical terms in the right and left segments of the expression).

The surviving terms are identical for the left and right segments of the above expression up to a minus sign so that we can take only the left segment and multiply by 2. Writing the surviving terms explicitly gives:

$$\delta E^{(2)} = 2 \sum_p \frac{2 \langle m | 2 \sum_{k \neq i} V_{ki}^{zx} J_k^z J_i^x | p \rangle \langle p | \sum_i g_L \mu_B B^x J_i^x | m \rangle}{\Omega_0} \quad (\text{B.0.6})$$

We now invoke the completeness relation to add $|m \rangle \langle m|$ after J_k^z (other terms in $\sum_{n \in \Lambda} |n \rangle \langle n| = \mathbb{I}$ fall off). We can also omit the summation over p , noting that the only contribution comes from p states in which the ions excited to Γ_2 match the ions affected by the J_i^x operators.

$$\delta E^{(2)} = \frac{8 \langle m | \sum_{k \neq i} V_{ki}^{zx} J_k^z | m \rangle \langle m | J_i^x | p \rangle \langle p | \sum_i g_L \mu_B B^x J_i^x | m \rangle}{\Omega_0} \quad (\text{B.0.7})$$

This can now be formulated with single ion states of the relevant ions:

$$\delta E^{(2)} = 8 g_L \mu_B B^x \sum_{k \neq i} \sum_i V_{ki}^{zx} \frac{\langle m_s | J_k^z | m_s \rangle \langle m_s | J_i^x | \Gamma_2 \rangle \langle \Gamma_2 | J_i^x | m_s \rangle}{\Omega_0} \quad (\text{B.0.8})$$

where m_s is the single ion state (e.g. $|\uparrow -I^z\rangle$) as dictated for each ion by the global state m . The quantity $\eta = |\langle \Gamma_2 | J^x | m_s \rangle|^2 = 5.62$ is found numerically using the code in appendix G.1.

$$\delta E^{(2)} = 2g_L\mu_B \sum_k \left(\frac{4\eta}{\Omega_0} \sum_{i \neq k} V_{ki}^{zx} B^x \right) \langle J_k^z \rangle \quad (\text{B.0.9})$$

This energy splitting has the form of a sum of, single ion, longitudinal Zeeman splittings (see eq. 2.5.2)

$$\delta E = 2g_L\mu_B \sum_k B_{k,eff}^z \langle J_k^z \rangle \quad (\text{B.0.10})$$

and we thus deduce effective longitudinal fields

$$B_{k,eff}^z = \frac{4\eta}{\Omega_0} \sum_{i \neq k} V_{ki}^{zx} B^x \quad (\text{B.0.11})$$

It is important to note that, at this level of approximation, the form of the energy splitting is identical for any two '*Global-Ising states*' (M). This allows us to apply the interpretation of a unique effective field to the entire subspace \tilde{M} (as defined at the beginning of this section). A more careful discussion of this fine point can be found in the next section (B.0.3).

As mentioned in section 3.1, the dependence of these effective longitudinal fields on the strength of the dipolar interactions makes them effectively random due to the spatial disorder of the magnetic ions.

A rough estimate is that this analysis is valid as long as corrections of first order to the unperturbed states are small $g_L\mu_B\sqrt{\eta}B^x \ll \Omega_0$ (or roughly $B^x \ll 2.5[T]$). However there are more constraints such as that this analysis is of course not valid near level crossings.

As implicitly mentioned above and explicitly in section 2.1, this derivation assumes large magnetic moments $J > \frac{1}{2}$. In real spin half systems the transverse field could couple the Ising states thereby resulting in completely different physics.

B.0.3 2nd Order - Complete

We now address the two approximations performed in the above expansion, and present a precise derivation of 2nd order expansion without any omissions. This would produce a limit to the validity of the effective field interpretation. It will also induce corrections more significant than the 3rd order contribution to be derived later.

The exact (unperturbed) energy difference between an M state and the relevant excited state should include the contributions of the longitudinal HF and longitudinal dipolar interactions. This turns eq. B.0.9

into:

$$\delta E^{(2)} = 2g_L\mu_B \sum_k \left(\frac{4\eta \sum_{i \neq k} V_{ki}^{zx}}{\Omega_0 + 2V_{ki}^{zz} \langle J_k^z \rangle \langle J_i^z \rangle + A_J \langle J_i^z \rangle \langle I_i^z \rangle} B^x \right) \langle J_k^z \rangle \quad (\text{B.0.12})$$

The contribution of the longitudinal dipolar interactions is small compared to Ω_0 (6% for n.n.) and does not change the qualitative picture at all (we already considered that each pair experiences a different effective field).

The correction due to the longitudinal HF interaction on the other hand can change the qualitative nature of the model. This is relevant either for high enough temperatures comparable to the HF splitting or for dynamical (out of equilibrium) processes, where not only the ground states are populated and we have to consider the splitting of both ground and excited states. In these cases the longitudinal HF interaction leads to some states splitting up to around 30% more than others (each state has a different "effective field"). Thus attributing a unique effective field to the entire subspace of 'Global-Ising states' (\tilde{M}) is only an approximation. Restricting the subspace further (e.g. by considering only the 8 lowest levels) can improve this approximation and its predictions. The original derivation [7] considered only the ground states in which case the effective field model is exact (the contribution of the HF interaction was included in the expression for Ω_0).

Another correction regards neglected terms in the numerator. These terms are related to coupling of the unperturbed states (m or l) to p states with an ion excited to high energy (single ion) electronic states (higher than Γ_2). These terms contribute in the same way as the more dominant terms only with a larger denominator and a different coupling $\eta_u = |\langle u | J^x | m_s \rangle|^2 \neq \eta$ (where $u = 4, 5, \dots$ are the electronic single ion states numbered in ascending order of energy). Thus both the corrections discussed in this section can easily be taken into account by substituting $\frac{\eta}{\Omega_0}$ for $\Theta = \frac{\eta}{(E_3 - E_m)} + \sum_{u=4}^{17} \frac{\eta_u}{E_u - E_m}$ in eq. B.0.9. These added terms turn out to be very significant and contribute a correction of 47% (not taking into account the HF and dipolar corrections above). This significant correction is a feature of the $\text{LiHo}_x\text{Y}_{1-x}\text{F}_4$ realization and did not appear in the original derivation which considered a general anisotropic dipolar magnet model where the transverse field could only couple to an excited electronic state of $\Delta J^z = 1$ (see section 2.1)

B.0.4 3rd Order

Similarly to eq. B.0.4, the equations for the 3rd and 4th order energy corrections can each be divided into three segments, where only the second one (see eq. B.0.13) contributes to the removal of degeneracy.

$$W_{3,4} = \mathbb{I} \pm \frac{1}{2} \sqrt{(\mathbb{III})^2 + \mathbb{IIII}} \quad (\text{B.0.13})$$

This is because the first part equally shifts the energy of both m and l states, and the third part requires a coupling between the m and l states which only happens at much higher orders. The third order contribution to the energy splitting is therefore:

$$\text{III} = \delta E^{(3)} = \sum_{q,p \in P} \frac{\langle m|H'|q \rangle \langle q|H'|p \rangle \langle p|H'|m \rangle}{(E_m - E_q)(E_m - E_p)} - \sum_{r,s \in P} \frac{\langle l|H'|r \rangle \langle r|H'|s \rangle \langle s|H'|l \rangle}{(E_m - E_r)(E_m - E_s)} \quad (\text{B.0.14})$$

where we already considered that only states within the subspace P can contribute at this order of perturbation (the original summation is over $n \notin M$) as discussed in section 3.1.

As in the 2nd order expansion, the only terms in this expression that do not zero out trivially, are those that have only an even number of J_i^x operators (for any i), and an even (including zero) number of nuclear ladder operator I_i^\pm . Also, terms without an odd number of J_k^z operators cancel each other out (identical terms in the right and left segments of the final expression).

Considering the surviving terms only in the left segment ($\langle m|\dots|m \rangle$) of the above expression for brevity, the corresponding numerators have the form:

$$N_1 = \sum_q \sum_p \langle m|2 \sum_{k \neq j} V_{kj}^{zx} J_k^z J_j^x|q \rangle \langle q|2 \sum_{j \neq i} V_{ji}^{xx} J_j^x J_i^x|p \rangle \langle p|(-g_L \mu_B B^x \sum_i J_i^x)|m \rangle \quad (\text{B.0.15})$$

$$N_2 = \sum_q \sum_p \langle m|(-g_L \mu_B B^x J_k^x)|q \rangle \langle q|2 \sum_{k \neq j} V_{kj}^{xx} J_k^x J_j^x|p \rangle \langle p|2 \sum_{j \neq i} \sum_i V_{ij}^{zx} J_i^z J_j^x|m \rangle \quad (\text{B.0.16})$$

with minimal denominators $(E_m - E_q)(E_m - E_p) = \Omega_0^2$ (see clarification below.)

or numerators:

$$N_3 = \sum_q \sum_p \langle m|2 \sum_{k \neq j} V_{kj}^{zx} J_k^z J_j^x|q \rangle \langle q|2(-g_L \mu_B B^x J_i^x)|p \rangle \langle p|\sum_{j \neq i} \sum_i V_{ij}^{xx} J_i^x J_j^x|m \rangle \quad (\text{B.0.17})$$

$$N_4 = \sum_q \sum_p \langle m|(-g_L \mu_B B^x J_i^x)|q \rangle \langle q|4 \sum_{k \neq i,j} V_{kj}^{zx} J_k^z J_j^x|p \rangle \langle p|\sum_{j \neq i} \sum_i V_{ij}^{xx} J_i^x J_j^x|m \rangle \quad (\text{B.0.18})$$

$$N_5 = \sum_q \sum_p \langle m|2V_{ij}^{xx} J_i^x J_j^x|q \rangle \langle q|2 \sum_{k \neq i,j} \sum_{j \neq i} V_{kj}^{zx} J_k^z J_j^x|p \rangle \langle p|(-g_L \mu_B B^x \sum_i J_i^x)|m \rangle \quad (\text{B.0.19})$$

with minimal denominators $(E_m - E_q)(E_m - E_p) = 2\Omega_0^2$ (see clarification below).

As all these terms are linear in B^x and in J_k^z we can expect the entire energy correction to have the same qualitative properties (an ion dependent effective longitudinal field linear in B^x). A thorough quantitative analysis follows for the purpose of comparison with numerical results.

As an approximation we can neglect states q and p with ions excited higher than the (single ion) Γ_2 level. These give smaller terms because of larger denominators

$(E_m - E_q)(E_m - E_p) \geq 3(\Omega_0)^2$. Importantly, these smaller terms are qualitatively the same as the larger which further justifies their omission.

We now direct our attention to $N_{4,5}$, noting the absence of terms with $\langle q | \sum_{k \neq j} V_{kj}^{zx} J_{k=i}^z J_j^x | p \rangle \langle p | \dots J_i^x | m \rangle$ since (in the single ion picture) $\langle \Gamma_2 | J^z | \Gamma_2 \rangle = 0$. This produces a significant difference between these terms and those with $N_{1,2,3}$ allowing us to neglect the former. In $N_{4,5}$, the two dipolar interaction operators (V_{kj}^{zx} and V_{ij}^{xx}) are between some ion j and two other ions ($i \neq k$), while in the $N_{1,2,3}$ this constraint is missing. For the purpose of comparison with the numerical analysis, the $N_{4,5}$ terms are trivially omitted since the model used in the numerics simulates strong Ho dilution by assuming that for each ion, only the nearest other ion has any effect (it's a two ions model).

For completeness we explain why these terms can be neglected using more general arguments. For strong Ho dilution ($x \ll 1$), we can say that the chance of an ion having two other nearest ions at similar distances is very low or in other words that for most ions the next ion after the nearest is significantly farther than the nearest. This makes the $N_{4,5}$ terms generally much smaller than the $N_{1,2,3}$ terms which have components proportional to the dipolar interactions (V_{kj}^{zx} and V_{ij}^{xx}) between the same pair ($i = k$). This is especially true for ion pairs only slightly separated, i.e. for each ion k with another close enough ion j (say k and j are at most 4th nearest lattice neighbors), the chance of j having another different neighboring ion i at a similar or shorter distance is small. This is indeed the situation of interest for us, since these close-by ions shall exhibit the strongest effective fields which are the easiest to measure in experiment.

The same arguments above for the omission of $N_{4,5}$ lead to omission of any terms in $N_{1,2,3}$ with dipolar interactions between different pairs, so that we can change $\sum_{k \neq j} \sum_{j \neq i} \sum_i V_{kj}^{zx} V_{ij}^{xx}$ in these terms to $\sum_k \tilde{V}_{kj}^{zx} \tilde{V}_{kj}^{xx}$ where j is now ion nearest to k . In the original derivation a slightly more sophisticated approximation was used that considered more ions beside the nearest. However since this approximation only lead to a multiplication of the result by a constant c very close to unity, we disregard it here. Moreover for the purposes of comparison with our numerical results, the derivation is exact in this respect.

We continue the derivation explicitly only for the N_1 terms for brevity as the process is identical for the other terms. We now invoke the completeness relation (twice) to add $|m\rangle \langle m|$ both after J_k^z and between $J_j^x J_i^x$ (other terms in $\sum_{n \in \Lambda} |n\rangle \langle n| = \mathbb{I}$ fall off). We can also omit the summation over p and q , noting that the only contribution comes from p and q states in which the ions excited to Γ_2 match the ions affected by the $J_{j,k}^x$ operators.

$$N_1 = \langle m | 2 \sum_k \tilde{V}_{kj}^{zx} J_k^z | m \rangle \langle m | J_j^x | q \rangle \langle q | 2 \tilde{V}_{jk}^{xx} J_j^x | m \rangle \langle m | J_k^x | p \rangle \langle p | (-g_L \mu_B B^x J_k^x) | m \rangle \quad (\text{B.0.20})$$

This can now be formulated with single ion states of the relevant ions:

$$N_1 = -4g_L \mu_B B^x \sum_k \tilde{V}_{kj}^{zx} \tilde{V}_{kj}^{xx} \langle m_s | J_k^z | m_s \rangle \langle m_s | J^x | \Gamma_2 \rangle \langle \Gamma_2 | J^x | m_s \rangle \langle m_s | J^x | \Gamma_2 \rangle \langle \Gamma_2 | J^x | m_s \rangle$$

$$(B.0.21)$$

where m_s is the single ion state (e.g. $|\uparrow -I^z\rangle$) as dictated for each ion by the global state m .

As in section 3.1, we find $\eta = |\langle \Gamma_2 | J^x | m_s \rangle|^2 = 5.62$ numerically using the code in appendix G.1.

$$N_1 = N_2 = N_3 = -4g_L\mu_B\eta^2 B^x \sum_k \tilde{V}_{kj}^{zx} \tilde{V}_{kj}^{xx} \langle m_s | J_k^z | m_s \rangle \quad (B.0.22)$$

The energy splitting is thus:

$$\begin{aligned} \delta E^{(3)} &= 2 \left(\frac{N_1}{\Omega_0^2} + \frac{N_2}{\Omega_0^2} + \frac{N_3}{2\Omega_0^2} \right) \\ &= 2 \cdot \frac{5}{2} \cdot \frac{4g_L\mu_B\eta^2 B^x \sum_k \tilde{V}_{kj}^{zx} \tilde{V}_{kj}^{xx} \langle m_s | J_k^z | m_s \rangle}{\Omega_0^2} \\ &= 2g_L\mu_B \sum_k \left(\frac{10\eta^2}{\Omega_0^2} \tilde{V}_{kj}^{zx} \tilde{V}_{kj}^{xx} B^x \right) \langle J_k^z \rangle \end{aligned} \quad (B.0.23)$$

where we considered that the contributions of the m and l states is identical up to a minus sign.

The combined contribution of 2nd and 3rd order perturbation corrections to the splitting is therefore:

$$\delta E^{(2)} + \delta E^{(3)} = 2g_L\mu_B \sum_k B_{k,eff}^z \langle J_k^z \rangle \quad (B.0.24)$$

with the ion specific effective longitudinal field:

$$\begin{aligned} B_{k,eff}^z &= 4\tilde{V}_{kj}^{zx} \left(\frac{\eta}{\Omega_0} + \sum_{u=4}^{17} \frac{\eta_u}{E_u - E_m} \right) B^x + \frac{10\eta^2 \tilde{V}_{kj}^{zx} \tilde{V}_{kj}^{xx}}{\Omega_0^2} B^x \\ &= \frac{4\eta \tilde{V}_{kj}^{zx}}{\Omega_0} \left(1 + 0.47 + \frac{1}{4} \frac{10\eta \tilde{V}_{kj}^{xx}}{\Omega_0} \right) B^x \end{aligned} \quad (B.0.25)$$

where this includes the corrections of section B.0.3

B.0.5 Comparison to Numerics

For two ions at nearest lattice positions $\vec{r} = (\frac{a}{2}, 0, \frac{c}{4})$, expanding the states $|\uparrow -\frac{7}{2} \uparrow -\frac{7}{2}\rangle$ and $|\downarrow \frac{7}{2} \downarrow \frac{7}{2}\rangle$ produces the splitting $\delta E_{perturbative} = 0.8135 B^x [K]$ (see code in appendix G.2). This is to be compared with the numerical result (see section 3.2) $\delta E_{numerical} = 0.7993 B^x + 0.0154 (B^x)^3 [K]$ for $0.01 < Bx < 0.1 [T]$ (i.e. well within the perturbative regime) and goodness of fit $R^2 = 1$. A 4th order expansion would produce the terms cubic in B^x

Another test to the validity of our numerical analysis is through the dependence of the energy splitting on the distance between the ions. To do this we consider the second order expansion (the third order has a different dependence on distance) and look at ion pairs which are increasingly separated but

otherwise identically oriented in space. An example of such pairs are ions at lattice sites separated by $\vec{r}_{k,j} = m \cdot \vec{r}_{n.n.} = m \cdot (\frac{a}{2}, 0, \frac{c}{4})$ with integer m (In fact these are exactly the pairs used in the numerical analysis presented below with $m = 1, 4, 5, 8, 9, 12, 13, 16, 17, 20$). For such identically oriented pairs, the dipolar interaction for each pair can be formulated with relation to the dipolar interaction of one of the pairs (e.g. the n.n. pair):

$$\begin{aligned}\tilde{V}_{kj}^{zx} &= \frac{1}{2} g_L^2 \mu_B^2 \frac{\mu_0}{4\pi} \frac{-3z_{kj}x_{kj}}{|r_{kj}|^5} = \frac{1}{2} g_L^2 \mu_B^2 \frac{\mu_0}{4\pi} \frac{-3|r_{kj}| \cos \theta |r_{kj}| \sin \theta \cos \phi}{|r_{kj}|^5} \\ &= \frac{\text{const}}{|r_{kj}|^3} = \frac{\text{const}}{|r_{n.n.}|^3} \cdot \frac{1}{m^3} \\ &= \tilde{V}_{n.n.}^{zx} \cdot \frac{1}{m^3}\end{aligned}\tag{B.0.26}$$

The energy splitting between states $|\uparrow -\frac{7}{2} \uparrow -\frac{7}{2}\rangle$ and $|\downarrow \frac{7}{2} \downarrow \frac{7}{2}\rangle$ for these pairs now reads:

$$\begin{aligned}\delta E^{(2)}(B^x, m) &= 4g_L \mu_B \langle J^z \rangle \cdot 4\Theta \frac{\tilde{V}_{n.n.}^{zx}}{m^3} B^x \\ &= \frac{A}{m^3} B^x\end{aligned}\tag{B.0.27}$$

with the constant $A = 0.8169[\frac{K}{T}]$.

We numerically found these energy splittings at field values $0.01 < Bx < 0.1[T]$ (again well within the perturbative regime) and applied a linear fit to the results for each pair to extract the linear slope ($\frac{A}{m^3}$) in B^x (all the fits proved to be highly linear with goodness of fit $R^2 = 1$). Next we applied a power fit ($y = A \cdot m^b$) to these slopes to test whether the energy splitting indeed decays cubically with distance as expected. This was indeed validated by the fit with $A = 0.7995$ and $m = -2.999$ and goodness of fit $R^2 = 1$. The slight difference in the linear coefficient in B^x ($A = 0.7995$) with respect to the numerical result mentioned in the first paragraph of this section ($A = 0.7993$) is because different polynomial fits were used to retrieve the linear slopes (here a 1st order polynomial and before a 3rd order polynomial was used).

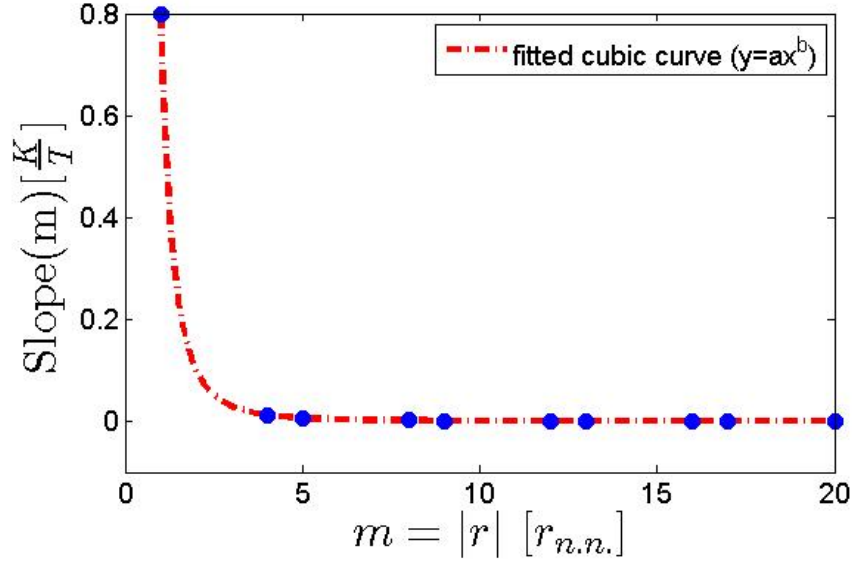


Figure B.4: Power fit to the slopes (with B^x) of the energy splittings of pairs separated by $\vec{r}_{k,j} = m \cdot \vec{r}_{n.n.} = m \cdot (\frac{a}{2}, 0, \frac{c}{4})$ with $m = 1, 4, 5, 8, 9, 12, 13, 16, 17, 20$

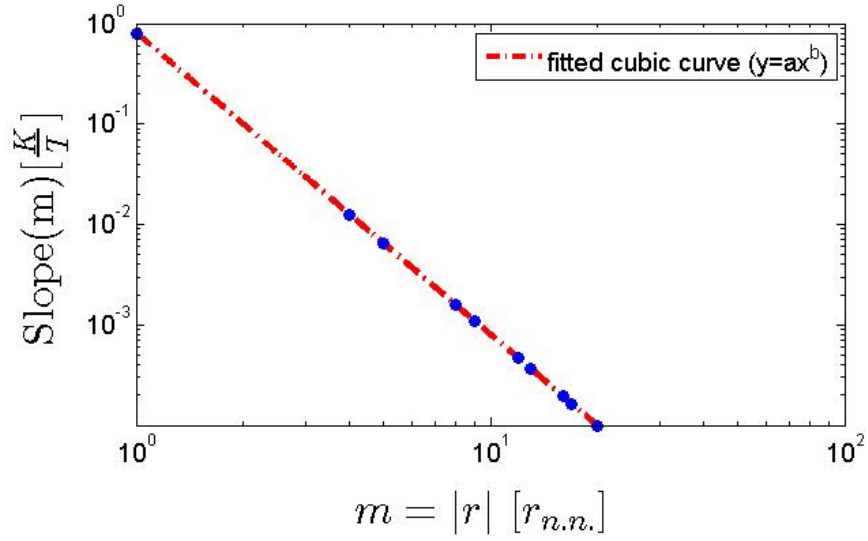


Figure B.5: Log-log plot of the power fit to the slopes (with B^x) of the energy splittings of pairs separated by $\vec{r}_{k,j} = m \cdot \vec{r}_{n.n.} = m \cdot (\frac{a}{2}, 0, \frac{c}{4})$ with $m = 1, 4, 5, 8, 9, 12, 13, 16, 17, 20$

Appendix C

Iterative Diagonalization

The results presented in section 3.2 and appendix D (e.g. fig. 3.1) were obtained using the Arnoldi method for solving eigenvalue problems for large sparse matrices. The Arnoldi method is a generalization of the Lanczos method (to non-symmetric matrices) and is an iterative diagonalization method. That is, through repeated iterations this method finds a few, say k , largest (or lowest) eigenvalues of a matrix. It also finds the appropriate eigenstates. The Arnoldi method is provided as an integral part of Matlab within the ARPACK package.

There are two main advantages to iterative methods. First and foremost, these methods allow us to store only the non-zero elements of a $(n \times n)$ matrix A , thereby reducing storage requirements. The original matrix A thus only requires storage proportional to $Nz(A)$ (where $Nz(A)$ is the number of non-zero elements in the matrix A) with $Nz(A) \ll n^2$ for large sparse matrices. The storage required for the process itself and afterwards to store the eigenvalues and eigenstates is of the order of $\mathcal{O}(n \cdot k) + \mathcal{O}(k^2)$ [33]. In our case ($n = 18496$, $k = 576$) this corresponds to only around $(18496 \times 576 \times 16 \text{ Bytes} \simeq) 170 \text{ MB}$ instead of $(18496 \times 18496 \times 16 \text{ Bytes} \simeq) 5.5 \text{ GB}$. Furthermore an iterative method can produce results considerably faster. While a standard diagonalization process requires a number of basic operations on the order of $\mathcal{O}(n^3)$, an estimation of the complexity of the Arnoldi method is $\mathcal{O}(Nz(A)) + \mathcal{O}(n \cdot k)$ operations [34].

A thorough overview of the Arnoldi and Lanczos methods is too lengthy for this thesis and can be found elsewhere (e.g. [34, 35]). Instead we briefly discuss the power method which is the archetypal iterative method and underlies most other iterative methods including the Arnoldi method.

The power method can be used to find the largest magnitude eigenvalue λ_1 of a matrix A . We assume this largest eigenvalue to be non-degenerate ($|\lambda_1| > |\lambda_i|$ for any $i \neq 1$). An initial vector b_0 is randomly

chosen. In the basis of the (yet unknown) eigenstates v_i ($Av_i = \lambda_i v_i$) this vector can be formulated as:

$$b_0 = c_1 v_1 + c_2 v_2 + \dots + c_n v_n \quad (\text{C.0.1})$$

with the further assumption of $c_1 \neq 0$.

We now iteratively multiply the initial vector b_0 by the matrix A (say p times):

$$\begin{aligned} b_p &= A \cdot A \cdot \dots \cdot A \cdot b_0 = A^p b_0 \\ &= c_1 A^p v_1 + c_2 A^p v_2 + \dots + c_n A^p v_n \\ &= c_1 \lambda_1^p v_1 + c_2 \lambda_2^p v_2 + \dots + c_n \lambda_n^p v_n \\ &= c_1 \lambda_1^p \left[v_1 + \frac{c_2}{c_1} \left(\frac{\lambda_2}{\lambda_1} \right)^p v_2 + \dots + \frac{c_n}{c_1} \left(\frac{\lambda_n}{\lambda_1} \right)^p v_n \right] \end{aligned} \quad (\text{C.0.2})$$

until convergence is achieved (i.e. until $\left(\frac{\lambda_{i \neq 1}}{\lambda_1} \right)^p \ll 1$ for any i) at which point to a good approximation:

$$b_p \simeq c_1 \lambda_1^p v_1 \quad (\text{C.0.3})$$

Thus the power method produces a vector which approaches a multiple of the eigenstate v_1 with increasing iterations. Some details necessary for practical algorithms (e.g. to prevent overflow / divergence) were omitted in this review to make it short and clear. Further details can be found elsewhere (e.g. [36]).

Appendix D

Further Numerical Results for Section 3.2

This appendix includes further numerical results obtained and used within this study, that did not appear in the main text and are relevant directly to section 3.2 (these results were also used in the analysis of chapter 4). A few results appearing in section 3.2 are presented again for comparison.

The next four plots (figs. D.1 through D.4) present the energy levels for transverse fields between 0 and $2T$ for nearest neighbor (n.n.), 3^{rd} n.n., and 4^{th} n.n. pairs.

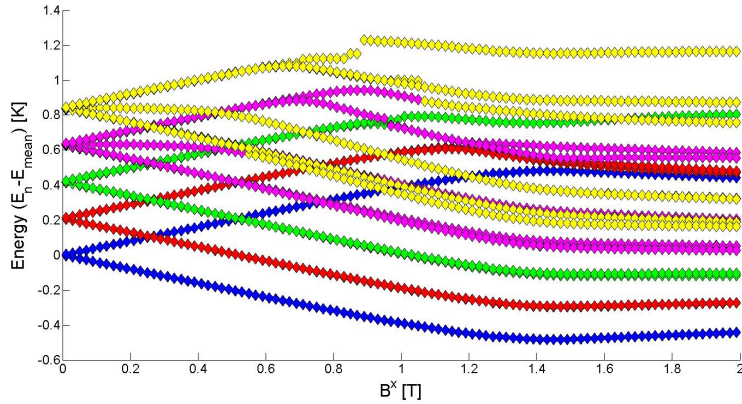


Figure D.1: *Energy levels Vs. B^x for n.n. pairs at relative positions $\vec{r} = (\pm\frac{1}{2}a, 0, \frac{1}{4}c)$ ('first' orientation)*

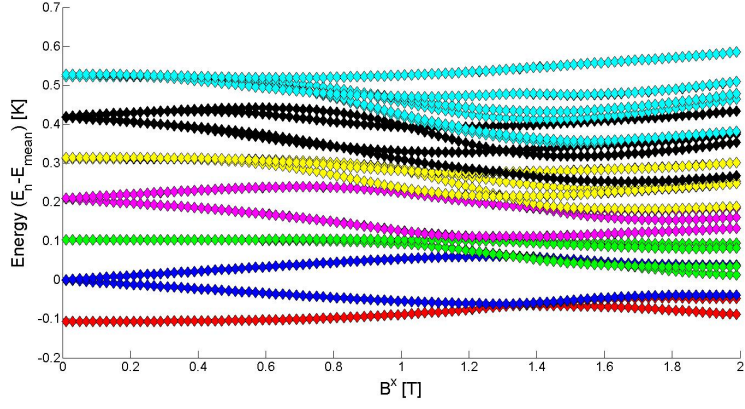


Figure D.2: Energy levels Vs. B^x for 3rd n.n. pairs at relative positions $\vec{r} = (\pm a, \pm \frac{1}{2}a, -\frac{1}{4}c)$ ('first' orientation).

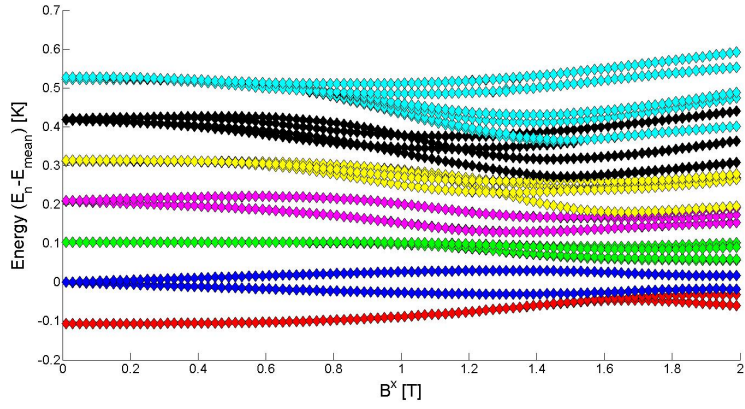


Figure D.3: Energy levels Vs. B^x for 3rd n.n. pairs at relative positions $\vec{r} = (\pm \frac{1}{2}a, \pm a, \frac{1}{4}c)$ ('second' orientation).

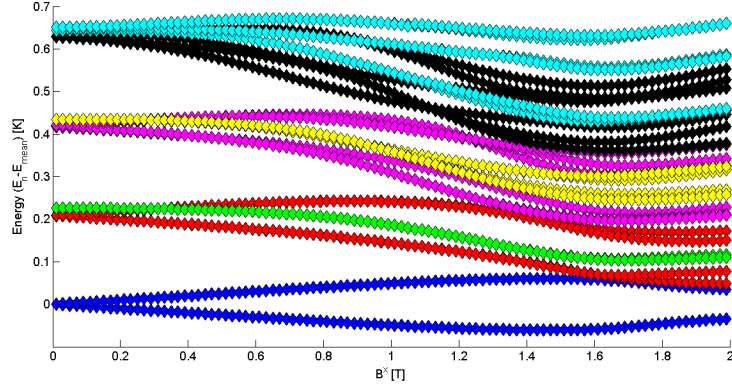


Figure D.4: *Energy levels Vs. B^x for 4th n.n. pairs at relative positions $\vec{r} = (\pm\frac{1}{2}a, \pm\frac{1}{2}a, \pm\frac{1}{2}c)$*

Explanatory notes:

- Only the first 32 levels are shown for clarity.
- The color scheme is determined according to the degeneracies at zero field. Each diabatic state should retain its color as B^x changes.
- All energies are relative to the mean between the states starting (at zero field) as $|\uparrow -\frac{7}{2} \uparrow -\frac{7}{2} >$ and $|\downarrow \frac{7}{2} \downarrow \frac{7}{2} >$ (i.e. relative to the mean between blue lines).
- 2nd n.n. pairs ,e.g. $\vec{r} = (a, 0, 0)$, are not presented as they do not show removal of degeneracy as indeed predicted by perturbation theory (no ODD terms at all).
- For the same reason, n.n. pairs of the 'second' orientation $\vec{r} = (0, \pm\frac{a}{2}, -\frac{c}{4})$ (see appendix A.1) are not presented (no V^{xz} terms leading to zero splitting for an applied field along the x axis).
- The 3rd n.n. pairs of the 'second' possible orientation $\vec{r} = (\pm\frac{1}{2}a, \pm a, \frac{1}{4}c)$ (see appendix A.1), are given here for completeness. As shown below, these pairs produce only a weak effective field compared to the 'first' orientation for 3rd n.n. pairs and to any of the other pairs presented here.

Plots of the energy difference between the $|\uparrow -\frac{7}{2} \uparrow -\frac{7}{2}\rangle$ and $|\downarrow \frac{7}{2} \downarrow \frac{7}{2}\rangle$ states:

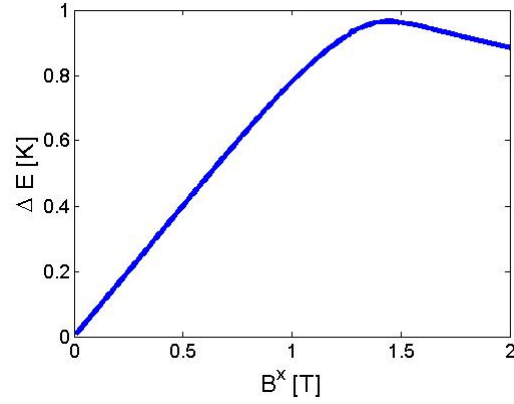


Figure D.5: Energy difference between the $|\uparrow -\frac{7}{2} \uparrow -\frac{7}{2}\rangle$ and $|\downarrow \frac{7}{2} \downarrow \frac{7}{2}\rangle$ for n.n. pairs at relative positions $\vec{r} = (\pm\frac{1}{2}a, 0, \frac{1}{4}c)$ ('first' orientation)

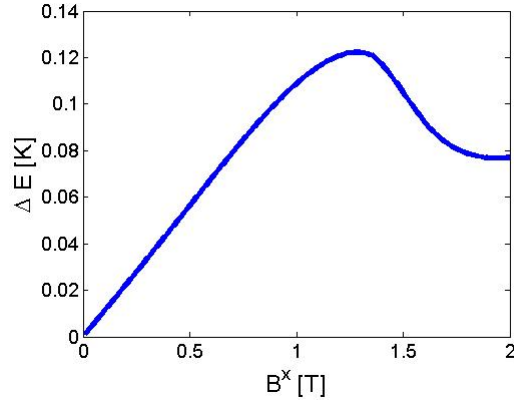


Figure D.6: Energy difference between the $|\uparrow -\frac{7}{2} \uparrow -\frac{7}{2}\rangle$ and $|\downarrow \frac{7}{2} \downarrow \frac{7}{2}\rangle$ for 3rd n.n. pairs at relative positions $\vec{r} = (\pm a, \pm\frac{1}{2}a, -\frac{1}{4}c)$ ('first' orientation:)

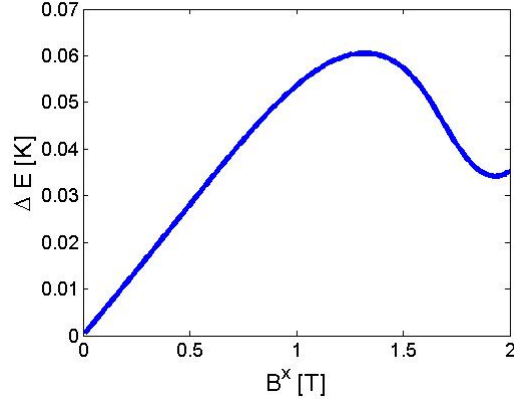


Figure D.7: Energy difference between the $|\uparrow -\frac{7}{2} \uparrow -\frac{7}{2}\rangle$ and $|\downarrow \frac{7}{2} \downarrow \frac{7}{2}\rangle$ for 3rd n.n. pairs at relative positions $\vec{r} = (\pm\frac{1}{2}a, \pm a, \frac{1}{4}c)$ ('second' orientation:)

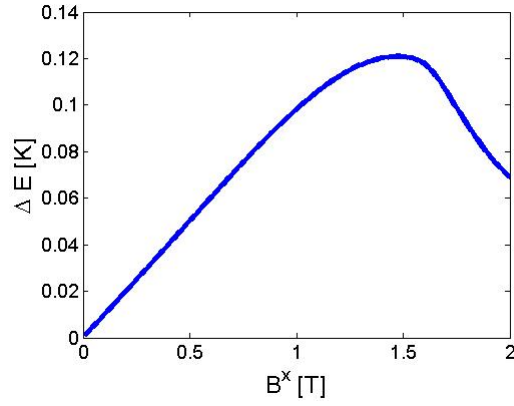


Figure D.8: Energy difference between the $|\uparrow -\frac{7}{2} \uparrow -\frac{7}{2}\rangle$ and $|\downarrow \frac{7}{2} \downarrow \frac{7}{2}\rangle$ for 4th n.n. pairs at relative positions $\vec{r} = (\pm\frac{1}{2}a, \pm\frac{1}{2}a, \pm\frac{1}{2}c)$

Effective longitudinal fields:

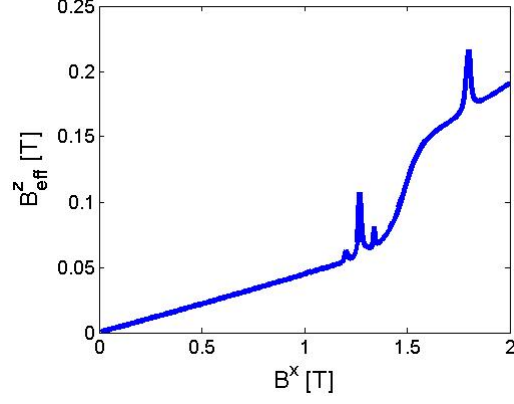


Figure D.9: *Effective longitudinal field Vs. B^x for n.n. pairs at relative positions $\vec{r} = (\pm\frac{1}{2}a, 0, \frac{1}{4}c)$ ('first' orientation:)*

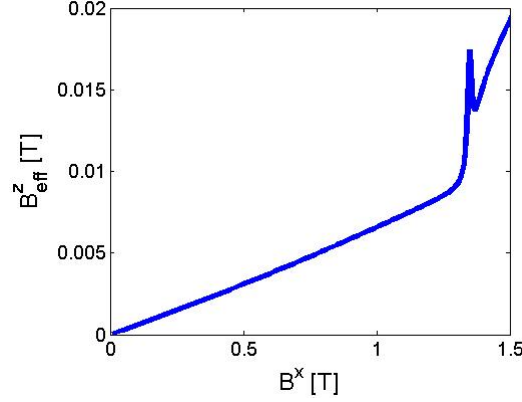


Figure D.10: *Effective longitudinal field Vs. B^x for 3rd n.n. pairs at relative positions by $\vec{r} = (\pm a, \pm\frac{1}{2}a, -\frac{1}{4}c)$ ('first' orientation:). The transverse field range is shorter here compared to the other plots since at higher fields there are sharp jumps that require scaling up the vertical axis too much*

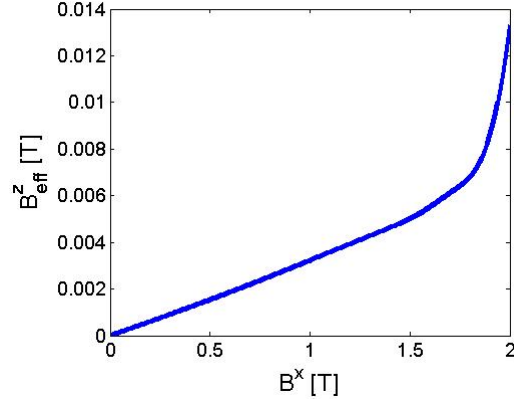


Figure D.11: *Effective longitudinal field Vs. B^x for 3rd n.n. pairs at relative positions $\vec{r} = (\pm\frac{1}{2}a, \pm a, \frac{1}{4}c)$ ('second' orientation:)*

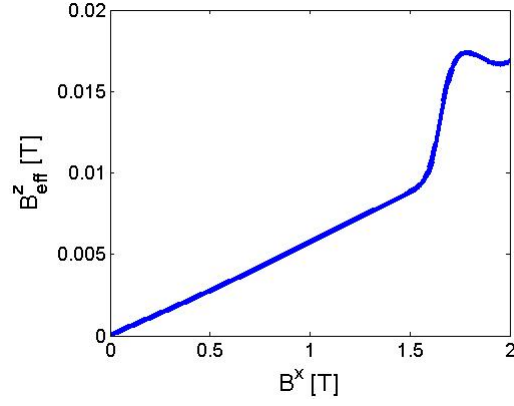


Figure D.12: *Effective longitudinal field Vs. B^x for 4th n.n. pairs at relative positions $\vec{r} = (\pm\frac{1}{2}a, \pm\frac{1}{2}a, \pm\frac{1}{2}c)$*

Appendix E

Further Plots for Chapter 4

This appendix includes further figures, that did not appear in the main text and are relevant to chapter 4. We remind the reader that, much like in chapter 4, all the plots in this chapter are approximated using the linear fits to the energy differences and effective fields found in section 3.2 (and appendix D).

E.1 A Second Example for Section 4.1

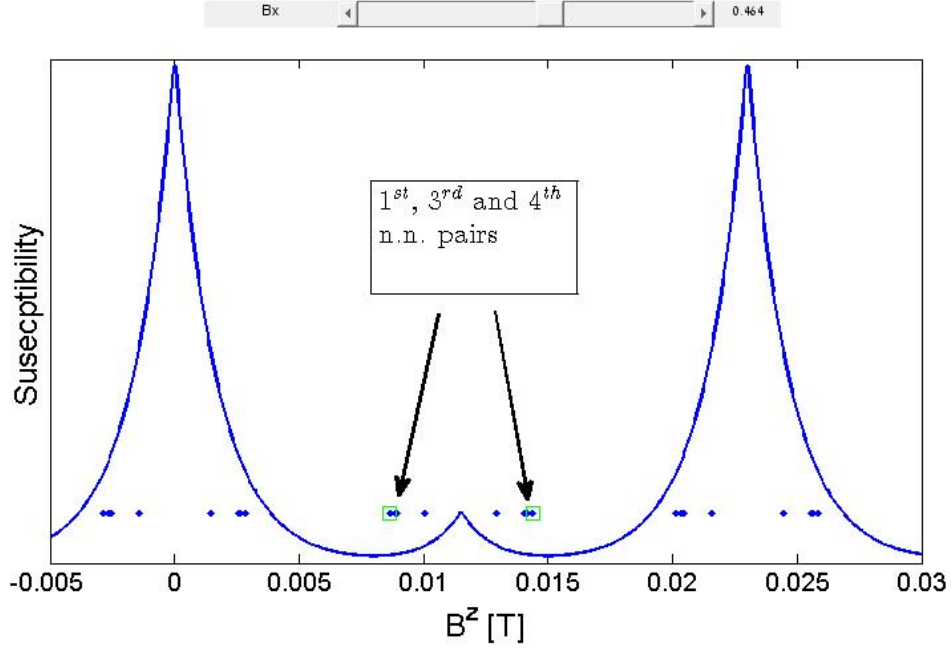


Figure E.1: Predicted positions of shifted susceptibility χ^{zz} peaks for $B^x = 0.464[T]$. Blue lines illustrate the original peaks for perspective. Green squares mark valley minima. Blue dots represent shifted peaks positions. The shifted peaks which are expected to be clearly visible in experiment are noted. All other shifted peaks (dots) in this plot are expected to simply widen the unshifted peaks

Figure E.1 represents another example of optimal visibility for shifted susceptibility χ^{zz} peaks for $B^x = 0.464[T]$. This example features the shifted peaks of 3rd and 4th n.n. pairs. This figure was made using the code in appendix G.5. The blue lines representing the original peaks are illustrations drawn for perspective only and should *not* be taken as a prediction for the size and functional form of the real peaks.

E.2 Refined Plots for Section 4.2

In section 4.2 we presented surface plots of Magnetization and Susceptibility as a function of both B^x and B^z but we did not take into account the dependency of J^z (for the ground states) on B^x (or on B^z). This

dependency was explicitly shown in section 3.2 (fig. 3.3). Of course the J^z value affects the magnetization, and even in the $0 < |B^x| < 1$ T range this could lead to as much as a 10% discrepancy.

Though it would not be feasible to find $J^z(B^x)$ for the ground states of every pair, a first approximation is to use the $J^z(B^x)$ values of the single ion picture, since the ions in most pairs are far apart (and therefore behave much like single ions). As the $J^z(B^x)$ line shape does not vary much for the different pairs (atleast in the regime $0 < |B^x| < 1$ T, see figure E.2), this should be a good approximation even for nearer neighbors. To calculate the $J^z(B^x)$ values for a single ion correctly a small longitudinal field $B^z = 0.001$ [T] is taken into account. This is in order to avoid the unphysical situation of an ion in a crystal experiencing zero (longitudinal) field, as obviously there will always be at least some small field due to the ions around it. The absence of a longitudinal field would have led to the unphysical outcome of the ion being in a completely symmetric/antisymmetric state $|\uparrow\rangle \pm |\downarrow\rangle$ with $J^z(B^x) = 0$. The value $B^z = 0.001$ [T] is the typical field magnitude experienced by a Ho ion due to all other Ho ions in the crystal. Figure E.2 shows the $J^z(B^x)$ values for a single ion and for a few pairs for comparison.

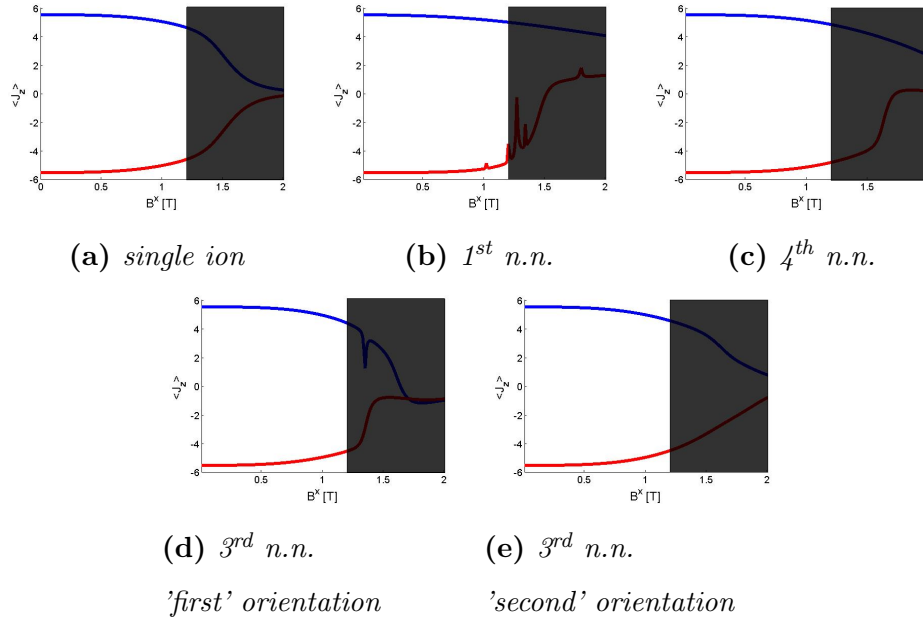


Figure E.2: $J^z(B^x)$ expectancy value for several pairs and for a single ion. The parts of the plots which correspond to $B^x > 1.2$ [T] are shaded noting that this is outside the range where our predictions are valid.

The dependency of J^z on B^z only becomes significant at high transverse fields of around $1T$. Figure E.3 shows the $J^z(B^z)$ dependency for several B^x values.

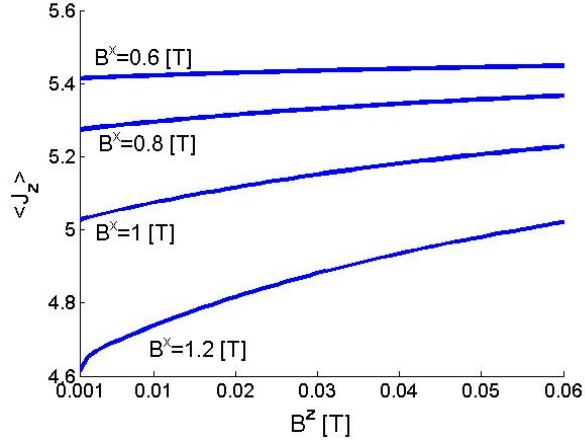
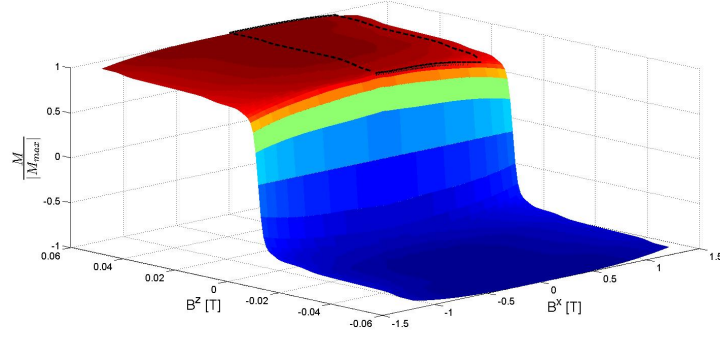


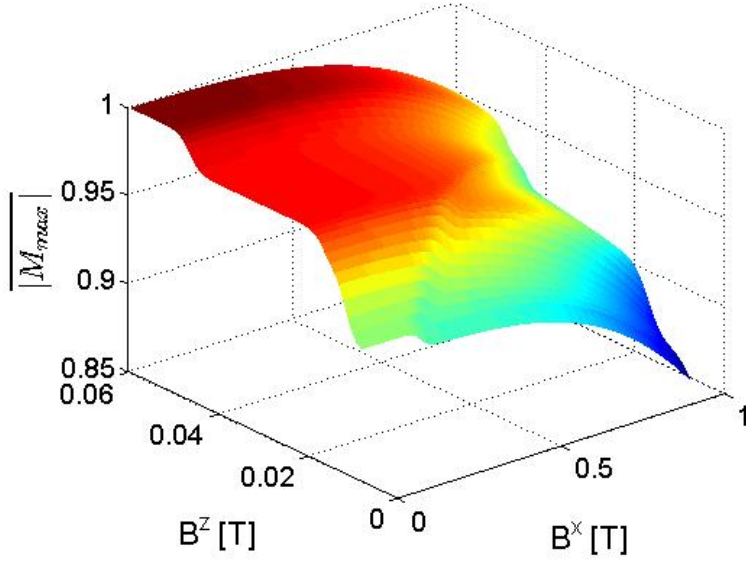
Figure E.3: $J^z(B^z)$ expectancy value of a single ion for several B^x values

Within the $-0.06 < B^z < 0.06T$ range, and for the B^x values $0.6T$, $0.8T$, $1T$ and $1.2T$, the $J^z(B^z)$ changes by 0.5%, 2%, 4% and 8% appropriately. We therefore conclude that this effect can be neglected as long as $B^x < 0.8$ (as in the suggested experiment in section 4.2.1).

Figures E.4 through E.6 show the magnetization and Susceptibility ($\chi^{zz} = \frac{\partial M^z(B^x, B^z)}{\partial B^z}$) using the $J^z(B^x, B^z)$ values found for a single ion.



(a)



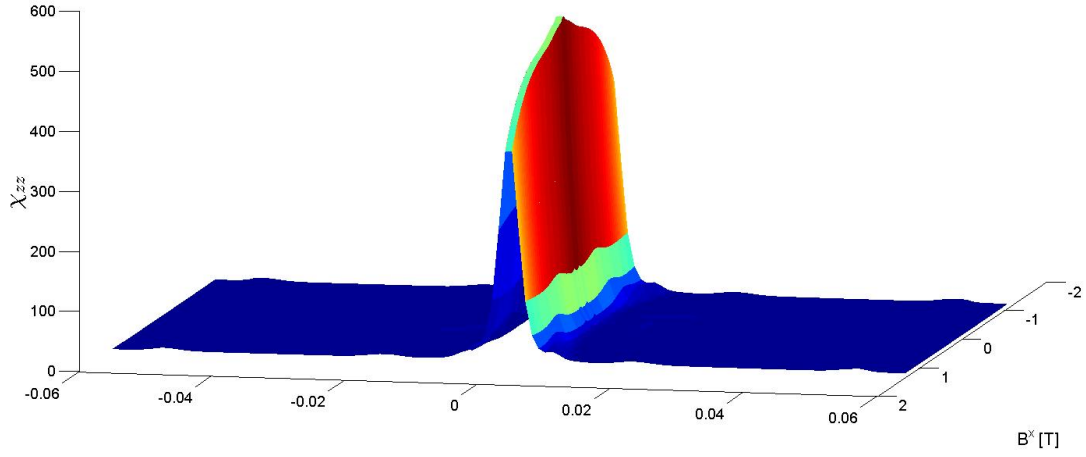
(b)

Figure E.4: Predicted Magnetization taking into account $J^z(B^x, B^z)$ values found for a single ion.

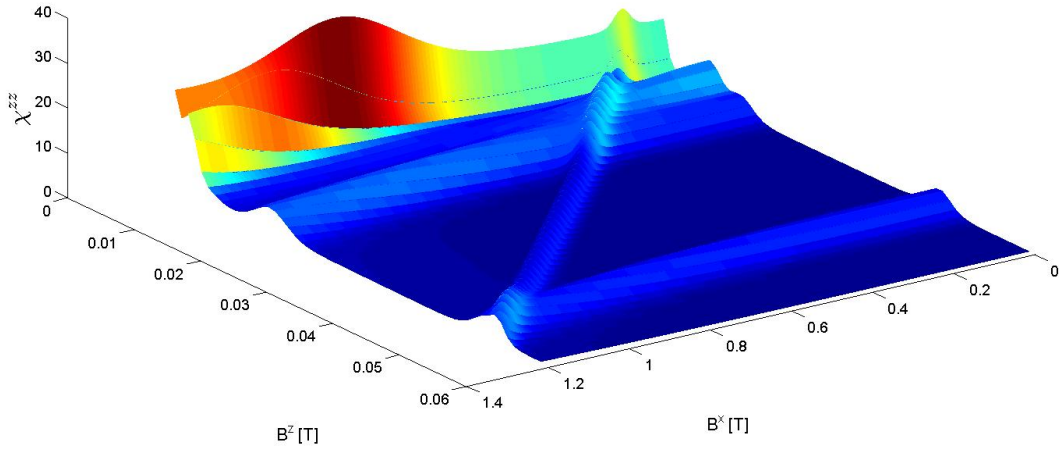
a) $-0.06 < B^z < 0.06T$; $-1.2 < B^x < 1.2T$.

b) $0.005 < B^z < 0.06T$; $0 < B^x < 1T$. (zoom in)

$T = 10[mK]$, $x = 0.005$ (broadening is not taken into account here).



(a)



(b)

Figure E.5: Predicted Susceptibility to B^z ($\frac{\partial M^z(B^x, B^z)}{\partial B^z}$) taking into account $J^z(B^x, B^z)$ values found for a single ion.

a) $-0.06 < B^z < 0.06T$; $-1.2 < B^x < 1.2T$.

b) $0.004 < B^z < 0.06T$; $0 < B^x < 1.2T$. (zoom in)

$T = 10[mK]$, $x = 0.005$ (broadening is not taken into account here).

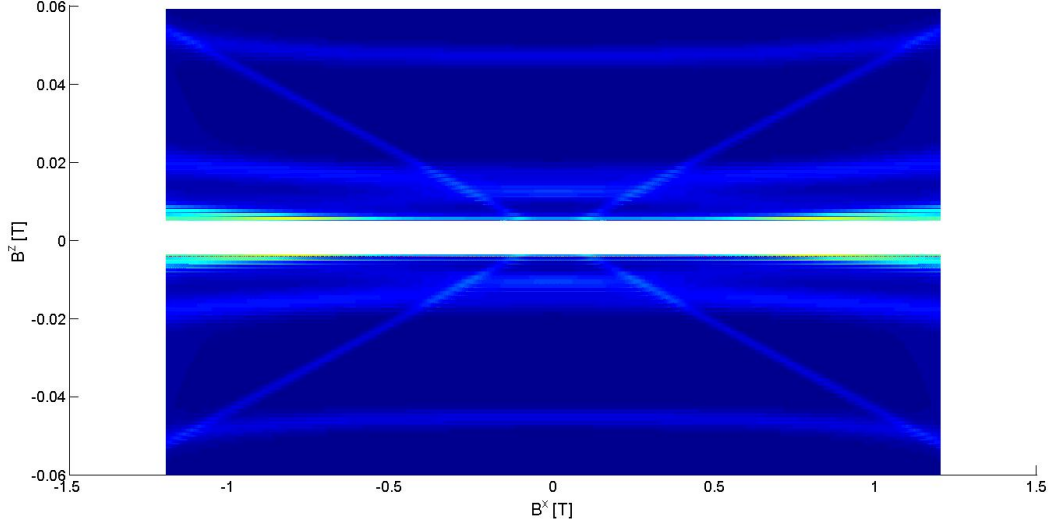


Figure E.6: *Projection of the susceptibility (χ^{zz}) on the $B^x B^z$ plane for applied fields $-0.06 < B^z < 0.06T$; $-1.2 < B^x < 1.2T$ taking into account $J^z(B^x, B^z)$ values found for a single ion. The area of the big susceptibility peak at zero longitudinal field ($-0.004 < B^z < 0.004T$) was cut off for better visibility of areas outside the big peak.*

$T = 10[mK]$, $x = 0.005$ (broadening is not taken into account here).

Appendix F

Landau-Zener Transition Profile

The transition profile, meaning the amount of ions tunnelling at resonances and the functional form of the peaks in susceptibility (both unshifted and shifted peaks) can be derived for zero temperature using the Landau-Zener approximation [37] [38]. The actual experimental results can be very different (as discussed in section 2.5.2) due (for example) to thermal excitation to levels where the energy gap of the crossing is larger. The relative contribution of this thermally assisted tunnelling compared to pure quantum mechanical tunnelling depends on the applied transverse field and the sweep rate as discussed below (as well as the temperature of course).

The assumptions required to make the Landau-Zener approximation are that the energies of the diabatic states change linearly and that the coupling between them is constant throughout the avoided level crossing. Of course if the crossing region is small enough, these assumptions can be said to hold in any case as a first approximation. In our specific case, the diabatic states as a function of applied longitudinal fields are highly linear as shown in section 3.2. As the crossing regions are small compared to the distance between crossings, the coupling can be taken as constant. This is true even though the resonances of interest involve states which are almost degenerate giving crossings which can be quite close to each other in B^z (of order $50\mu T$ see fig. F.1b). In the following analysis we consider the simplified case where coupling to the environment is very weak (zero temperature) and can be neglected. In general the coupling to the environment can change the transition profile and overall transition probability due to dephasing and dissipation effects (cf. [39] [40] [41]).

For each crossing, the reduced Schrödinger equation describing the subspace of the two crossing states

is:

$$i\hbar \frac{d}{dt} \begin{pmatrix} C_1 \\ C_2 \end{pmatrix} = \begin{pmatrix} -\hbar\Delta & \hbar\Omega \\ \hbar\Omega & \hbar\Delta \end{pmatrix} \begin{pmatrix} C_1 \\ C_2 \end{pmatrix} \quad (\text{F.0.1})$$

where $\pm\hbar\Delta$ are the energy values of the diabatic states with zero energy chosen at the intersection of the diabatic states, and $\hbar\Omega$ the (constant) coupling between the diabatic states.

In terms of the known system parameters:

$$\Omega = \frac{\delta E}{2\hbar} \quad (\text{F.0.2})$$

where δE is the gap between the energy levels at the crossing and:

$$\Delta = \frac{|\alpha|t}{2\hbar} \quad (\text{F.0.3})$$

with $|\alpha_{sf\backslash co}| = c_{sf\backslash co} \cdot 2\nu\mu_B g_L| < J^z > |$ being the rate of change of the energy difference between the diabatic states. $c_{sf\backslash co}$ is an artificially added parameter taking into account the difference between "single-flip" crossings ($c_{sf} = 1$) and co-tunnelling ($c_{co} = 2$). In the single spin picture only α_{sf} is used.

The overall transition probability to stay in the same diabatic state is given by the well-known result [38]:

$$P_D = e^{-\pi \frac{\delta E^2}{2\hbar|\alpha|}} \quad (\text{F.0.4})$$

Making the probability for a magnetic moment flip:

$$P_F = 1 - e^{-\pi \frac{\delta E^2}{2\hbar|\alpha|}} \quad (\text{F.0.5})$$

δE (through the coupling $\Omega = \frac{\delta E}{2\hbar}$ between the diabatic states involved) depends exponentially on B^x as was shown by Schechter and Stamp [17] (see fig. 4 there).

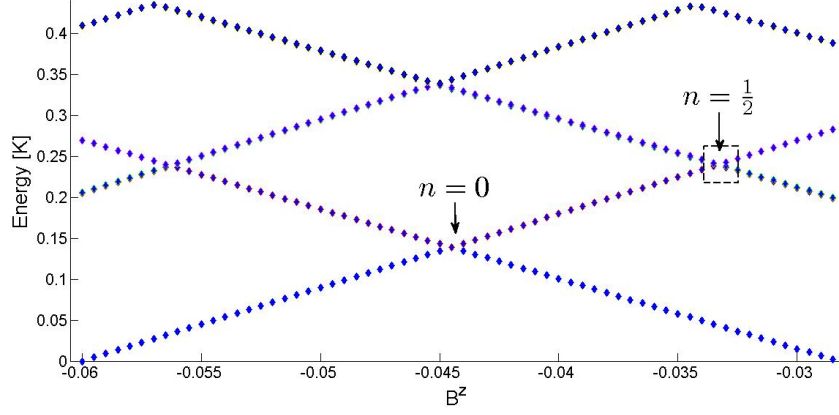
In order to predict the functional form of the susceptibility peaks, the Schrödinger equations were solved numerically (see Numerical Routine in appendix F) following the work of Vitanov [42].

The energy gaps ΔE for the different crossings were found using the exact diagonalization of the Hamiltonian in applied constant transverse and varying longitudinal fields (see Numerical Routine in appendix G.6).

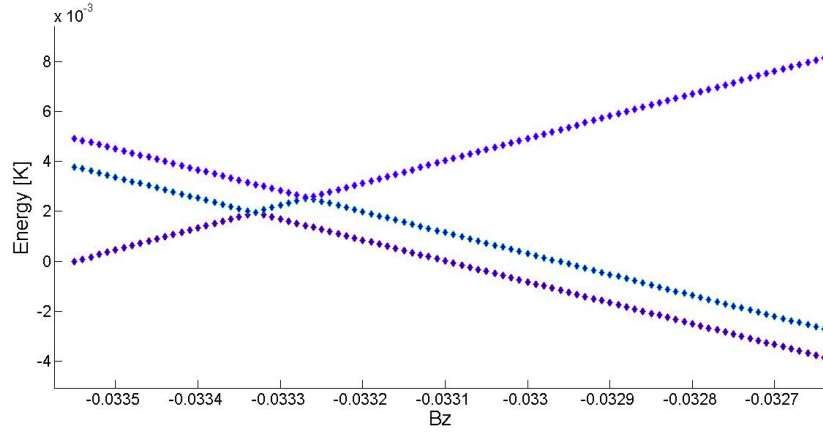
The results of this analysis predict the behaviour of a single pair of ions initially populating a specific level (two ion picture). To extrapolate for the entire crystal we need to know for each sweep of applied longitudinal field, the initial population of all the states. This is feasible only when the crystal is allowed thermal relaxation between sweeps, so that only the ground state is significantly populated i.e. the process

starts from thermal equilibrium. For that reason we assume initial thermal equilibrium in the following analysis.

We offer as an example a prediction for the behaviour of a single n.n. pair near the $n = \frac{1}{2}$ crossing in energy levels (as a function of B^z) for a transverse field $B^x = 1[T]$. Figure F.1 shows the crossing in energy levels for the $n = \frac{1}{2}$ resonance.



(a)



(b)

Figure F.1: $n = \frac{1}{2}$ crossing in energy levels for the n.n. pairs Vs. B^z . $T = 0$. $B^x = 1[T]$.

a) a wider perspective b) zoom in on the area noted by a dashed rectangle in (a)

From the zoom in (F.1b) we can see that the $n = \frac{1}{2}$ crossing is in fact two slightly separate crossings

of different energy levels (which would be degenerate for zero longitudinal and transverse fields). In the following analysis we shall treat the 'second' crossing at a more positive B^z value of the two.

Figure F.2 shows the probability that the pair would flip. The magnetization contribution of this pair to the co-tunnelling resonance is of course proportional to this probability.

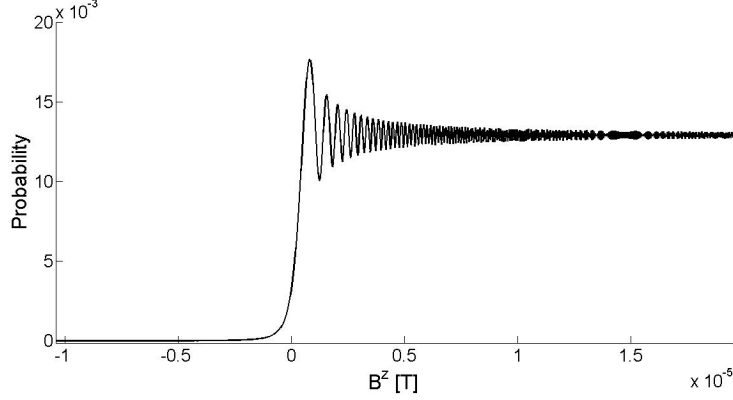


Figure F.2: *Probability of a flip by a single n.n. pair for the $n = \frac{1}{2}$ crossing. $T = 0$. $B^x = 1[T]$*

For an ensemble of such pairs we have to take into account broadening due to effective fields generated by the surrounding Ho ions and HF interaction with the Fluorine ions. Such a broadening of $0.5mT$ was applied in figure F.3.

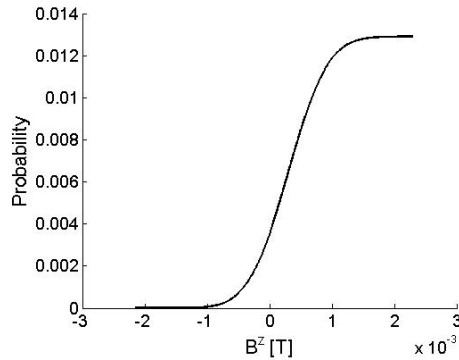


Figure F.3: *Probability of a flip of a n.n. pair in an ensemble for the $n = \frac{1}{2}$ crossing with a broadening of $500\mu T$. $T = 0$. $B^x = 1[T]$*

It turns out that the broadening dictates the functional form of the crossing, since it is much greater

than the width of the single pair crossing ($\sim 1\mu T$). The Landau-Zener approximation then is only used to find the overall transition probability.

The derivative of the broadened probability plot gives (up to a multiplicative factor) the line shape of the susceptibility (χ^{zz}).

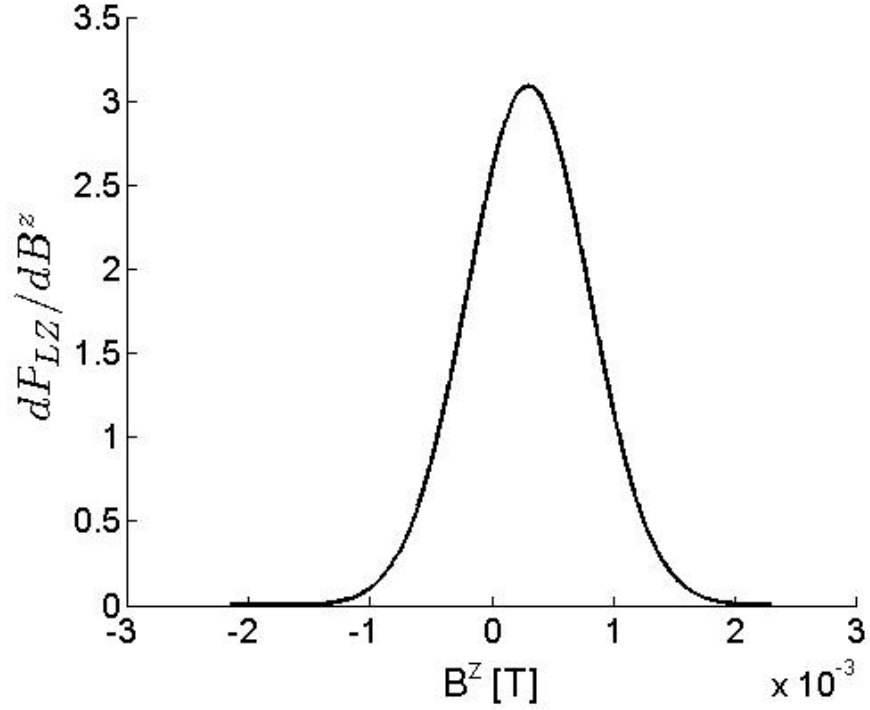


Figure F.4: *Susceptibility (up to a multiplicative constant) Vs. B^z for an ensemble of n.n. pairs at the $n = \frac{1}{2}$ crossing with a broadening of $500\mu T$. $T = 0$. $B^x = 1[T]$*

Appendix G

Numerical Routines

G.1 Finding the 17 Crystal Field States

The following code designated *Crystal_Field.m* finds the 17 eigenstates of the Crystal Field Hamiltonian (i.e. the electronic single ion states).

Standard Matlab diagonalization process (not iterative) is applied. The operator equivalents O_n^l are initially given in a basis ordered according to increasing J_z values. Before diagonalization of the Crystal Field Hamiltonian, the basis states are reordered to get a block diagonal matrix for this Hamiltonian. This is done in order for Matlab to give eigenstates each within the manifold of only one of the irreducible representation $\Gamma_{1,2,3,4}$ (some of the eigenstates are degenerate so that any linear combination of them is also an eigenstate).

The code also finds the J^z expectancy values for the different eigenstates and produces the J^x and J^y matrices so that one can check that these matrices have no non-zero components in the subspace of the ground state doublet.

```
%% % Defining Basic Parameters

%—— Setting up the basic matrices of the problem: J^2, Jz, Jx, Jy, J+ J- ——

%Setting J value
J=8;

%Defining J^2 (called J2) as the identity matrix times J(J+1)
J2=J*(J+1)*eye((2*J+1));

%Defining a vector containing the diagonal elements of jz
```

```

VECjz=(-J:J);
jz=diag(VECjz);

%This loop builds the vector of the non-zero values of jplus (and jminus) which
%are found on the secondary diagonal below (above) the main one.
VECjplusminus=zeros(1,(2*J+1)-1);
for t=J:J-1
    VECjplusminus(t+J+1)=sqrt(J*(J+1)-t*(t+1));
end

jplus=diag(VECjplusminus,-1);
jminus=diag(VECjplusminus,1);

%—— Setting up the Operator Equivalents and the Crystal Field Parameters (CFP) ——

O20=3*jz^2-J2;
%Building the O40 operator equivalent from previously defined matrices
O40=35*jz^4-30*J2*jz^2+25*jz^2-6*J2+3*(J2)^2;
%Building the O44c operator equivalent from previously defined matrices
O44c=(jplus^4+jminus^4)/2;
%Building the O60 operator equivalent from previously defined matrices
O60=231*jz^6-315*J2*jz^4+735*jz^4+105*(J2)^2*jz^2-525*J2*jz^2+294*jz^2-5*(J2)^3 ...
+40*(J2)^2-60*J2;

%Building the O64c operator equivalent from previously defined matrices

%The matrices (jplus^4+jminus^4) and (11*jz^2-J2-38) are both
%hermitian so that hermitian conjugation of their multiplication simply
%gives a multiplication in the opposite order (A*B)'=B'*A'
O64c=((jplus^4+jminus^4) * (11*jz^2-J2-38*eye(2*J+1)) + ...
      ((jplus^4+jminus^4) * (11*jz^2-J2-38*eye(2*J+1))' )' )/4;

%Building the O64s operator equivalent from previously defined matrices
O64s=(jplus^4-jminus^4) * (11*jz^2-J2-38*eye(2*J+1)) /(4*1i) + ...
      ((jplus^4-jminus^4) * (11*jz^2-J2-38*eye(2*J+1))' )' /(4*1i) )';

%Assigning the values for the Crystal Field Parameters from PRB 70,144411(2004)
%by Chakraborty et al. – Theory of the magnetic phase diagram of LiHoF4
B20=-0.696; %Kelvin
B40=4.06*10^(-3); %Kelvin
B60=4.64*10^(-6); %Kelvin
B44c=0.0418; %Kelvin
B64c=8.12*10^(-4); %Kelvin
B64s=1.137*10^(-4); %Kelvin

```

```

Vc=B20*O20+B40*O40+B60*O60+B44c*O44c+B64c*O64c+B64s*O64s;

%% %Changing Basis and finiding eigenstates and eigenvalues

%Here I change the numbering of the states so that I get a Block diagonal
%matrix for Vc.
%BC gives the new numbering compared to the old.
BC=[2,6,10,14,4,8,12,16,1,5,9,13,17,3,7,11,15];
%This changes the order of the states in the relevant operators according to BC
Vc=Vc(BC,BC);
jz=jz(BC,BC);
jplus=jplus(BC,BC);
jminus=jminus(BC,BC);

%Finding the eigenstates and eigenvalues
[EVc,ES]=eig(Vc);

%Finding the expectancy value of Jz for the different eigenstates
Jz=EVc\jz*EVc;
Jz_expectancy=diag(Jz);

%Building the jx matrix from the j minus and jplus matrices
jx=(jplus+jminus)/2;
%Building the jy matrix from the j minus and jplus matrices
jy=(jplus-jminus)/(2i);
%Changing basis to check that Jx and Jy have no non-zero components in the
%subspace of the ground state doublet
Jx=EVc\jx*EVc;
Jy=EVc\jy*EVc;
%Finding eta=|<Gamma2|Jx|up>|^2=|<Gamma2|Jx|down>|^2 for use in perturbation
%theory result of effective longitudinal field:
eta=Jx(2,3)*Jx(3,2);

```

G.2 Including HF Structure (Extending to Electro-Nuclear States)

The following code designated *Inclusion_of_HF.m* is a direct continuation of the code in appendix G.1 and extends the Hilbert space of the eigenstates produced in that code to include the HF structure.

Standard Matlab diagonalization process (not iterative) is applied to find the new eigenstates.

The code also calculates the corrections to 2nd order perturbation theory stemming from

coupling to excited electronic levels higher than Γ_2 , from the HF structure and from the dipolar interaction.

```
%% %           ——— Defining Basic HF Operators ———
I=7/2;
VECiz=(-I:I);
Iz=diag(VECiz);

VECiplusminus=zeros(1,(2*I+1)-1);
for t=-I:I-1
    VECiplusminus(t+I+1)=sqrt(I*(I+1)-t*(t+1));
end

Iplus=diag(VECiplusminus,-1);
Iminus=diag(VECiplusminus,1);

AJ=0.039; %Kelvin

%% %           ——— Incorporating HF ———

%This joins the electron and nuclear angular momentum spaces using outer product
jz=kron(jz,eye(2*I+1));
Iz=kron(eye(2*J+1),Iz);
jplus=kron(jplus,eye(2*I+1));
jminus=kron(jminus,eye(2*I+1));
Iplus=kron(eye(2*J+1),Iplus);
Iminus=kron(eye(2*J+1),Iminus);
Vc=kron(Vc,eye(2*I+1));
%EVc is used to change basis to that of the eigenstates of the Crystal Field
EVc=kron(EVc,eye(2*I+1));

%Building the jx matrix from the j minus and jplus matrices
jx=(jplus+jminus)/2;
%Building the jy matrix from the j minus and jplus matrices
jy=(jplus-jminus)/(2i);

HF=AJ*((jplus*Iminus+jminus*Iplus)/2+jz*Iz);

%% %—— Calculating corrections to the energy difference found in 2nd order ——
%—— perturbation theory (corrections are still in 2nd order) ——

%changing basis (only for this section of the code)
Jz=EVc\jz*EVc;
Jx=EVc\jx*EVc;
Jy=EVc\jy*EVc;

%the file "positions_of_neighbors_sorted_by_distance.mat" stores various parameters
%relevant to the different pairs with ions at various relative positions.
```

```

load positions_of_neighbors_sorted_by_distance position

%the neighbor in question (the first 4 entries are n.n. pairs the next 4 entries
%are 2nd n.n. pairs and so on. see table in first appendix of thesis as an
%example)
neighbor=1;

%position(neighbor,10) gives 2 times the strength of the zz dipolar interaction
%at Bx=0. The difference in energy due to the zz dipolar term between and upup
%state and a Gamma2up state should be half that.
Energy_dipolar=position(neighbor,10);

Energy=diag(EVc\Vc*EVc)+diag(HF);
%changing the energy levels according to the Hf structure. here we consider only
%the contribution of diagonal part of the HF interaction (AJ*jz*Iz)

%      ——— Finding Theta=eta/Omega_0+eta_4/(3Omega_0)+... ———
%eta=|<Gamma2| Jx |up>|^2
%eta_u=|<u| Jx |up>|^2=|<u| Jx |down>|^2 (u being an excited level)
Theta=0;
for t=3:17
    Theta=Theta+Jx((1-1)*8+2,(t-1)*8+2)*Jx((t-1)*8+2,(1-1)*8+2)/...
        (Energy((t-1)*8+2)-(Energy((1-1)*8+2)+Energy_dipolar/2));
    %The energy of the up and down states should be changed by "Energy_dipolar/2"
    %since in fact it represents the energy of upup and downdown states , whereas
    %the energy of the excited states represents the energy of states such as
    %Gamma2up which lack the longitudinal dipolar contribution to the energy.
end

%"position(neighbor,12)" give the coefficient Vzx of the dipolar interaction.
slope_Bz_eff_2nd_order=position(neighbor,12)*4*abs(Theta);

%"position(neighbor,13)" give the coefficient Vxx of the dipolar interaction.
slope_Bz_eff_3rd_order_numerator=5.62^2*10*position(neighbor,12)*...
    position(neighbor,13);

%I used Omega_0=10 as the energy difference without taking into account longitudinal
%dipolar and longitudinal HF interactions as a first approximation for the 3rd
%order terms
slope_Bz_eff_3rd_order=slope_Bz_eff_3rd_order_numerator/(10)^2;

slope_Bz_eff_both_orders=slope_Bz_eff_2nd_order+slope_Bz_eff_3rd_order;
slope_energy_split_both_orders=slope_Bz_eff_both_orders*4*(5/4)*0.6717*5.51;

%this is for when I want to find 2nd order only

```



```

slope_energy_split_2nd_order=slope_Bz_eff_2nd_order*4*(5/4)*0.6717*5.51;
%this is for when I want to find 3rd order only
slope_energy_split_3rd_order=slope_Bz_eff_3rd_order*4*(5/4)*0.6717*5.51;

%%                                — Diagonalization —

H=Vc+HF;
[EV,ES]=eig(H);
%notice that this is still in the old basis. To change to the new basis (eigenstates
%of the Crystal Field whose Hilbert space is extended to include the HF
%structure) the following commands have to be executed "EV=EVC\EV". also Jx, Jy
%and Jz should be used instead of jx, jy jz.

```

G.3 The Full 2 Ions Model

The following code designated *Sparse_Diag_for_HPC.m* is a direct continuation of the code in appendix G.2 and extends the Hilbert space of the eigenstates produced there to include two ions. It also incorporates the dipolar interaction between the ions and a Zeeman term (both longitudinal and transverse components)

Sparse Matrices are used to conserve memory and accordingly an iterative diagonalization method is used to produce the eigenstates and eigenvalues (see appendix C for details).

In practice many versions of this code were run on the BGU High Performance Cluster (HPC) each for a different B^x value (or a different B^z value). A master code calls this code to run each time with the different parameters. For brevity the master code is not shown here and instead the relevant parameters are manually defined.

```

%% %An example of the parameters defined by the master code:

%Maximum and minimum transverse field values
Bx_max=3;    %Tesla
Bx_min=0.01; %Tesla
%Transverse field step size
step=0.01;   %Tesla

%interval is the amount of Bx values (in steps of size 'step') used in each run of
%this code.
interval=2;

%The results in the thesis correspond to zero longitudinal field, but the code can
%take into account non-zero fields as well.
Bz=0; %Tesla

%VEChum determines the number of eigenstates and eigenvalues that the iterative
%process finds. For most purposes it is sufficient to find the 576
%[(3 X 8) X (3 X 8)] lowest eigenstates which correspond (at zero field) to
%each ion being in one of the 3 lowest electronic states.

```

```

VEChum=576;

%VECdim determines how many components will be saved from each eigenstate. When
%interested in levels which at low fields correspond to the 2 (or 3) lowest
%electronic levels and at low to moderate fields (0 to 2T) where these levels
%incorporate very little components of the 3rd (or 4th) and above electronic
%levels, it is enough to save the components corresponding to the 4th electronic
%levels and below (1024 components = [(4 X 8) X (4 X 8)] )
VECdim=1024 ;

f_ind=1; %f_ind is a parameter which tells this code which Bx values to consider out
%of the entire range defined in the master code. In this example, f_ind=1 means
%that this code uses the lowest 2 (interval=2) Bx values i.e. Bx=0.01 and
%Bx=0.02. The expression f_ind=2 would take the next 2 values and so on

%% %Defining Basic Parameters for dipolar interaction and Zeeman effect

%Lande g factor (Unitless)
gL=5/4;
%Bohr Magneton (Kelvein/Tesla)
uB=0.6717;
%Vacuum Permeability (Tesla*meter/Ampere)
u0=4*pi*10^(-7);
%Boltzmann constant (Joule/Kelvin)
Kb=1.3806504*10^(-23);

%% %Defining Relative Positions of Ions

%Unit cell measurements:
a=5.175 *10^(-10); %Meter
c=10.75 *10^(-10); %Meter

%The relative position vector between the two ions:
r=[a/2 0 c/4];

%% %Incorporating Dipolar interactions

%Switching to storage of matrices in sparse format (only non-zero elements are saved)
%All matrices in sparse format are denoted by an 's' prefix
sjx=sparse(jx);
sjy=sparse(jy);
sjz=sparse(jz);

%Extending the Hilbert space to include two ions using an outer product
sjx1=kron(sjx ,speye((2*J+1)*(2*I+1)));
sjy1=kron(sjy ,speye((2*J+1)*(2*I+1)));
sjz1=kron(sjz ,speye((2*J+1)*(2*I+1)));

```

```

sjx2=kron(speye((2*J+1)*(2*I+1)),sjx);
sjy2=kron(speye((2*J+1)*(2*I+1)),sjy);
sjz2=kron(speye((2*J+1)*(2*I+1)),sjz);

%Defining the dipoar interaction
U=gL^2*uB^2*u0*Kb/(4*pi);
Vint=(norm(r))^2*eye(3);
Vint=Vint-3*(r)'*r;
Vint=Vint*U/(norm(r))^5;

sHint= Vint(1,1)*sjx1* sjx2 +Vint(1,2)*sjx1*sjy2 +Vint(1,3)*sjx1*sjz2 ;
sHint=sHint+ Vint(2,1)*sjy1* sjx2 +Vint(2,2)*sjy1*sjy2 +Vint(2,3)*sjy1*sjz2 ;
sHint=sHint+ Vint(3,1)*sjz1* sjx2 +Vint(3,2)*sjz1*sjy2 +Vint(3,3)*sjz1*sjz2 ;

%% %Expanding the basis change matrix for two spins
sEVc=sparse(EVc);
sEVc1=kron(sEVc,speye((2*J+1)*(2*I+1)));
sEVc2=kron(speye((2*J+1)*(2*I+1)),sEVc);

%% %Allocating memory to arrays

%defining a 3D array that will store several eigenstates matrices for different Bx
%values
full_EV=zeros(VECDim,VECnum,interval);
%defining a 2D array that will store several eigenstates vectors (!!!) for different
%Bx values
full_ES=zeros(interval,VECnum);

%Save_ind keeps the indices of the components (of the eigenstates) we wish to keep
for t=1:sqrt(VECDim);
    Save_ind((t-1)*sqrt(VECDim)+1:t*sqrt(VECDim))=(t-1)*136+1:(t-1)*136+sqrt(VECDim);
end

%% %This is the actual diagonalization loop

%for the predetermined number of Bx values:
for f=1:1:interval

    %Bx=minimum + proportional to which file is used + proportional to index
    %within file
    Bx=Bx_min + (f_ind-1)*interval*step + (f-1)*step;

    Hziman=-gL*uB*(Bz*jz+Bx*jx);
    H=Vc+HF+Hziman;

    %switching to storage in sparse format (sHint is already in sparse format)
    sH=sparse(H);

```

```

sH=kron(sH,speye((2*J+1)*(2*I+1)))+kron(speye((2*J+1)*(2*I+1)),sH)+sHint;

%'eigs' is the iterative diagonalization command
%note that 'eigs' (just like 'eig') returns the eigenstates in a matrix, not a
%vector
[sEV,sES]=eigs(sH,VECnum);

%changing basis to that of the Crystal Field eigenstates (extended to include
%HF and two ions)
sEV=sEVc1\sEV;
sEV=sEVc2\sEV;

%keeping only the desired eigenstates components
%also, placing the eigenstates matrix in the 3D array defined above
full_EV(:, :, f)=sEV(Save_ind, :);
%storing the eigenstates matrix (which is diagonal in any case) in vector form
%also, placing this eigenstate vector in the 2D array defined above
full_ES(f, :)=(diag(sES))';

end

%Permuting the dimensions of the 3D Eigenstates array to make it compatible to the
%Eigenvalue array:
full_EV=permute(full_EV,[3 2 1]);

%% Sorting Eigenstates

%The 'eigs' command is supposed to return the eigenvalues and eigenstates in order
%of ascending eigenvalues. This ordering is not always perfect when eigenstates
%are almost degenerate which is why a separate sorting is needed

%This checks whether the eigenenergies are given in the correct order (for each
%field value)
[full_ES_sort, ind_sort]=sort((full_ES)');
ind_sort=ind_sort';

%This sorts the states according to ascending order of the corresponding energies
%(for each field value)
full_ES=full_ES_sort';
for t=1:interval
    full_EV(t, :, :)=full_EV(t, ind_sort(t, :), :);
end

%% %%For each such file the information is saved to be later recalled for analysis

```

G.4 Tracking Diabatic States Through Crossings

G.4.1 Review of Method

This appendix presents the method used for tracking diabatic states for increasing B^x and through level crossings. By tracking a diabatic state we mean affiliating an eigenstate (for each B^x value) which is the most similar to the diabatic state (for the same B^x value). Away from avoided level crossings, the tracking is simple since the eigenstates and diabatic states are equivalent. Near avoided level crossings the process becomes problematic since there the diabatic states are necessarily a mix of eigenstates.

The main idea behind the tracking method relies on comparing the eigenstates for each B^x values to a reference eigenstate using a dot product.

The code used for tracking is by no means perfect and in fact fails whenever the crossing width (and therefore the coupling between levels at avoided level crossings) is too large. However for the purpose of this study it is enough, as it can correctly track the two diabatic states $|\uparrow - \frac{7}{2} \uparrow - \frac{7}{2} \rangle$ and $|\downarrow \frac{7}{2} \downarrow \frac{7}{2} \rangle$ up to transverse fields of at least $B^x = 1.2[T]$. The results of the tracking were manually verified wherever there was doubt as to their accuracy.

G.4.2 Code

The following code designated *Diabatic_States_Tracking.m* keeps track of the affiliation of eigenstates with diabatic states as B^x is increased. It does so for 2 diabatic states whose most dominant components are specified (e.g diabatic states starting as $|\uparrow - \frac{7}{2} \uparrow - \frac{7}{2} \rangle$ and $|\downarrow \frac{7}{2} \downarrow \frac{7}{2} \rangle$).

The code loads the data from each file separately and only after tracking the states for the B^x values stored in the current file, moves on to the next file (files are created by the code in appendix G.3). The entire data set is not loaded simultaneously due to memory limit issues.

The code also computes the energy difference between the tracked states, the $\langle J^z \rangle$ value for these states and the random field for the two ions (assuming the tracked states correspond to $|\uparrow\uparrow\rangle$ and $|\downarrow\downarrow\rangle$ states).

The following is a short review of the code for increased clarity:

The code assumes that the tracking starts at a low enough initial B^x value (B_{min}^x) so that the appropriate eigenstate at B_{min}^x can be trivially affiliated to the diabatic state we wish to track. This is done by looking for the eigenstate which has the largest component in the direction (at zero field) of the tracked diabatic state (e.g. looking for the eigenstate with the greatest $|\uparrow - \frac{7}{2} \uparrow - \frac{7}{2} \rangle$ component).

Another assumption is that the tracking starts well away from any level crossings so that the eigenstate affiliated to the tracked diabatic state at B_{min}^x is in fact equivalent to the diabatic state. This will allow us to use this eigenstate as a reference for comparing eigenstates of higher B^x values to the tracked diabatic state. For the minimal value $B_{min}^x = 0.01[T]$ and the field step size $B_{step}^x = 0.01[T]$ used in this study, this is a good assumption as the first crossing for n.n. pairs is at $B^x = 0.26[T]$ and at even higher field values for farther pairs.

From this point on the tracking works by increasing the B^x value, and for each step comparing the dot product of each of the eigenstates with the reference eigenstate. The eigenstate which

produces the greatest dot product is considered as the continuation of the tracked diabatic state.

The reference eigenstate has to be updated occasionally since the diabatic states change with B^x . However we have to take care not to choose a reference eigenstate too near to an avoided level crossing. This is because we want to choose as a reference only eigenstates which are practically equivalent to the appropriate diabatic state. This is currently the weak point of the code, as it does not correctly identify level crossings which are relatively wide in B^x . As the coupling between states (and therefore the width of the crossings) increase with the applied transverse field B^x [17] (see fig. 4 there), we are limited to accurate tracking in the range $0 < B^x < 1.2[T]$.

```
%% %Basic Parameters
```

```
%For Brevity it is assumed that all the parameters defined in previous codes
%(such as Bx_max, Bx_min, step and so on) are already defined.
```

```
Resolution=1; %Resolution is used to control how small are the steps in Bx that
    %are actually used. When a wide range of Bx values is desired (say 0 to 10
    %Tesla), and memory is short, a Resolution values larger than 1 can be chosen
    %which means that not all Bx values in the data set will be used. For
    %'Resolution=2' 1 out of every 2 stored Bx values will be used and so on.
    %Legitimate values for 'Resolution': 1, 2, 5 or 10.
```

```
%'M' is the number of Bx values considered.
M=double(int16((Bx_max-Bx_min)/step)+1)/Resolution;
```

```
%% %Determining State Indices
```

```
%Numbering of states in  $136^2=18496$  dimensions (vector components)
```

```
%First state to look for (in this case 1097 corresponds to the  $|\text{up}-7/2 \text{ up}-7/2\rangle$ 
%state
State_ind_1=1097;
%Second state to look for (960 corresponds to the  $|\text{down}7/2 \text{ down}7/2\rangle$  state
State_ind_2=960;
```

```
%Numbering of states in  $(3 \times 8)^2=576$  dimensions (instead of 18496)
State_ind(1,1)=double(int16(State_ind_1/136)*sqrt(VECDim)+ ...
    mod(int16(State_ind_1),136));
State_ind(2,1)=double(int16(State_ind_2/136)*sqrt(VECDim)+ ...
    mod(int16(State_ind_2),136));
```

```
%% %Tracking 2 states through level crossings
```

```
%'lvl_ind' stores the indices of the 2 levels tracked (e.g. 1 if the tracked
    %level has the lowest energy, 2 if it's the second lowest and so on) for all
    %relevant Bx values.
lvl_ind=zeros(2,M);
```

```

%'Partial_EV' stores a subset of the eigenstates containing only the 2 states
%(per Bx value) affiliated with the tracked diabatic states.
Partial_EV=zeros(M,2,VECdim);

%'previous_EV' stores the 2 eigenstates which were found as corresponding to the
%tracked diabatic states for the previous Bx value. This is used to compare
%sequential (in Bx) 'tracked' eigenstates to see if a level crossing has been
%reached
previous_EV=zeros(2,VECdim);

%'immediate_overlap' stores the overlap (dot product) of every two sequential
%eigenstates tracked (for the same diabatic state). This is used to see if a
%level crossing has been reached
immediate_overlap=zeros(2,M);

%'prime_overlap' stores the overlap (dot product) of the eigenstate affiliated
%with (chosen as the most similar to) the tracked diabatic state with the
%reference eigenstate.
prime_overlap=zeros(2,M);

%For every data file
for t=1:M/interval

    %load the eigenstates stored in this data file. The data is stored in files
    %such as "shpc_sorted_f_ind_1.mat" where the number at the end is an index
    %to the order of the files (from low Bx to high).
    temp_EV=load(['shpc_sorted_f_ind_' num2str(((Bx_min-Bx_min)/step)/interval+t)...
        '.mat'], 'full_EV');
    temp_EV=temp_EV.full_EV;

    %Go over Bx values in this data file in steps of "step*Resolution":
    for q=Resolution:Resolution:interval

        %'field_ind' is the index of the current Bx value among all the Bx values
        %used.
        field_ind=((t-1)*interval+q)/Resolution;

        %'flag' is 1 if everything is ok, and 0 if there's a problem (no
        %eigenstate matches the diabatic state)
        flag=[0 0];

        %For the first Bx value considered: (This part defines the initial
        %affiliation between eigenstates and diabatic states)
        if field_ind==1

            %go over all the 'VEChum' eigenstates

```

```

for k=1:VECnum

    %find the eigenstate which has largest component (squared)
    %corresponding to the (first) tracked diabatic state. Make
    %sure this state is similar enough to the diabatic state
    %(component^2 > 0.3) (i.e. find the eigenstate most closely
    %resembling the first tracked diabatic state for this initial
    %Bx value)
    if ((abs(temp_EV(q,k,State_ind(1,1))))^2>0.3) && ...
        ((abs(temp_EV(q,k,State_ind(1,1))))^2> ...
        prime_overlap(1,field_ind))

        %for "field_ind=1", 'Prime_overlap' gives the magnitude (squared)
        %of the component of the (first) tracked diabatic state in the
        %current (k^th) eigenstate being investigated. (at the end of
        %the "for k=1:VECnum" loop this will correspond to the eigenstate
        %with the greatest such component)
        prime_overlap(1,field_ind)=(abs(temp_EV(q,k,State_ind(1,1))))^2;

        %set the level index of the (first) diabatic state according to
        %the appropriate eigenstate for the initial Bx
        lvl_ind(1,field_ind)=k;

        flag(1)=1;          %no error
    end

    %the same as the above "if" only for the second tracked diabatic
    %state
    if ((abs(temp_EV(q,k,State_ind(2,1))))^2>0.3) && ...
        ((abs(temp_EV(q,k,State_ind(2,1))))^2>...
        prime_overlap(2,field_ind))
        prime_overlap(2,field_ind)=(abs(temp_EV(q,k,State_ind(2,1))))^2;
        lvl_ind(2,field_ind)=k;
        flag(2)=1;
    end
end

%define the reference eigenstate for the (first) tracked diabatic state
%as the eigenstate of the initial Bx value
prime_EV(1,:)=squeeze(temp_EV(1,lvl_ind(1,1),:));

%same as the line above only for the second tracked state
prime_EV(2,:)=squeeze(temp_EV(1,lvl_ind(2,1),:));

%if an appropriate eigenstate was not found, stop running loop.
if (~(flag(1))) || (~(flag(2)))
    Array_size=field_ind-1;
    break;
end

```



```

end

%for any other Bx value (not the initial one)
else

%—— Looking for the eigenstate with the greatest overlap (dot product) to ——
%—— the reference eigenstate "Prime_EV" ——

%for each tracked state:
for p=1:2

    %go over the different eigenstates (There's an assumption here that
    %the correct level is close (up to 8 levels away) to the level
    %used in the previous Bx value)
    for k=max(1,lv1_ind(p,field_ind-1)-8): ...
        min(VECnum ,lv1_ind(p,field_ind-1)+8)

        %if the magnitude of the dot product is greater than any of the
        %previous ones (for eigenstates with lower energy):
        if abs(dot(squeeze(temp_EV(q,k,:)) , prime_EV(p,:))) > ...
            prime_overlap(p,field_ind)

            %"prime_overlap" gives the overlap (dot product) between the
            %current (k^th) eigenstate and the reference eigenstate
            prime_overlap(p,field_ind)=...
                abs(dot(squeeze(temp_EV(q,k,:)) , prime_EV(p,:)));

            %"immediate_overlap" gives the overlap (dot product) between
            %the current eigenstate and the eigenstate chosen for the
            %tracked diabatic state in the most recent Bx value used
            immediate_overlap(p,field_ind)=...
                abs(dot(squeeze(temp_EV(q,k,:)) , previous_EV(p,:)));

            lv1_ind(p,field_ind)=k;
            flag(p)=1;    %no error
        end
    end

    %if an appropriate eigenstate was not found, stop running
    %loop (for p=...)
    if ~flag(p)
        Array_size=field_ind-1;
        break
    end
end

%if an appropriate eigenstate was not found, stop running
%loop (for q=...)

```

```

    if (~flag(1)) || (~flag(2))
        break
    end
end

%—— Updating reference eigenstates ——

%for each tracked state:
for p=1:2
    %save the relevant eigenstate found for the current Bx value
    Partial_EV(field_ind,p,:)=temp_EV(q,lvl_ind(p,field_ind),:);

    %temporarily save this same eigenstate to be compared to the
    %eigenstates of the next Bx value
    previous_EV(p,:)=squeeze(Partial_EV(field_ind,p,:));

    %the reference eigenstate cannot be updated within the first 8 Bx
    %values. This is because 8 Bx values preceding the current
    %Bx value are used to check that the current Bx value is not
    %too near to a level crossing.
    if field_ind>8

        %if A) the overlap of the currently tracked 'eigenstate' with
        %the reference eigenstate is smaller than 0.9 (this could
        %be either since the diabatic state has changed too much
        %since the reference eigenstate was last determined or
        %because we are near an avoided level crossing. The next
        %conditions try to rule this out)).
        % B)The eigenstates did not change too much in the previous 8
        %Bx values (which would happen if we were near a level
        %crossing). The way this change in eigenstates is tested
        %is by making sure the "immediate_overlap" did not change
        %too much:
            %1) standard deviation is small
            %2) the "immediate_overlap" for this Bx value is not
            %much larger or smaller than the mean of the
            %"immediate_overlap" for previous Bx value (at most 2
            %standard diviations above or below the mean)
        if (prime_overlap(p,field_ind)<0.9) && ...
            ( ( (2*std(immediate_overlap(p,(field_ind-8): ...
                (field_ind-1)))<0.05) && ...
                (immediate_overlap(p,field_ind)< ...
                    (mean(immediate_overlap(p,(field_ind-8):(field_ind-1))) ...
                        +2*std(immediate_overlap(p,(field_ind-8):(field_ind-1)))))) ...
                    && (immediate_overlap(p,field_ind)> ...
                        (mean(immediate_overlap(p,(field_ind-8):(field_ind-1))) ...
                            -2*std(immediate_overlap(p,(field_ind-8):(field_ind-1)))))))

```

```

                                %Under these conditions a new reference eigenstate is defined
                                prime_EV(p,:)=Partial_EV(field_ind ,p,:);
                                end
                                end
                                end
                                end

                                %if an appropriate eigenstate was not found, stop running loop (for t=...)
                                if (~flag(1)) || (~flag(2))
                                    break
                                end
                                end
                                end

                                %% %Energy difference , <Sz> and random field

                                %shrinking the jz matrix to 1024X1024 (i.e. saving only matrix entries relevant
                                %to the VECdim components we save for each eigenstate)
                                Sjz1=Sjz1(Save_ind ,Save_ind);
                                Sjz2=Sjz2(Save_ind ,Save_ind);

                                %Finding the energy difference between the tracked states
                                energy_diff=zeros(1,M);
                                for t=1:M
                                    energy_diff(t)=full_ES(t,lv1_ind(2,t))-full_ES(t,lv1_ind(1,t));
                                end

                                %Finding <jz> for the tracked states (for both ions)
                                jz_expectancy=zeros(2,2,M);
                                for t=1:M
                                    jz_expectancy(1,1,t)=(squeeze(Partial_EV(t,1,:)))'*Sjz1*squeeze(Partial_EV(t,1,:));
                                    jz_expectancy(1,2,t)=(squeeze(Partial_EV(t,1,:)))'*Sjz2*squeeze(Partial_EV(t,1,:));
                                    jz_expectancy(2,1,t)=(squeeze(Partial_EV(t,2,:)))'*Sjz1*squeeze(Partial_EV(t,2,:));
                                    jz_expectancy(2,2,t)=(squeeze(Partial_EV(t,2,:)))'*Sjz2*squeeze(Partial_EV(t,2,:));
                                end

                                %I assume here that the first state is the appropriate UPUP state and the sceond
                                %state is the appropriate DOWNDOWN state!!!!!!
                                random_field=energy_diff./transpose(squeeze((uB*gL*(jz_expectancy(1,1,:)+ ...
                                    jz_expectancy(1,2,:)-jz_expectancy(2,1,:)-jz_expectancy(2,2,:)))));

                                %% %Plots

                                %Defining the X axis
                                F=1:1:M;
                                X=Bx_min+step*(Resolution-1)+(F-1)*step*Resolution;

                                %Energy levels compared to the energy of the mean of the two levels tracked

```

```

min_lvl=1;
max_lvl=32;
figure
ax1=gca;
ylabel('Energy_{E_n-E_{min}}');
xlabel('Bx');
set(ax1,'XColor','k','YColor','k','Xlim',[Bx_min-step Bx_max+step]);
colorvalues=['b' 'r' 'g' 'm' 'y' 'k' 'c'];
colorvalues(8:576)='c';
hold on
for p=min_lvl:max_lvl
    for t=1:M
        line(X(t),full_ES(t,p)-(full_ES(t,lvl_ind(2,t))+full_ES(t,lvl_ind(1,t)))/2,...
            'MarkerFaceColor',colorvalues(idivide(int16(p-1),7)+1),'Color',...
            colorvalues(mod(p-1,7)+1),'MarkerSize',6,'LineStyle','none','Marker',...
            'd','Parent',ax1);
    end
end

%Plotting the signed value of <Sz> for both states
figure
hold on
plot(X,squeeze(jz_expectancy(1,1,:)),'b','LineWidth',4);
plot(X,squeeze(jz_expectancy(1,2,:)),'b—','LineWidth',4);
plot(X,squeeze(jz_expectancy(2,1,:)),'r','LineWidth',4);
plot(X,squeeze(jz_expectancy(2,2,:)),'r—','LineWidth',4);
ylabel('<J_z>','FontSize',18);
xlabel('B^x_{[T]}','FontSize',18);
set(gca,'FontSize',14);

% plotting energy difference
figure
plot(X,energy_diff,'LineWidth',4);
ylabel('\Delta_{E_{[K]}}','FontSize',18);
xlabel('B^x_{[T]}','FontSize',18);
set(gca,'FontSize',14);

%plotting random field — absolute value
figure
plot(X,abs(random_field),'LineWidth',4);
ylabel('B^z_{eff}_{[T]}','FontSize',18);
xlabel('B^x_{[T]}','FontSize',18);
set(gca,'FontSize',14);

```

G.5 Shifted Peaks Positions

The following code designated *Shifted_Peaks_Locations.m* produces a plot of the positions of the 4 most significantly shifted peaks (blue dots) with a slider control for the transverse field parameter (see Figs. 4.2 and E.1). Green squares represent the minima of valleys between unshifted peaks (where the shifted eaks are expected to be the most visible). The lines representing the unshifted peaks are for illustration only and do not follow the actual functional form of such peaks.

This code uses the "Manipulate: Interactive Parametrized Plotting" package not built-in in Matlab which can be downloaded from the "Matlab Central" website [43].

```
%Coefficients for the effective fields of the relevant pairs. These coefficients
%are based on a linear fit to the random field data for 0.01<Bx<0.8
%1st n.n.
coeff(1,1)=0.0442; %slope
coeff(2,1)=-1.6809*10^(-4); %effective field at (Bx=0)
%3rd n.n - 'first' orientation.
coeff(1,2)=0.0063; %slope
coeff(2,2)=-7.0682*10^(-5); %effective field at (Bx=0)
%3rd n.n - 'second' orientation.
coeff(1,3)=0.0032; %slope
coeff(2,3)=-2.8418*10^(-5); %effective field at (Bx=0)
%4th n.n.
coeff(1,4)=0.0056; %slope
coeff(2,4)=-4.2954*10^(-5); %effective field at (Bx=0)

%'n' determines how many unshifted peaks are presented (n single-flip peaks on
%either side of the Bx=0 peak)
n=2;

%Bz_n is the distance in Bz between a single-flip peak and a co-tunnelling peak
Bz_n=0.0115; %Tesla

%limit of the plot in Bz
Bz_lim=(n*2+(3/4))*Bz_n;

%Bz_step is the resolution for the points on the plot (in Bz)
Bz_step=0.00005;

%finding the size of the array
Bz_size=size(-Bz_lim:Bz_step:Bz_lim);
s=Bz_size(2);

% — plotting the expected positions of the shifted susceptibility peaks —
% — blue dots —

% a blue dot appears whenever the difference between Bz (=-Bz_lim:Bz_step:Bz_lim)
```

```

    %and the position of a shifted peak is smaller than 'res' (the position of a
    %shifted peak is defined as any of the positions of unshifted peaks
    %plus/minus the effective field of any pair)
res=0.00005;
manipulate( { @(Bz,param) ( +( (any(abs(repmat(Bz,4*n+1,1)- ...
    repmat((-n*2*Bz_n:Bz_n:n*2*Bz_n)',1,s)- ...
    ones(4*n+1,s)*(coeff(1,1)*param(1)+coeff(2,1))) <= res))
...
    (any(abs(repmat(Bz,4*n+1,1)-repmat((-n*2*Bz_n:Bz_n:n*2*Bz_n)',1,s)+ ...
    ones(4*n+1,s)*(coeff(1,1)*param(1)+coeff(2,1))) <= res))
...
    (any(abs(repmat(Bz,4*n+1,1)-repmat((-n*2*Bz_n:Bz_n:n*2*Bz_n)',1,s)- ...
    ones(4*n+1,s)*(coeff(1,2)*param(1)+coeff(2,2))) <= res))
...
    (any(abs(repmat(Bz,4*n+1,1)-repmat((-n*2*Bz_n:Bz_n:n*2*Bz_n)',1,s)+ ...
    ones(4*n+1,s)*(coeff(1,2)*param(1)+coeff(2,2))) <= res))
...
    (any(abs(repmat(Bz,4*n+1,1)-repmat((-n*2*Bz_n:Bz_n:n*2*Bz_n)',1,s)- ...
    ones(4*n+1,s)*(coeff(1,3)*param(1)+coeff(2,3))) <= res))
...
    (any(abs(repmat(Bz,4*n+1,1)-repmat((-n*2*Bz_n:Bz_n:n*2*Bz_n)',1,s)+ ...
    ones(4*n+1,s)*(coeff(1,3)*param(1)+coeff(2,3))) <= res))
...
    (any(abs(repmat(Bz,4*n+1,1)-repmat((-n*2*Bz_n:Bz_n:n*2*Bz_n)',1,s)- ...
    ones(4*n+1,s)*(coeff(1,4)*param(1)+coeff(2,4))) <= res))
...
    (any(abs(repmat(Bz,4*n+1,1)-repmat((-n*2*Bz_n:Bz_n:n*2*Bz_n)',1,s)+ ...
    ones(4*n+1,s)*(coeff(1,4)*param(1)+coeff(2,4))) <= res)) -0.9), ...
[-Bz_lim:Bz_step:Bz_lim],[0]},{}, {1,'Bx',0 1.2})
set(findobj('Type','line'),'LineStyle','none','Marker','.', 'MarkerSize',10)

%           — plotting valley minima positions: —

%valley minima positions (optimal place to put a shifted peak for visibility):
Z_optimal1=-(n*2-3/4)*Bz_n:2*Bz_n:(n*2-3/4)*Bz_n;
Z_optimal2=-(n*2-5/4)*Bz_n:2*Bz_n:(n*2-3/4)*Bz_n;
si=size(Z_optimal2);
si=si(2);
Y_optimal=1.1*ones(si,1);

%plot — marking valley minima with green squares
hold on
plot(Z_optimal1,Y_optimal-1,'gs','MarkerSize',10)
plot(Z_optimal2,Y_optimal-1,'gs','MarkerSize',10)
xlabel('Bz [T]', 'FontSize',18);
ylabel('Susceptibility', 'FontSize',18);
set(gca, 'YTick', [], 'FontSize',14);

```

```

%      — plotting an illustration of the unshifted peaks — blue lines —

%single-flip peak positions
Z_single=-n*2*Bz_n:2*Bz_n:n*2*Bz_n;

%co-tunnelling peak positions
Z_co=-(n*2-1)*Bz_n:2*Bz_n:(n*2-1)*Bz_n;

Y_single=1.1*ones(n*2+1,1);
Y_co=1.1*ones(n*2);

%Defining the illustrated peaks as decaying exponentially with coefficients such
%that minimum between a single-flip peak and a co-tunnelling peak would fall
%where the minima is already marked
A=(3/2)*(1/Bz_n)*log(100);
B=(4)*(1/Bz_n)*log(10);
Z=Bz_lim:Bz_step:Bz_lim;
single_peak=zeros(2*n+1,s);
co_peak=zeros(2*n,s);
all_peaks=zeros(1,s);
for k=-n:n
    single_peak(k+n+1,:)=exp(-abs(Z-k*2*Bz_n)*A);
    all_peaks=all_peaks+single_peak(k+n+1,:);
end
for k=1:n
    co_peak(k,:)=0.1*exp(-abs(Z-(2*k-1)*Bz_n)*B);
    co_peak(k+n,:)=0.1*exp(-abs(Z+(2*k-1)*Bz_n)*B);
    all_peaks=all_peaks+co_peak(k,:)+co_peak(k+n,:);
end

plot(Z,all_peaks,'LineWidth',2)
ylim([0 1])

```

G.6 Finding Energy Gaps in Avoided Level Crossings

Some of the on-resonance energy gaps (energy gaps at avoided level crossings) were found in order to predict Landau-Zener behaviour of crossing such a resonance. The energy gaps were found using a code almost identical to the one in appendix G.3, the only difference being that we changed B^z and set a constant B^x . We repeatedly (manually) ran the code for a narrowing range of B^z values around a desired crossing with an increasing resolution of the B^z values (smaller B^z step size). At each step the energy levels plot was observed until either the avoided level was clearly seen (the energy levels formed clear non-intersecting curves), or the Matlab precision limit was reached (we got a very messy plot where no curve could be identified)

As the magnitude of the on-resonance energy gaps is exponentially proportional to the applied transverse field B^x [17] (see fig. 4 there), at low fields (under around $0.6T$), these gaps are below the Matlab precision limit. Thus we could only find such gaps and predict Landau-Zener behaviour for fields above this value. However even for greater transverse fields some of the gaps are very close to the Matlab precision limit making them hard to evaluate.

A good example is the the 'first' of the $n = \frac{1}{2}$ crossing (the one at a more negative B^z value out of the two) at $B^x = 0.6[T]$ (see Fig. G.1 and G.2).

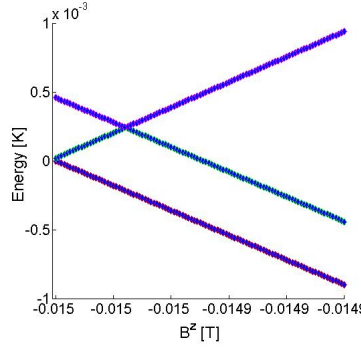


Figure G.1: Energy levels for the $n = \frac{1}{2}$ crossings for *n.n.* pairs under applied transverse field $B^x = 0.6T$. The analysis here is for the 'first' of these at more negative B^z

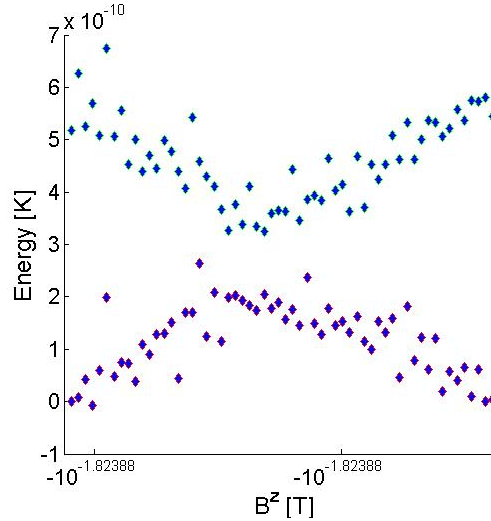


Figure G.2: Zoom in on energy levels for the 'first' of the $n = \frac{1}{2}$ crossings for *n.n.* pairs under applied transverse field $B^x = 0.6T$. The effects of the Matlab precision limit are evident

To find these energy gaps accurately we used fitting for the energy difference with applied *longitudinal* field, and extrapolated the minimum of the fitted curve. We used the Matlab Curve

Fitting tool with a custom fit to the expected functional form of the energy difference:

$$\Delta E(B^z) = (\Delta E_{min}^2 + (\alpha * (B^z - B_{resonance}^z))^2)^{\frac{1}{2}} \quad (\text{G.6.1})$$

We chose 51 points around the expected minimum and used the 'Center and scale' option with the 'Robust' option off.

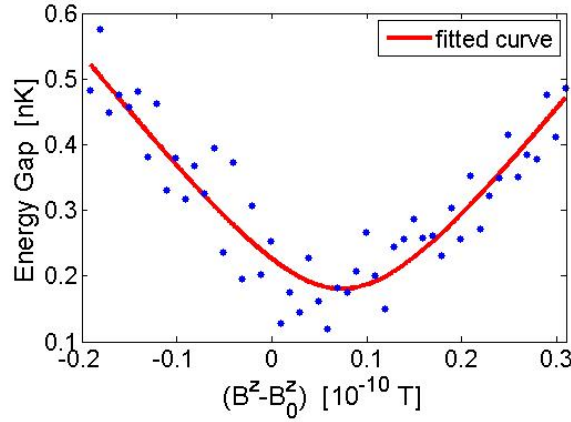


Figure G.3: Fit to gap between 2nd and 3rd energy levels (first of $n = \frac{1}{2}$ crossing) for n.n. pairs under applied transverse field $B^x = 0.6T$. Blue dots mark the data points used for the fit. The fit itself noted by a red line. $B_0^z = -0.015001018148902$ was used to roughly center the x axis data points of the plot (B^z values) around zero for a more accurate fit

The coefficients produced and the goodness of the fit are as follows :

General model:

$$f(x) = (\Delta E^2 + (\alpha * (B_z - B_{z_res}))^2)^{\frac{1}{2}}$$

Coefficients (with 95% confidence bounds):

$$\begin{aligned} B_{z_res} &= 0.07381 \quad (0.06417, 0.08346) \\ \Delta E &= 0.1803 \quad (0.1565, 0.2042) \\ \alpha &= 1.848 \quad (1.722, 1.974) \end{aligned}$$

Goodness of fit:

$$\begin{aligned} \text{SSE: } &0.1014 \\ \text{R-square: } &0.8386 \\ \text{Adjusted R-square: } &0.8319 \\ \text{RMSE: } &0.04597 \end{aligned}$$

Reverting back to units of Tesla for field and Kelvin for energy and with respect to the original B^z

axis (see caption in figure G.3) the coefficients are:

$$\begin{aligned} B_{res}^z &\rightarrow (B_{res}^z + B_0^z) \cdot 10^{-10}[T] \\ B_{res}^z &= -0.015[T] \end{aligned} \tag{G.6.2}$$

$$\begin{aligned} \Delta E &\rightarrow DeltaE \cdot 10^{-9}[K] \\ \Delta E &= 1.8 \cdot 10^{-10}[K] \end{aligned} \tag{G.6.3}$$

G.7 Finding the Landau-Zener Transition Profile

The following code designated *Landau_Zener_Transition_Functional_Form.m* numerically finds the functional form of the magnetization steps and susceptibility peaks. The standard 4th order Runge-Kutha method is applied to the Schrödinger equation to advance it from the initial condition, of complete population of the ground state, through the resonance and beyond. This procedure, and the notations used, follow the article of Vitanov [42]

The standard 4th order Runge-Kutha method is a method for numerically integrating ordinary differential equations. Details can be found e.g. here [44]

The code also applies quantum broadening (Gaussian)

```
%% %defining relevant parameters

%Lande g Factor (Unitless)
gL=5/4;
%Bohr Magneton (Kelvein/Tesla)
uB=0.6717;

%Transverse Field (Tesla)
Bx=0.6;

%The value of <Jz> does not significantly change during a crossing because the
%crossings are narrow
Jz1=-5.5;
Jz2=5.4;

%This energy gap corresponds for example to the first n=1/2 crossing
deltaE=1.8*10^(-10);

%Sweep rate (Tesla/Sec)
nu=0.03;
alpha=nu*uB*gL*(2*Jz2-2*Jz1);

%Boltzmann constant (Joule/Kelvin)
kB=1.3806504*10^(-23);
%Reduced Planck constant (Joule * Sec)
hbar=6.626*10^(-34)/(2*pi*kB);
```

```

beta=sqrt(0.5*alpha/hbar);

%Coupling between diabatic states
Omega=0.5*deltaE/hbar;

%% % Using standard Runge–Kutta 4th order method – for the occupation amplitudes

%Time step size (Sec)
dt=0.0000000001;
dT=beta*dt;

%Starting time relative to the time when the system is at the middle of the
    %resonance (Sec)
t_min=-0.0005;
%End time relative to middle of the resonance (Sec)
t_max=0.001-dt;

%Number of steps in the process
steps=(t_max-t_min)/dt;

%The process requires very small steps (dt) to produce a correct result (if the
    %steps are too big, the advancing of the schrodinger equation through time
    %can run off course). However for the purpose of analysis of the results, a
    %lower step resolution can be used. For that reason and in order to conserve
    %memory the process runs in sections where at the end of each section only one
    %representing value is saved. 'resolution' is the number of steps in each section.
resolution=1000;

%cphi are the amplitudes of the occupation for each level (for each time step)
cphi=zeros(steps/resolution+1,2);

%cphi_tag is the time derivative of cphi
cphi_tag=zeros(steps/resolution+1,2);

%Initial conditions: The ground state is 100% populated
cphi(1,1)=1;
cphi(1,2)=0;

%Initial conditions: Far away from the crossing the change in population is negligible
cphi_tag(1,1)=0;
cphi_tag(1,2)=0;

%for each section (of the size of 'resolution' number of steps)
for q=1:steps/resolution

    %Define temporary arrays for the occupation amplitudes and their derivatives.
    %leave room for initial conditions for this section
    cphi_temp=zeros(resolution+1,2);

```

```

cphi_tag_temp=zeros(resolution+1,2);

%Dictate the initial conditions for this section to be the values at the last
%step in the previous section (or in the case of the very first section,
%simply the initial conditions of the entire process)
cphi_temp(1,:)=cphi(q,:);
cphi_tag_temp(1,:)=cphi_tag(q,:);

%for all the steps in this section
for f=1:resolution
    %time=start time + time this section began + time from beggining of section
    t=      t_min      + (q-1)*resolution*dt      + (f-1)*dt ;

    Delta=beta^2*t;
    T=beta*t;

    %This is the Runge-Kutta 4th order method:
    k1(1)=1i*Delta*cphi_temp(f,1)-1i*Omega*cphi_temp(f,2);
    k1(2)=-1i*Omega*cphi_temp(f,1)-1i*Delta*cphi_temp(f,2);

    k2(1)=1i*(beta^2*(t+0.5*dt))*(cphi_temp(f,1)+0.5*dt*k1(1)) - ...
        1i*Omega*(cphi_temp(f,2)+0.5*dt*k1(2));

    k2(2)=-1i*Omega*(cphi_temp(f,1)+0.5*dt*k1(1)) - ...
        1i*(beta^2*(t+0.5*dt))*(cphi_temp(f,2)+0.5*dt*k1(2));

    k3(1)=1i*(beta^2*(t+0.5*dt))*(cphi_temp(f,1)+0.5*dt*k2(1)) - ...
        1i*Omega*(cphi_temp(f,2)+0.5*dt*k2(2));

    k3(2)=-1i*Omega*(cphi_temp(f,1)+0.5*dt*k2(1)) - ...
        1i*(beta^2*(t+0.5*dt))*(cphi_temp(f,2)+0.5*dt*k2(2));

    k4(1)=1i*(beta^2*(t+0.5*dt))*(cphi_temp(f,1)+dt*k3(1)) - ...
        1i*Omega*(cphi_temp(f,2)+dt*k3(2));

    k4(2)=-1i*Omega*(cphi_temp(f,1)+dt*k3(1)) - ...
        1i*(beta^2*(t+0.5*dt))*(cphi_temp(f,2)+dt*k3(2));

    cphi_temp(f+1,:)=cphi_temp(f,:)+(dt/6)*(k1+2*k2+2*k3+k4);
    cphi_tag_temp(f+1,1)=1i*(beta^2*t)*cphi_temp(f+1,1)-1i*Omega*cphi_temp(f+1,2);
    cphi_tag_temp(f+1,2)=-1i*Omega*cphi_temp(f+1,1)-1i*(beta^2*t)*cphi_temp(f+1,2);
end

%saving only the values at the last step of this section
cphi(q+1,:)=cphi_temp(resolution+1,:);
cphi_tag(q+1,:)=cphi_tag_temp(resolution+1,:);

end

```

```

%Switching from amplitude to probability
cP=abs(cphi).^2;

%% Applying Broadening – averaging over the probability using a gaussian distribution

%This has to be done before finding the derivative of the probability to produce
%physically meaningful results for an ensemble of ions, since the probability
%for a single pair of ions oscillates

%Broadening is due to quantum effects such as farther ions and HF interaction with
%F ions. Farther ions produce a typical longitudinal field of 1mT

%Standard Deviation of the gaussian distribution (Tesla):
sigma_Bz=0.5*10^(-3);

%same for the time axis (Secs)
sigma_t=sigma_Bz/nu;

%same in number of values used from the final data set (chpi)
sigma_steps=floor((sigma_t/dt)/resolution);

%The data set was limited to values near the crossing (where everything interesting
%happens). however the standard deviation is much larger then this region. To
%average over areas farther away from the crossing we simply dictated that the
%occupation at earlier times is the same as the initial condition, and the
%occupation at later times is the same as the last value in the data set (no
%transitions outside the area of the crossing)
cP_expanded=zeros(615000,2);
cP_expanded(1:300000,1)=cP(1,1);
cP_expanded(1:300000,2)=cP(1,2);
cP_expanded(315001:end,1)=cP(steps/resolution+1,1);
cP_expanded(315001:end,2)=cP(steps/resolution+1,2);
av_P2=zeros(6150,2);

%for (sufficiently away from the start of the array) : (in jumps of 100) : ...
%(untill sufficiently away from the end of the array)
%(The value of the braodened probability curve is found in jumps of 100 to save
%computing time since we can afford the number of steps in the result to be
%much lower than the number of step in the data set)
for n=14*sigma_steps+1:100:615000-14*sigma_steps-1

    %for each Bz value, the values taken for the gaussian distribution are from
    %14*STD values on either side.
    for k=-14*sigma_steps:1:14*sigma_steps
        av_P2(floor(n/100),1)=av_P2(floor(n/100),1) + ...
            cP_expanded(n+k,1)*exp(-0.5*(double(k)/sigma_steps)^2) / ...
            sqrt(2*pi*sigma_steps^2);
    end
end

```

```

        av_P2(floor(n/100),2)=av_P2(floor(n/100),2) + ...
            cP_expanded(n+k,2)*exp(-0.5*(double(k)/sigma_steps)^2) / ...
            sqrt(2*pi*sigma_steps^2);
    end
end

%% finding the derivative to the broadened probability

%setting a time vector for the expanded data set
t_expanded=t_min-dt*resolution*300000:dt*resolution:t_max+dt*resolution*300000;

deriv=zeros(6149,2);

%for the values in the data set for which the broadened probability was found:
for n=14*sigma_steps+1+100:100:615000-14*sigma_steps-1

    %the derivative is taken as the slope of the linear curve between two points
    %in the data set
    temp(1,:)=polyfit(t_expanded(n-100:100:n)',av_P2(floor(n/100)-1:floor(n/100),1),1);
    temp(2,:)=polyfit(t_expanded(n-100:100:n)',av_P2(floor(n/100)-1:floor(n/100),2),1);
    deriv(floor(n/100),1)=temp(1,1);
    deriv(floor(n/100),2)=temp(2,1);
end

%% plots – for the transition from one diabatic state to another

t=t_min:dt*resolution:t_min+dt*steps;
Bz=t*nu;

%Probability (before broadening) vs Bz
figure
hold on
plot(Bz(1:end),cP(1:end,2),'k','LineWidth',1.5);
ylabel('Probability','FontSize',16);
xlabel('B^z_⊥[T]','FontSize',16);
set(gca,'FontSize',14);

t_expanded=t_min-dt*resolution*300000:dt*resolution:t_max+dt*resolution*300000;
Bz_expanded=t_expanded*nu;

%Broadened Probability
figure
hold on
plot(Bz_expanded(14*sigma_steps+1:100:615000-14*sigma_steps-1), ...
    av_P2(floor((14*sigma_steps+1)/100):1: ...
        floor((615000-14*sigma_steps-1)/100),2),'k','LineWidth',1.5);

```

```

ylabel('Probability','FontSize',16);
xlabel('B^z_{T}','FontSize',16);
set(gca,'FontSize',14);

%Derivative of broadened Probability
figure
hold on
plot (Bz_expanded(14*sigma_steps+1+100:100:615000-14*sigma_steps-1), ...
      deriv(floor((14*sigma_steps+1+100)/100):1: ...
            floor((615000-14*sigma_steps-1)/100),2),'k','LineWidth',1.5);

ylabel('$dP_{LZ}/dB^z$', 'FontSize',20, 'Interpreter', 'latex');
xlabel('B^z_{T}','FontSize',16);
set(gca,'FontSize',14);

```

Bibliography

- [1] Y. Imry and S. K. Ma. Random-field instability of the ordered state of continuous symmetry. *Phys. Rev. Lett.*, 35:1399–1401, Nov 1975.
- [2] S. Fishman and A. Aharony. Random field effects in disordered anisotropic antiferromagnets. *Journal of Physics C: Solid State Physics*, 12(18):L729, 1979.
- [3] W. KLEEMANN. Random-field induced antiferromagnetic, ferroelectric and structural domain states. *International Journal of Modern Physics B*, 07(13):2469–2507, 1993.
- [4] K. A. Reza and D. R. Taylor. Measurement of static critical exponents for a structural ising-model phase transition with random strains: $\text{Dy}(\text{as}_x\text{v}_{1-x})\text{o}_4$. *Phys. Rev. B*, 46:11425–11431, Nov 1992.
- [5] J. T. Graham, J. H. Page, and D. R. Taylor. Ultrasonic investigation of critical behavior in the random-field ising system $\text{dy}(\text{as}_x\text{v}_{1-x})\text{o}_4$. *Phys. Rev. B*, 44:4127–4134, Sep 1991.
- [6] B. J. Frisken, David S. Cannell, M. Y. Lin, and S. K. Sinha. Neutron-scattering studies of binary mixtures in silica gels. *Phys. Rev. E*, 51:5866–5879, Jun 1995.
- [7] M. Schechter and N. Laflorencie. Quantum spin glass and the dipolar interaction. *Phys. Rev. Lett.*, 97:137204, Sep 2006.
- [8] M. Schechter. $\text{LiHo}_x\text{Y}_{1-x}\text{F}_4$ as a random-field ising ferromagnet. *Phys. Rev. B*, 77:020401, Jan 2008.
- [9] B. Barbara, R. Giraud, W. Wernsdorfer, D. Mailly, P. Lejay, A. Tkachuk, and H. Suzuki. Evidence for resonant magnetic tunneling of rare-earth ions: from insulating to metallic matrix. *Journal of Magnetism and Magnetic Materials*, 272276, Part 2(0):1024 – 1029, 2004. Proceedings of the International Conference on Magnetism (ICM 2003).
- [10] M.J.P Gingras and P. Henelius. Collective phenomena in the $\text{LiHo}_x\text{Y}_{1-x}\text{F}_4$ quantum ising magnet: Recent progress and open questions. *Journal of Physics: Conference Series*, 320(1):012001, 2011.
- [11] B. Coqblin. *The electronic structure of rare-earth metals and alloys: the magnetic heavy rare-earths*. (A Anouk). Academic Press, 1977.

- [12] R.J. Elliott. *Magnetic properties of rare earth metals*. Plenum Press, 1972.
- [13] J.L. Prather. Atomic energy levels in crystals. Technical report, U.S. Department of Commerce. National Bureau of Standards, 1961.
- [14] P. B. Chakraborty, P. Henelius, H. Kjønsberg, A. W. Sandvik, and S. M. Girvin. Theory of the magnetic phase diagram of LiHoF_4 . *Phys. Rev. B*, 70:144411, Oct 2004.
- [15] R. Giraud, W. Wernsdorfer, A. M. Tkachuk, D. Mailly, and B. Barbara. Nuclear spin driven quantum relaxation in $\text{LiY}_{0.998}\text{Ho}_{0.002}\text{F}_4$. *Phys. Rev. Lett.*, 87:057203, Jul 2001.
- [16] M. Schechter and P. C. E. Stamp. Significance of the hyperfine interactions in the phase diagram of $\text{LiHo}_x\text{Y}_{1-x}\text{F}_4$. *Phys. Rev. Lett.*, 95:267208, Dec 2005.
- [17] M. Schechter and P. C. E. Stamp. Derivation of the low- t phase diagram of $\text{LiHo}_x\text{Y}_{1-x}\text{F}_4$: A dipolar quantum ising magnet. *Phys. Rev. B*, 78:054438, Aug 2008.
- [18] Wenhao Wu, B. Ellman, T. F. Rosenbaum, G. Aeppli, and D. H. Reich. From classical to quantum glass. *Phys. Rev. Lett.*, 67:2076–2079, Oct 1991.
- [19] Wenhao Wu, D. Bitko, T. F. Rosenbaum, and G. Aeppli. Quenching of the nonlinear susceptibility at a $T = 0$ spin glass transition. *Phys. Rev. Lett.*, 71:1919–1922, Sep 1993.
- [20] J. F. A. Silva A. H. Cooke, D. A. Jones and M. R. Wells. Ferromagnetism in lithium holmium fluoride- LiHoF_4 : magnetic measurements. *J. Phys. C*, 1975.
- [21] D. H. Reich, B. Ellman, J. Yang, T. F. Rosenbaum, G. Aeppli, and D. P. Belanger. Dipolar magnets and glasses: Neutron-scattering, dynamical, and calorimetric studies of randomly distributed ising spins. *Phys. Rev. B*, 42:4631–4644, Sep 1990.
- [22] R. Giraud, A. M. Tkachuk, and B. Barbara. Quantum dynamics of atomic magnets: Cotunneling and dipolar-biased tunneling. *Phys. Rev. Lett.*, 91:257204, Dec 2003.
- [23] S. Bertaina, B. Barbara, R. Giraud, B. Z. Malkin, M. V. Vanuynin, A. I. Pominov, A. L. Stolov, and A. M. Tkachuk. Cross-relaxation and phonon bottleneck effects on magnetization dynamics in $\text{LiYf}_4 : \text{Ho}^{3+}$. *Phys. Rev. B*, 74:184421, Nov 2006.
- [24] Z. B. Goldschmidt. Chapter 1 atomic properties (free atom). In K. A. Gschneidner and L. Eyring, editors, *Metals*, volume 1 of *Handbook on the Physics and Chemistry of Rare Earths*, pages 1 – 171. Elsevier, 1978.
- [25] V. Heine. *Group Theory in Quantum Mechanics*. Dover Books on Physics and Chemistry. Dover Publications, 1960.
- [26] K. W. H. Stevens. Matrix elements and operator equivalents connected with the magnetic properties of rare earth ions. *Proceedings of the Physical Society. Section A*, 65(3):209, 1952.

- [27] D J Newman and B Ng. The superposition model of crystal fields. *Reports on Progress in Physics*, 52(6):699, 1989.
- [28] G. Burns. Shielding and crystal fields at rare-earth ions. *Phys. Rev.*, 128:2121–2130, Dec 1962.
- [29] M.T. Hutchings. *Point Charge Calculations of Energy Levels of Magnetic Ions in Crystalline Electric Fields*. Defense Technical Information Center, 1963.
- [30] D. S. Fisher and D. A. Huse. Ordered phase of short-range ising spin-glasses. *Phys. Rev. Lett.*, 56:1601–1604, Apr 1986.
- [31] D. S. Fisher and D. A. Huse. Equilibrium behavior of the spin-glass ordered phase. *Phys. Rev. B*, 38:386–411, Jul 1988.
- [32] L. I. Schiff. *Quantum Mechanics*. International series in pure and applied physics. McGraw-Hill Education (India) Pvt Limited, 1968.
- [33] Chao Y. Arpack homepage, 1997. <http://www.caam.rice.edu/software/ARPACK/>.
- [34] Y. Saad. *Iterative Methods for Sparse Linear Systems*. Society for Industrial and Applied Mathematics, 2003.
- [35] N. Laflorencie and D. Poilblanc. Simulations of pure and doped low-dimensional spin-1/2 gapped systems. In U. Schollwck, J. Richter, D.J.J. Farnell, and R. Bishop, editors, *Quantum Magnetism*, volume 645 of *Lecture Notes in Physics*, pages 227–252. Springer Berlin Heidelberg, 2004.
- [36] G. W. Benthien. Notes on numerical linear algebra, 2006. <http://gbenthien.net/NumLinAlg.pdf>.
- [37] L. D. Landau. A theory of energy transfer ii. *Physik. Z. Sowjet*, 1932.
- [38] C. Zener. Non-adiabatic crossing of energy levels. *Proceedings of the Royal Society of London. Series A*, 137(833):696–702, 1932.
- [39] E. Shimshoni and A. Stern. Dephasing of interference in landau-zener transitions. *Phys. Rev. B*, 47:9523–9536, Apr 1993.
- [40] A. Palii, B. Tsukerblat, J. M. Clemente-Juan, A. Gaita-Ariño, and E. Coronado. Manipulation of the spin in single molecule magnets via landau-zener transitions. *Phys. Rev. B*, 84:184426, Nov 2011.
- [41] Kayanuma Y. Nonadiabatic transitions in level crossing with energy fluctuation. i. analytical investigations. *Journal of the Physical Society of Japan*, 53(1):108–117, 1984.
- [42] N. V. Vitanov and B. M. Garraway. Landau-zener model: Effects of finite coupling duration. *Phys. Rev. A*, 53:4288–4304, Jun 1996.

- [43] Mingjing Zhang. Manipulate: Interactive parametrized plotting, 2012.
<http://www.mathworks.com/matlabcentral/fileexchange/36512-manipulate-interactive-parametrized-plotting>.
- [44] J.C. Butcher. *Numerical Methods for Ordinary Differential Equations*. John Wiley & Sons, 2008.